SPIN-TORQUE EFFECTS IN MGO-BASED MAGNETIC TUNNEL JUNCTIONS

A Dissertation

Presented to the Faculty of the Graduate School

of Cornell University

in Partial Fulfillment of the Requirements for the Degree of

Doctor of Philosophy

by

Hsin-wei Tseng

January 2013

SPIN-TORQUE EFFECTS IN MGO-BASED MAGNETIC TUNNEL JUNCTIONS

Hsin-wei Tseng, Ph.D.

Cornell University 2013

This thesis work focuses on understanding the fundamentals of the spin-torque effect in MgO-based high tunneling magnetoresistance (TMR) magnetic tunnel junction (MTJ) nanopillar geometry devices. In order to achieve this goal, I have successfully established a reliable and repeatable high TMR and low resistance-area (RA) product MgO sputtering process at Cornell. Currently, we are capable of sputtering TMR ($>$100% with RA$<10\Omega/\mu m^2$). In addition to speeding up the nanopillar two-terminal structure fabrication process, I have also worked on improving the nanopillar lift-off process, which has enabled me to finish the nanopillar fabrication process within a week. We have full control over high TMR MgO MTJ materials, nanofabrication and spin-torque analysis schemes at Cornell.

I have shown that the spin-torque effect in asymmetric MgO-based MTJ could be significantly affected by the electronic structure in the electrodes or electrode/barrier interface in the MTJ (”asymmetric” MTJs indicate bottom and top electrodes materials are different ferromagnetic materials and ”symmetric” MTJs have identical bottom and top electrode ferromagnetic materials.) Briefly, I have shown that the field-like torque in the asymmetric MTJs exhibit non-zero torkance at zero bias and would further reverse torkance asymmetric when the electrode was reversed from $Fe_{40}Co_{40}B_{20}$/MgO/$Fe_{80}B_{20}$ to $Fe_{80}B_{20}$/MgO/$Fe_{40}Co_{40}B_{20}$. In addition,

the field-like torque exhibits a constant and weak voltage dependence compared to symmetric $Fe_{40}Co_{40}B_{20}/MgO/Fe_{40}Co_{40}B_{20}$ MTJs. Symmetric $Fe_{80}B_{20}/MgO/Fe_{80}B_{20}$ MTJs exhibit opposite in-plane torkance compared to symmetric $Fe_{40}Co_{40}B_{20}/MgO/Fe_{40}Co_{40}B_{20}$.

I also further probe the differences in spin-transfer torque in high TMR MgO-based MTJs, I have developed a pulse-biased microwave emission measurement to understand the spin-torque behavior under high current densities for real ultra-fast (<1ns) spin-torque-based magnetic switching devices. Here, I have observed that the microwave emissions are highly asymmetric under positive and negative voltage polarities. Within the bi-polar stable switching region, negative polarity (electrons flowing from fixed to free) induced strong microwave emission, but there is no microwave emission with positive voltage. This phenomena could be understood by a strong field-like torque effect affecting in-plane torque driven dynamics. Macromagnetic power phase diagram simulations capture the major features observed in the pulse-biased experiments. This result indicated that field-like torque could play a dominant role inducing unreliable switching even in the symmetric MTJ, plus the strong asymmetric in-plane torque with negative polarities could introduce chaotic dynamics and resulting in back-hopping switching.

BIOGRAPHICAL SKETCH

Hsin-wei Tseng was born on March 21st, 1982 in Kaohsiung, Taiwan, to Ching-yin Tseng and Su-zhen Huang. Hsin-wei Tseng has an older brother Hsin-yu Tseng, who has been very supportive to his career and a great blessing to the family. With his persistence and help, Hsin-wei Tseng was able to study overseas to pursue his goals and dreams. Hsin-wei had a happy and playful childhood, as his family once ran a convenience store which sold lots of food, drinks and computer games. Hsin-wei had unlimited access to those "resources" and was still able to perform well in school. Hsin-wei Tseng attended Kaohsiung Senior High School at Kaohsiung, where he was educated by encouraging and loving teachers who urged him pursue higher education. Since childhood, Hsin-wei has had a strong interest in understanding how things are made and work. In 2000, Hsin-wei enrolled National Tsing Hua University, Taiwan and majored in physics there. He was inspired by the great passion of physicists to strive for knowledge in natural science. After obtaining his B.S. degree in 2004, Hsin-wei began his two-year mandatory military service before leaving for the United States for a graduate degree. In 2008, he left the country he had lived in for 24 years. Hsin-wei was really excited about spin-transfer torque physics and how the electrons interact with each other to change magnetic magnetizations, he was lucky enough to start his Ph.D. degree with Prof. Robert A. Burhman at the School of Applied and Engineering Physics, Cornell University. In 2010, he married with Rui Kan and soon had their first-born baby boy Ryan.

To Rui Kan and Ryan Tseng, wife and son, who have supported me unconditionally. And to my family who raised me through many difficulties, Ching-yin Tseng, Su-zhen Huang and Hsin-yu Tseng.

ACKNOWLEDGEMENTS

First of all, I would like to thank my Ph.D. advisor Prof. Robert A. Buhrman for his trust, patience, encouragement and great faith he has shown through his doing and his persistent research works. Through my Ph.D. path, there are ups and downs, Bob had been really patient and I sincerely appreciate the courtesy he had extended to me. I am lucky enough to be able to work for and with Bob that I had a chance to work on pioneering experiments and had access to world-leading nanofabrication facilities at Cornell, Cornell Nanofabrication Facilities (CNF). I would also like to express my appreciation for my special committee members Prof. Daniel C. Ralph and Prof. Bruce van Dover to provide my knowledge and guidance along my Ph.D. path. Also, I have collaborated with Prof. Edwin C. Kan and his student Jonathan Shaw on MgO/Si MOS capacitor project to further understand properties of defeat state in ultra thin MgO oxide through Cornell Center for Materials Research (CCMR).

I also like to thank my mentors Dr. John Read and Dr. Patrick Braganca for his guidance and help with my experiments. They have been assisting me during their time at Cornell and even after they graduated. John patiently and encouragingly taught me all the hard works of maintaining the ultra-high vacuum (UHV) instruments in D7 and the complicated operation of scanning tunneling microscopy (STM) and the ballistic electron emission microscopy (BEEM). Operating and maintaining the complicated, delicate and expensive scientific instruments in D7 build my confidence and faith that I am capable of working on those highly sensitive experiments without destroying them. Patrick taught me how to work on nanofabrication to building nanopillars which I do not believe I could ever achieve in the beginning when I joined the group. I really appreciated all the time Patrick discussed with me even when I cannot speak English

well.

In addition, I have been really grateful for working with many great coworkers in both our group and Prof. Ralph's group. Yun Li and I have been working in the D7 since both of us starting working in the group. Keeping D7 up and running by oneself is not an easy task at all both physically and mentally. Several times while I had faced some complicated issues regarding the UHV system in the D7, discussing the issues with Yun has become extremely helpful to double check my concepts and tentative schemes to fix the problems in the UHV chamber. Not only the scientific works, but also Yun has been a very reliable and careful person and coworker. I could totally reply on her's work to achieve very complicated and keep up all the details of some very subtle experiments. I alos appreciated all my lab mates for their assistance and persistence on maintaining all the lab equipments for making my experiments ever possible. Oukjae Lee and Praveen Gowtham have great personalities to work with and to enjoy time with. While the experiments do not go well, I would share my frustration with them and they have been extremely encouraging and helpful for my frustration to share my motion need. In addition, I really appreciate their great knowledge and time devoting on maintaining both ion milling tools to keep those tools always up and running for our experiments. I also like to thank for great help from Jonathan Shu and Steve from Center for Nanoscale Systems (CNS). Through the years, I have been using CNS equipments to perform my measurement. Many of my friends from both Cornell and First Chinese Christian Fellowship have been extremely helpful for both my professional career and my personal life.

Finally, I would like to thank my wife Rui Kan. She has been supporting me through my difficult time and raising the baby while I had being busy working

on my thesis. My little boy, Ryan, he is the cutest baby in the home to entertain me in many different ways. Also, I want to show my appreciation to my parent and my brother. They have been the motivation and they has been encouraging me and supporting me through many difficult time in my life. They has been raising through their own difficult time which I did not appreciate until I have my own family.

TABLE OF CONTENTS

LIST OF TABLES

LIST OF FIGURES

CHAPTER 1

INTRODUCTION

Spintronics is an emerging research focusing on manipulation and control of the electron spin instead of pure electron charge[89]. The application of spintronics enable the possibilities of the interactions between electron spin and magnetic properties and can be easily further integrated with current silicon-based electronics technologies. For instance, spin-torque (ST) switching in the nanopillar structure is applied to magnetic random access memory (MRAM) for non-volatile memory for instant-on computation technology. Due to this strong driving from the consumer electronics, there have been many companies and research groups established and focused to explore the ST engineering. In the recent years, there has been many significant discoveries and enhancing of ST effect in the MgO-based MTJs. We, however, still not very well understood the fundamental physics of ST in the MgO-based MTJ. In this thesis, I will focus on understanding and exploring the fundamental ST physics in the MgO-based MTJs.

First of all, chapter 2 presents the fundamental of MTJs and both experiments and theories of spin-torque in MTJs and the current status of experiment progress. First, I will discuss the fundamental of spin-polarized tunneling in the MTJ in the early work and recent progresses in the high tunneling magnetoresistance (TMR) in the MTJ at room temperature (AlO_x and MgO) and further present the current understanding of the fundamental physical and material in the MTJs about the interfacial state and TMR. Furthermore, I will discuss the spin-transfer torque in the MTJs and other novel three-terminal device concepts developed in the last few years for MRAM application.

Chapter 3 present the details of MgO-based materials in the AJA sputtering chamber at Cornell, which I have been working on in the last few years. First, I will discuss the motivation of pursing high TMR MgO MTJs at Cornell. Then, I analyze the obstacles and challenges growing high TMR MgO MTJs at Cornell and how we solved those issues. I summarize the reliable process parameters of growing high TMR CoFeB-based MgO MTJs in AJA. I will further present some basic concepts I have learned which are helpful speeding of materials characterization.

Chapter 4 describes the details of HSQ/PMMA lift-off process for fabricating nanopillar. Different from previous carbon-based nanomask approach, I will describe how I developed HSQ/PMMA lift-off process for fabricating nanopillars smaller than 100nm. I will show the SEM and AFM images of the resolution of this HSQ/PMMA process and describe several difficulties in the process. Several important designing concept in the CAD design and fracturing conversion software (Layout Beamer). Summary of the HSQ/PMMA lift-off process will be presented in details.

Chapter 5 presents the chemical analyses based on electron energy loss spectroscopy (EELS), electronic transport studies and spin-torque studies on asymmetric FeCoB/MgO/FeNiB MTJs. First, EELS results indicate that the FeNiB alloy exhibit phase segregation between Fe and Ni after annealing. Besides, the tunneling conductance as a functions of voltage ($dI/dV - V$) manifest significant asymmetry under different current polarities, which indicated electronic structure is on two sides of the tunnel barrier. In addition, the switching behavior is highly abnormal while comparing to typical spin-valve device. More than one sample exhibit abnormal switching behavior. To further understand the ST

physics in the MgO-based MTJs, I explore the ST in four different ferromagnetic material configurations of MgO-based MTJs.

Chapter 6 describes a pulse-biased microwave measurement developed to measure the ST-driven dynamics of nanomagnets under high current densities. The motivation of this experiment is because previous microwave measurements are mostly based on DC-based current. Therefore, DC-based technique does not provide dynamic behaviors of nanomagnet with current densities corresponding to real application. First, I will review the microwave measurement which explore the complete parameter space of power phase diagram of spin valves under various currents and field configurations. Second, I will present current research results about microwave measurement in CoFeB/MgO/CoFeB ST-driven nanopillar MTJs. Third, I will describe the circuit of the pulse-biased microwave measurement technique and will discussed about its strength and weakness. Finally, I will show the result from the pulse-biased microwave measurement in low RA CoFeB/MgO/CoFeB nanopillars with various coercivities ranged from ~130Oe to 0Oe and explain the possible current-induced mechanisms governing power phase diagram.

Finally in Chapter 7, I will provide a summary of the most significant result of my work.

CHAPTER 2

BACKGROUND

2.1 Motivation

Nowadays, many scientific researches are significantly driven by the need of consumer electronics. Goal of many applied science or engineering projects are aiming to overcome the limitations of conventional silicon-based CMOS technologies. One important motivation is non-volatile memory application to further reduce the power consumption from conventional dynamics random access memory (DRAM) or even used as an universal memory. Figure 2.1(a) show the conventional architecture of computation. The conventional computation architecture require significant amount of booting time to load data from slow storage medias, such as hard-disk drive (HDD) or solid-state drive (SDD). A main goal of future computation architecture to reduce power consumption and feature instant ON/OFF capability, which will require at least a faster type of non-volatile memory to replace the most common dynamics random access memory (DRAM) in personal computers. Magnetic RAM has been one type of non-volatile memories pursued for more than 30 years. Spin-transfer-torque-based RAM (STRAM) is one of the most promising candidate in MRAM and other several non-volatile technologies, such as phase-change RAM and FeRAM.

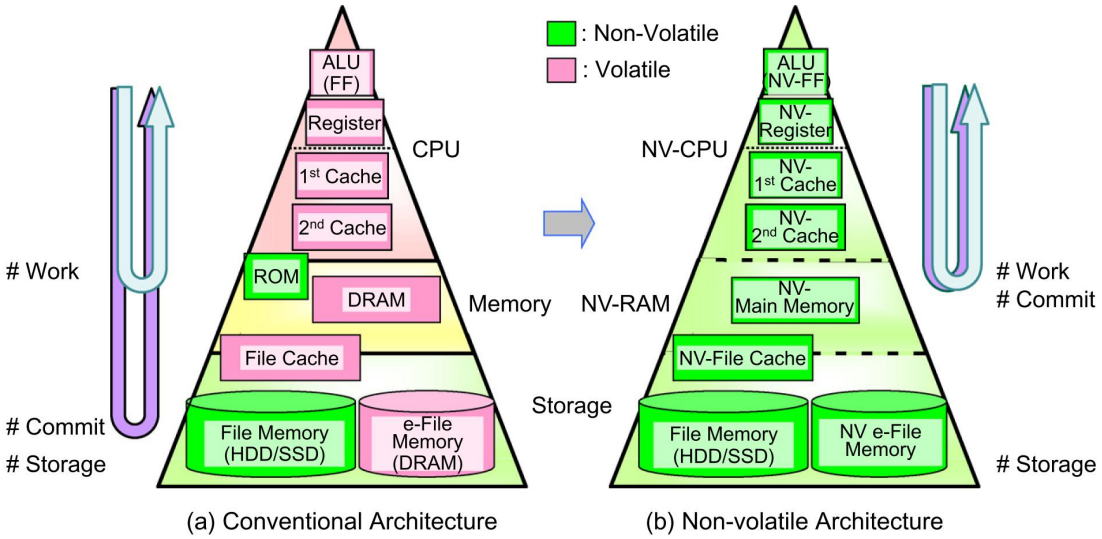

Figure 2.1: Conventional computation architecture versus non-volatile architecture based on non-volatile memory. (From Ref. [35])

Currently, there are two different kinds of MRAM writing schemes. A conventional MRAM uses a write word line and a bit line (shown in Fig 2.2(a)). This writing scheme pass large current density through the write word line to cause the bit switched with the magnetic field generated by the current. This scheme require large current density and has limitation on the scaling due the field affecting nearby bits. Another scheme based on spin-transfer torque effect enable directly writing and reading through the line which is beneficial for reducing the cell size (shown in Fig 2.2(b)). Switching bits with ST effect also benefit with reducing the critical current while shrinking the device cell area.

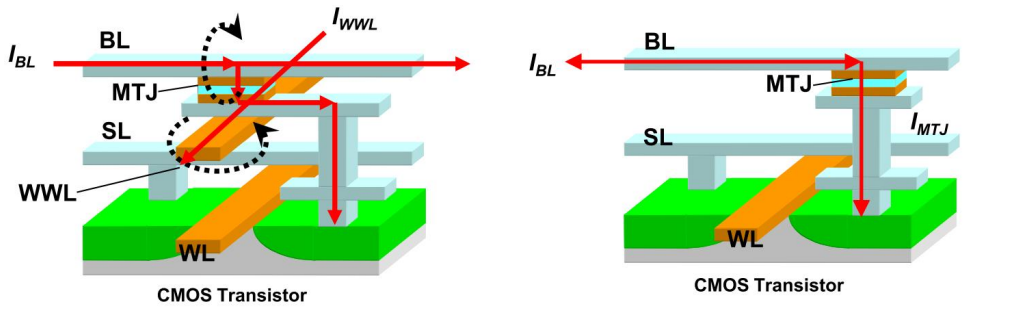

(a) Conventional MRAM using write method with magnetic field

(b) Spin transfer torque RAM (SPRAM) using write method with spin-polarized current

Figure 2.2: Two different MRAM architectures. (a) conventional MRAM architecture utilize magnetic-field for writing requiring high current densities and has lower bit density. (b) spin-transfer torque MRAM using the spin-polarized current directly injecting spin and inducing magnetization switching. This architecture allows cross-point memory structure and could have easily achieve ultrahigh density.

2.2 Magnetic Tunnel Junctions

Magnetic tunnel junctions (MTJs) are the important and fundamental MRAM cells due to its high magnetoresistance (MR) and tunable resistance-area (RA) product and has been studied extensively. Spin-dependent tunneling in solid state system has been demonstrated more than 30 years ago by Julliere[31]. Julliere's work has established the quantitative approach to measure the spin polarization of a magnetic tunnel junction. Moodera *et al.*[53] significantly enhance the tunneling magnetoresistance to 10% in CoFe/AlO_x/NiFe at room temperature and 24% at low temperature (4.2K).

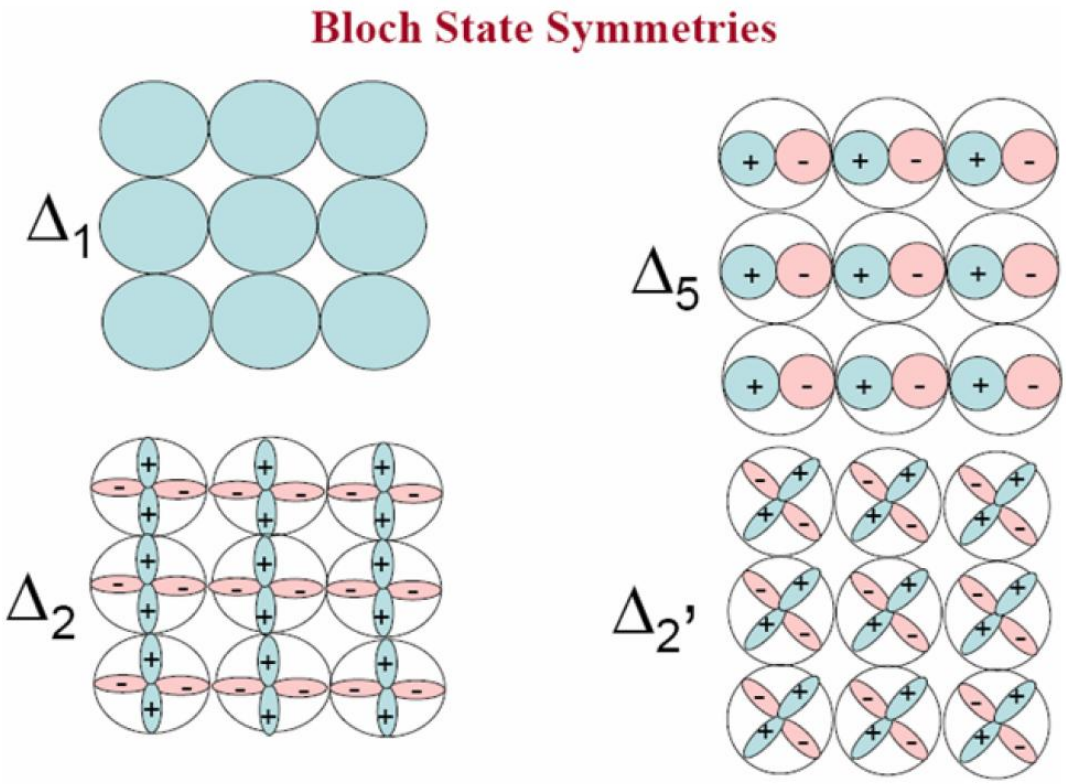

Figure 2.3: Two-dimension Bloch state symmetries of electrons which is compatible with a square lattice in the x-y plane (figure from Ref. [12])

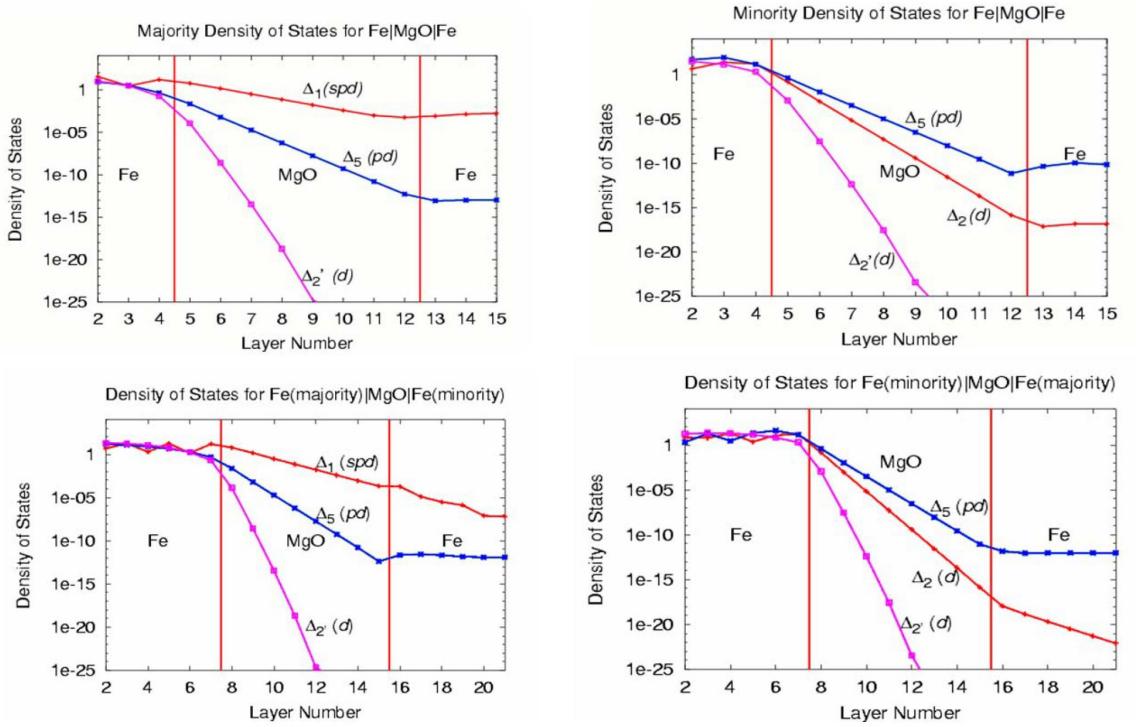

Figure 2.4: Tunneling DOS for $k_{||} = 0$ for Fe(100)/8MgO/Fe(100) system. The top two figures show the tunneling DOS for majority and minority in parallel configuration. Bottom two figures are the tunneling DOS in the antiparallel alignment.(Figure from Ref.[12])

In 2001, Butler *et al.*[11] and Mathon[48] use first-principles calculations to calculate the tunneling conductance and magneto conductance of epitaxial Fe(100)/Mg(100)/Fe(100) structure. In addition, they found that in fully crystallized Fe / MgO /Fe MTJs, the TMR could exceed 1000%. This result suggest several significant findings. First, the tunneling conductance not only depend on the spin polarization of the electrodes, but also the symmetry of the Bloch states in the electrodes and in the evanescent states in the tunneling barrier. Second, the different symmetry of Bloch state of the electrons have different decay rate which depends on the energy bands in the barriers (illustrations of Bloch

state symmetries shown in Figure 2.3). Figure 2.4 show the tunneling DOS for $k_{\|} = 0$ for Fe(100)/8MgO/Fe(100). This figure shows that the $\Delta_1(spd)$ symmetry has the slowest decay rate in the tunnel barrier and next is $\Delta_5(pd)$ symmetry. Therefore, electrons with $\Delta_1(spd)$ symmetry can easily tunnel through barrier and coupled to another Fe electrode. The phenomena is called spin-filtering effect, since only particular electrons could tunnel through MgO barrier in this Fe/MgO/Fe system.

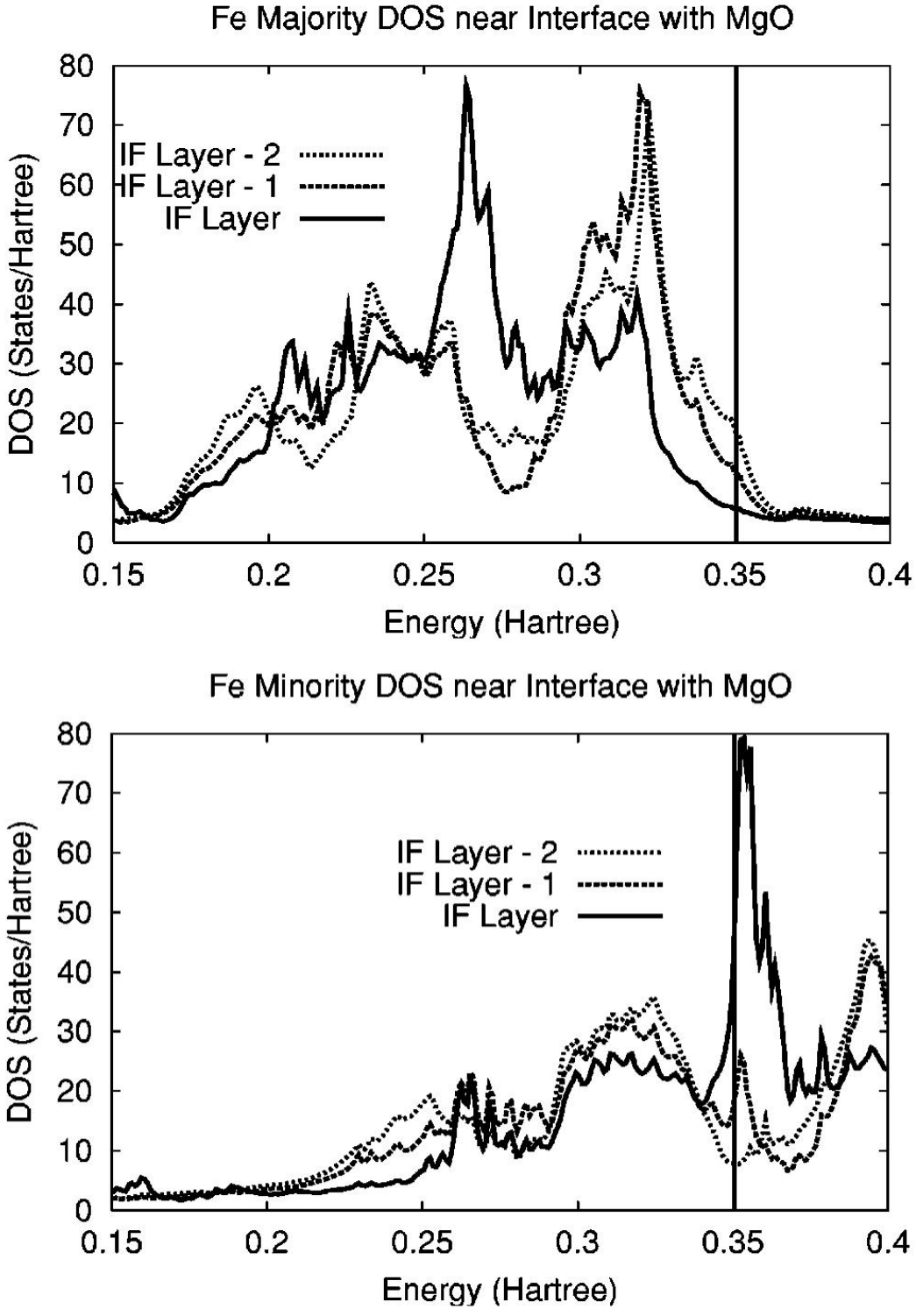

Figure 2.5: DOS for each atomic layer of Fe(100) near the interface with MgO. One hartree = 27.2eV. The solid-vertical line represents the Fermi surface.

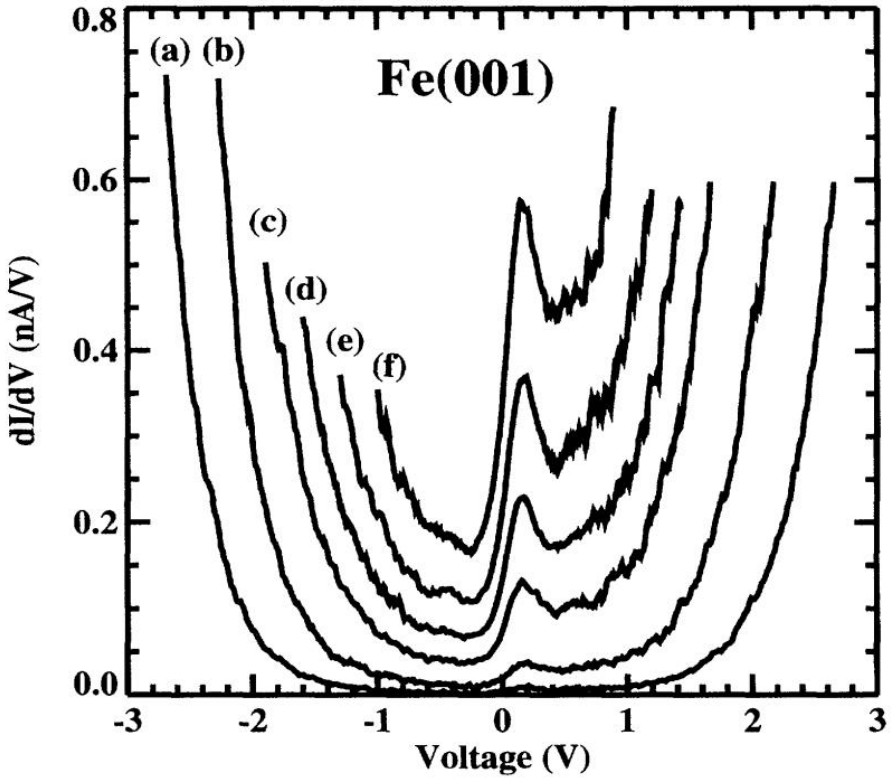

Figure 2.6: Tunneling conductance vs sample voltage measurement on a Fe (001) surface. The dI/dV are obtained at a constant height above Fe surface. The dI/dV were obtained by numerical differetion of the current vs voltage measurement I-V. (Figure from Ref.[76])

Another important discovery which is related to our measurement observation is that a sharp peak of minority spin surface and interfacial states (IS) in the DOS falls slight above the Fermi level in bcc Fe(001) system. Figure 2.5 show a strong peak in the minority DOS just above the Fermi level. This result is calculated by using local spin density approximation (LSDA) to density functional theory (DFT) implemented within the full-potential linearized augmented plane wave (FLAPW) techniques. Experiment observation has be reported in bcc Fe surface states by scanning tunneling microscopy (STM)[76]. Figure 2.6 show the tunneling spectroscopy of Fe(001) surface obtained at constant height above the

Fe surface.

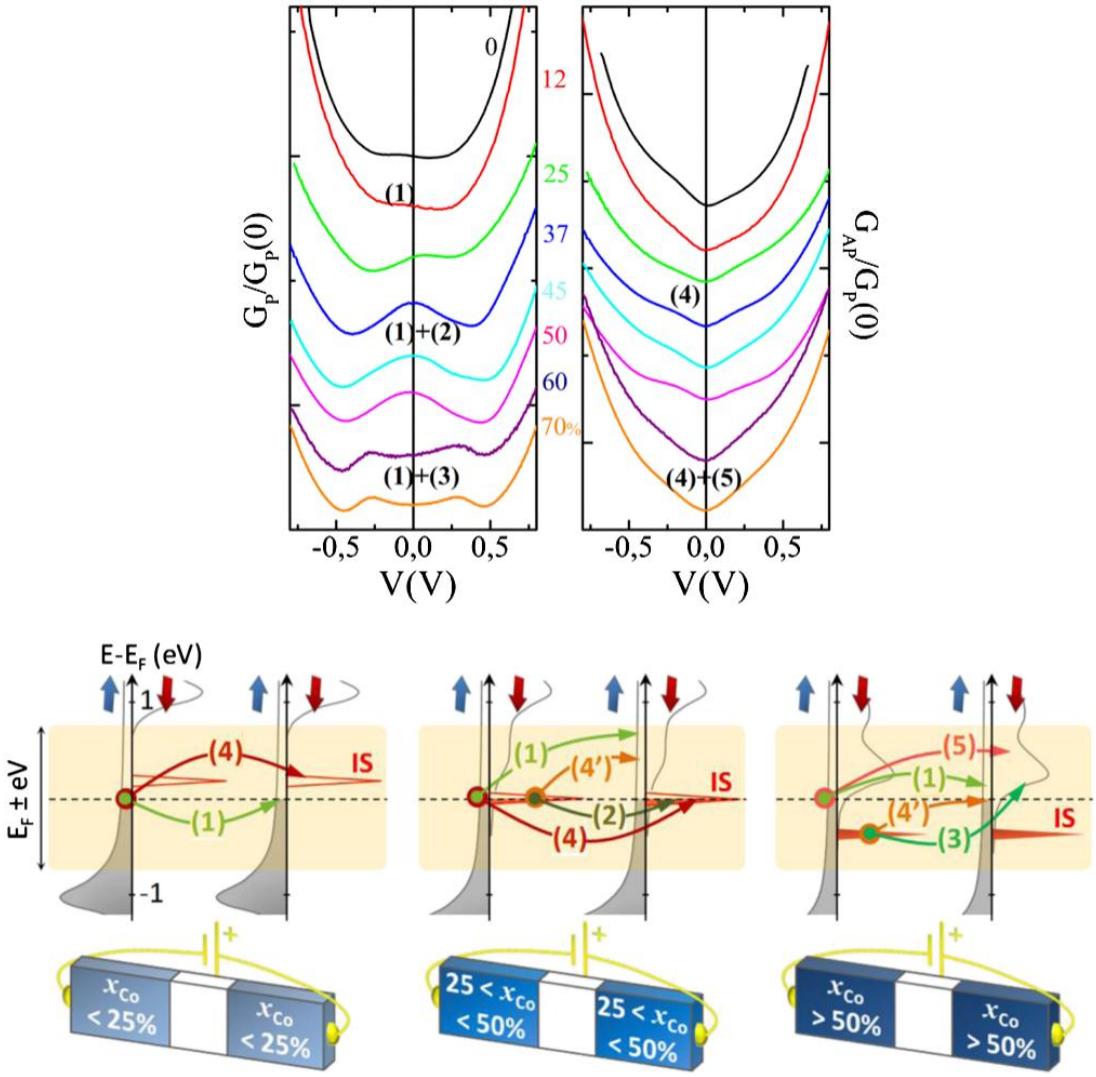

Figure 2.7: Top: Parallel and anti-parallel tunneling conductance as a function of voltage ($G_P(V)$ and $G_{AP}(V)$). Bottom: the band structure of various $Fe_{1-x}Co_x$ alloys in the MTJs and how different tunneling channels influence the tunneling conductance features (From Ref [4])

More recently, Bonell *et al.*[4] combined spin- and symmetry-resolved photoemission spectroscopy, magnetotransport measurement and *ab initio* calcu-

lation to examine how electronic structure in the $Fe_{1-x}Co_x(001)$ / MgO / $Fe_{1-x}Co_x(001)$ affects the electronic transport. First, the spin-resolved photoemission spectroscopy showed the existence of the Δ_1 surface state at the bcc (001) free surfaces which also been reported in Fe(001)[76, 3, 63]. *Ab initio* calculation suggested it also present at the Fe/MgO interface as interfacial states (IS) coupled to bulk state. However, there is no direct experiment results showing the effect of interface state. Bonell *et al.*[4] further show the interface state in the FeCo alloys is gradually filled with increasing Co content with spin-resolved photoemission spectroscopy. Due to the existence of IS, the additional conduction channel actually affects the electronic transport. Figure 2.7 show how the IS and bulk state in different FeCo alloys affecting the parallel and anti-parallel tunneling condutances ($G_P(V)$ and $G_{AP}(V)$). Channel (1) represents the ($\Delta_1 \uparrow \rightarrow \Delta_1 \uparrow$) tunneling channel in P configuration. Channel (4) : the ($\Delta_1 \uparrow \rightarrow \Delta_1 \downarrow$) tunneling channel in AP configuration. Channel (2) : ($\Delta_1(IS) \downarrow \rightarrow \Delta_1(IS) \downarrow$). Channel (4′) : ($\Delta_1(IS) \downarrow \rightarrow \Delta_1(Bulk) \uparrow$). Channel (3) : ($\Delta_1(IS) \downarrow \rightarrow \Delta_1(Bulk) \downarrow$). Channel (5) : ($\Delta_1(Bulk) \uparrow \rightarrow \Delta_1(Bulk) \downarrow$). Depending on different FeCo alloy compositions, different channels may be activated, which further leading to small decrease or large increase in the $G_P(V)$ and $G_{AP}(V)$. This authors conclude that the existence of $\Delta_1(IS) \downarrow$ and the empty $\Delta_1(Bulk) \downarrow$ significantly reduce the half-metallicity of FeCo which Co content is greater than 25%. The consequence further cause the decrease of experimental TMR performance of FeCo/MgO/FeCo MTJs.

2.3 Spin-transfer Torques in the Magnetic Tunnel Junctions

In addition to the significant scientific discovery of high TMR MTJs at room temperature, another important finding is the spin-transfer torque, which is the reverse effect of MR. Since the prediction and discover of spin-torque effect in the 1990s, intensive researches have been focusing both the fudametal physics and engineering aspects due to its potential application to MRAM application. At 1996, Slonczewski[74] and Berger[2] predicted spin-polarized electron current could transfer angular momentum to a ferromagnetic layer and induced spin-transfer-torque switching. Until 1999, Katine *et al.*[33] and Myers *et al.*[56] successfully demonstrated convincing spin-torque-driven switching and microwave wave results in a single-domain Co/Cu/Co spin valve nanopillar. Detailed discussion of spin transfer torques can be found in Ref [64].

Later 2004, because of the important discovery of high TMR>100% CoFe-based MgO MTJs at room temperature[61, 92]. Because of this important results, significant efforts to observe spin-torque behavior in the MTJ system. Both Fuchs[24] and Huai[30] have shown spin-torque-driven switching in the MTJ. One critical aspect of being able to use MTJs for spin-torque-driven magnetic switching device is for impedance match with a CMOS transistor, since the resistance-area (RA) product can be tuned with the tunnel barrier thickness. Spin-torque transfer in the MTJ require tunnel barrier to thin enough for RA within the window that enough current densities can be tunneled through the barrier without barrier breakdown. In the same time, the tunnel barrier need to be thick enough for TMR high enough for signal sensing. Soon, several efforts to understand the fundamental spin-torque effect in the MTJs. Deac *et al.*[17] measure the microwave emission to estimate the in-plane and field-like torque

in the MgO-based MTJs. Currently, ST-FMR technique is applied to MgO-based MTJs to quantitatively measure the spin-torque vectors[70, 85, 86].

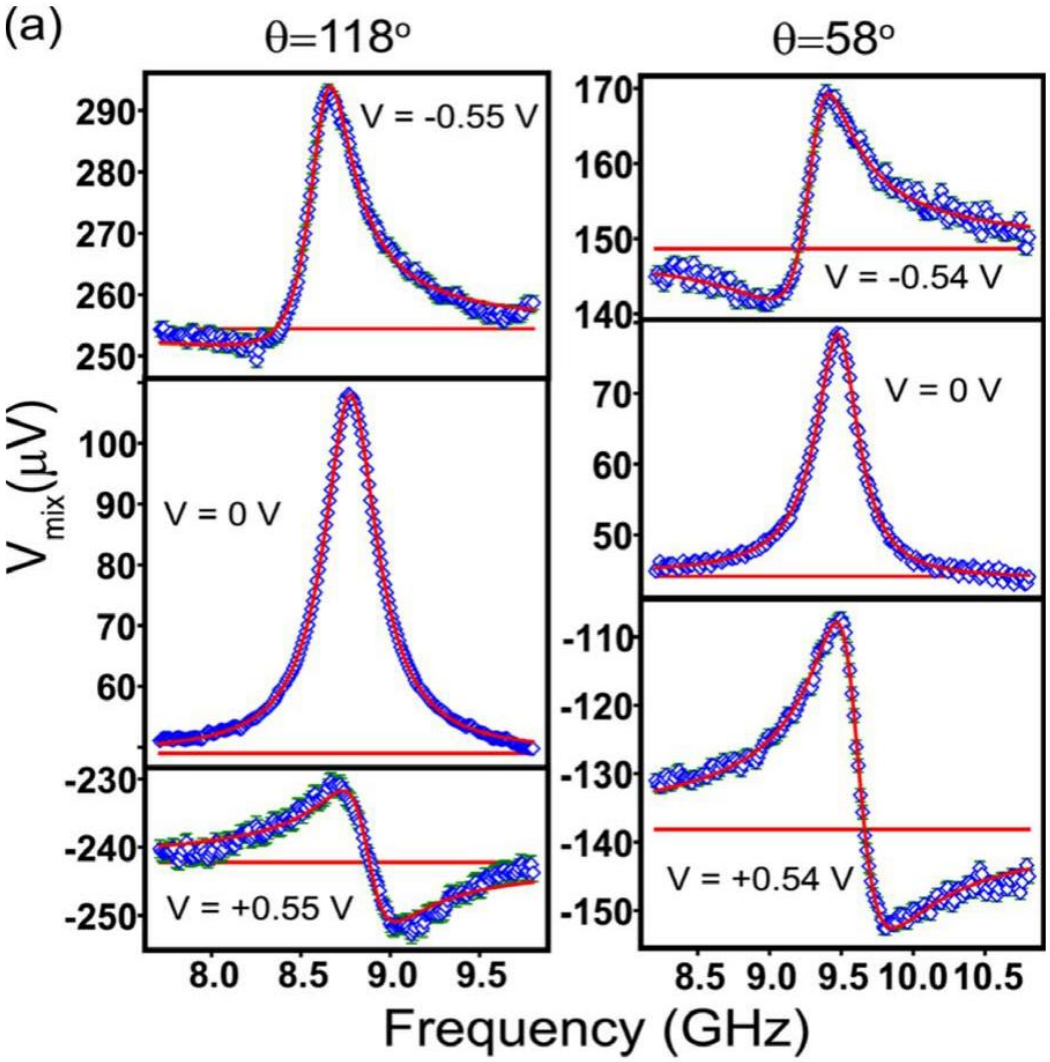

Figure 2.8: ST-FMR spectra at -0.55V, 0, +0.55V for offset angles of θ = 118° and θ = 58°. The ST-FMR spectra is fit to the symmetric and anti-symmetric Lorentzians to further obtain the values of the torkance. (figures from Ref [85].)

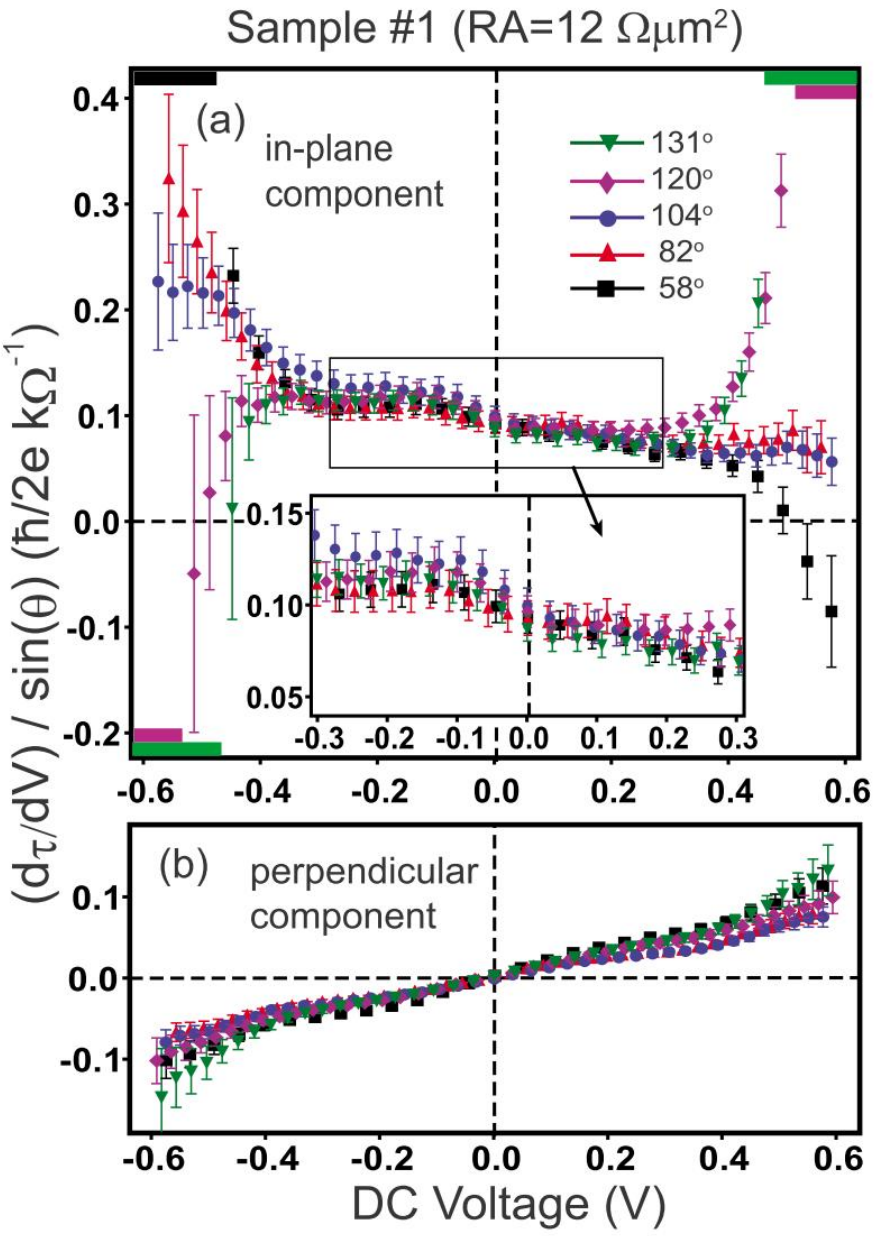

Figure 2.9: The torkance of in-plane and perpendicular component in the CoFeB-based MgO MTJs. (a) is the torkance of in-plane component of spin-torque vectors (anti-damping torque) under various DC voltage bias and angles. (b) is the torkance of perpendicular component. The figure from Ref [85].

In the theoretical prediction, the in-plane torque in a symmetric MgO-based

MTJ is predicted to[75]

$$\frac{d\tau_{\parallel}/dV}{\sin\theta} = \frac{\hbar}{4e}\frac{2P}{1+P^2}(\frac{dI}{dV})_P, \tag{2.1}$$

In addition, the perpendicular component according to Ref. [83, 75] would exhibit a quadratic voltage bias dependence $\tau_{\perp} \propto V^2$. The torkance, therefore, is a linear voltage dependence and has been observed in both Sankey *et al.*[70] and Kubota *et al.*[38].

2.4 Application of Spin-transfer Torque Effect in the Magnetic Tunnel Junctions

Two major applications of Spintronics are nonvolatile memory and nonvolatile of logic circuit operation. Non-volatile memory is preferred than volatile memory is due to its low power consumption and long booting time reading from hard drive or other storage media from personal computer. Both applications are crucial for mobile electronics. For both application, it preferable for multi-terminal device structures, which is necessary for logic operation to communicate information between two different fundamental units and also beneficial for memory application.

Currently, spin-torque effect has been a well-known term and physical phenomena. Another benefit of pursuing multi-terminal structures is to separate read and write terminals. One of the early and important implementation of three structure is in our group[8]. This structure takes advantages of both high MR in MTJs and low resistivity of spin-valve. Read from MTJs terminal and

write through spin-valve terminal. The advantage of this structure concept is simple and can be fabricated using conventional nanopillar fabrication tools. The difficulty of this device structure require experienced E-beam tool user to align one nanopillar over another within 20nm to 30nm accuracy. Late Sun *et al.*[79] utilized spin-pumping and spin-diffusion to induce spin-torque-driven switching in the free layer of the MTJ. Spin-polarized current is injected into a copper layer. The MTJ nanopillar is aligned on the top of the injection. Recently Lui *et al.*[45] discover using spin-Hall effect in nonmagnetic heavy transitional metals could induce magnetic switching. This finding not only enables a whole new area of researches discovering spin-Hall effect materials, but also simplified three-terminal device structure. (see Figure 2.12). Those three-terminal researches are important milestone for next generation spintronic logic devices.

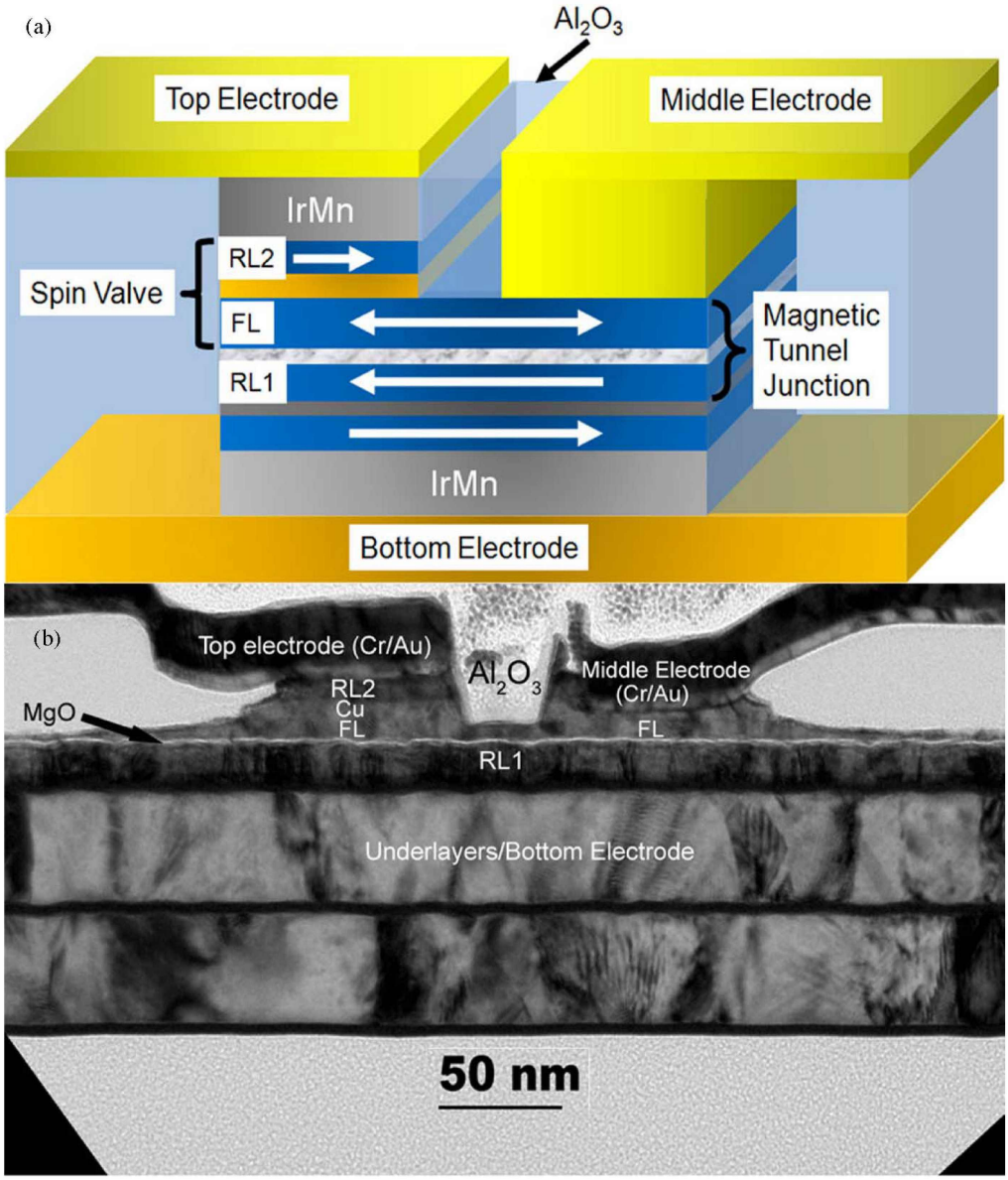

Figure 2.10: (a) Illustration of three-terminal structure concept. The structure enables reading and writing separation from SV and MTJ. (b) Cross-section TEM image from three-terminal structure. Figures from Ref.[8]

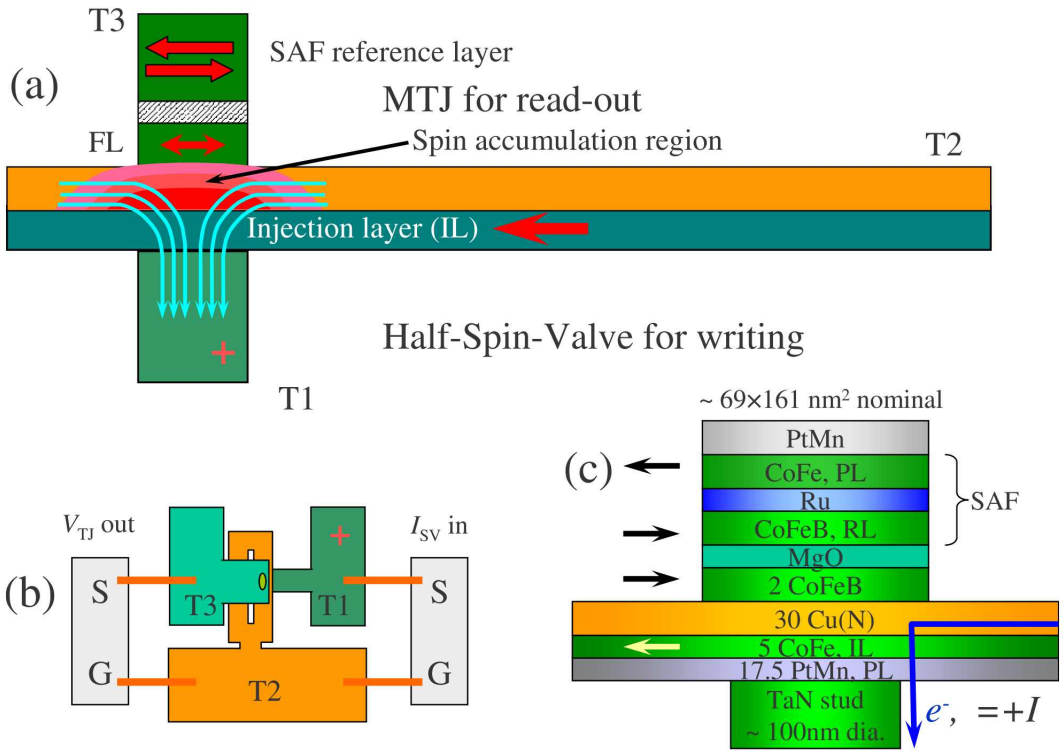

Figure 2.11: Device structure of IBM three-terminal SV/MTJ device. (a) Cross-section illustration image of terminal device. Spin-polarized current is injected from T1 to T2, where underneath the MTJ nanopillar. (b) top view of the device. (c) The side view of the multilayer stack. Figures from Ref.[79]

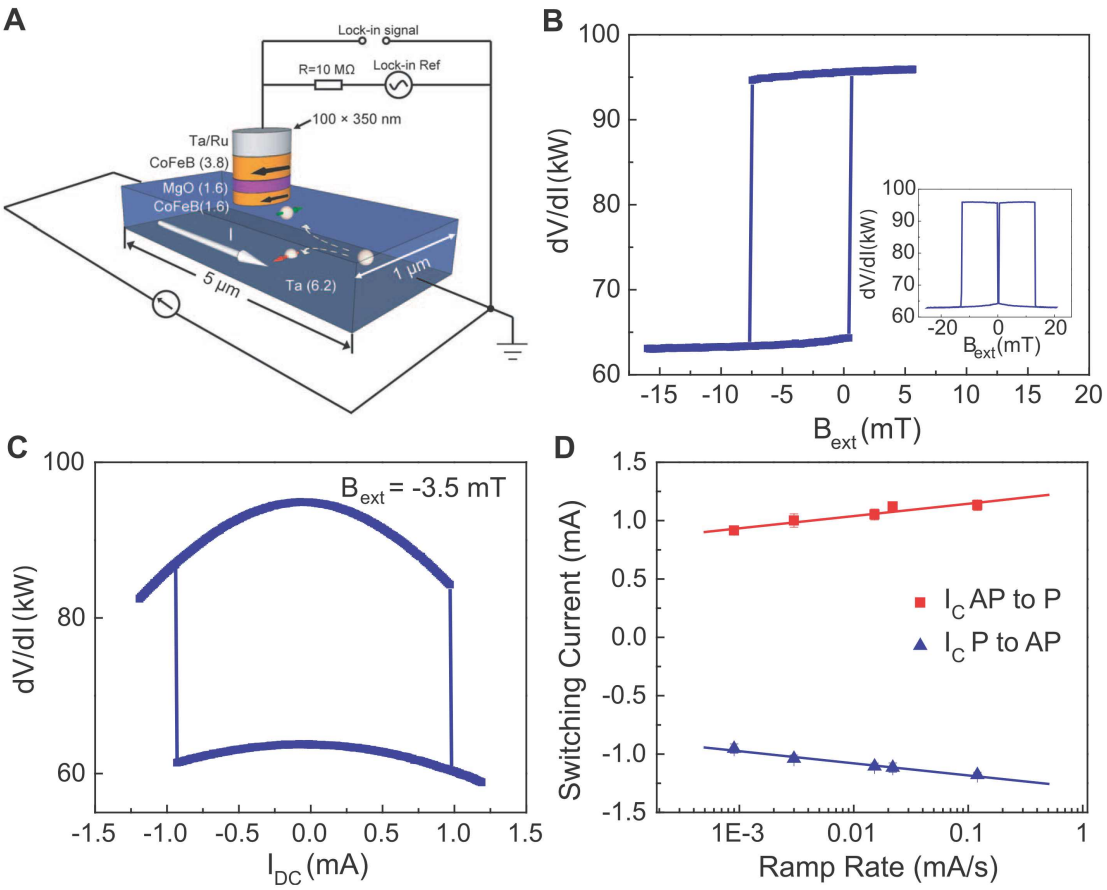

Figure 2.12: Three-terminal structure based on giant spin-Hall effect in Tantulum (a) the illustration of the device structure. (b) field-induced switching in the free layer. (c) current-induced switching and the resistance-switching reading is from the MTJ. (c) Current-ramping rate measurement to estimate the zero-temperature critical current. Figures from Ref.[45]

In the last decades, the discoveries and further understanding of of fundamental physics in spin generation, spin detection and spin manipulation have established pivotal foundation for spintronics and enable the possibility of new industries for MRAM. The discovery of spin-torque switching enables ultrafast magnetic switching[33]. Several start-up companies are established to explore STT-MRAM, such as Grandis (acquired by Samsung), Spin Transfer Technology,

Everspin and etc. or design specific tools for charactering STT-MRAM, such as Integral Solution International(ISI), MicroSense, Nanounity and Mountain Scientifics.

CHAPTER 3

SPUTTERING MGO-BASED MAGNETIC TUNNEL JUNCTION

3.1 Motivation

Tunneling magnetoresistance (TMR) in magnetic tunnel junctions (MTJs) is an important research topic for both scientific interest and industrial applications. Understanding the TMR requires the fundamental understand of spin-dependent transport in the MTJs. Starting from 1995 the discovery of high TMR (24%) in aluminum oxide tunneling barrier [53], there are extensive efforts to discover high TMR magnetic tunnel junctions. Theories have predicted that in FeCo-based MgO MTJs could exhibit very high TMR up to 1000% [11, 48]. In 2004, TMR (>100%) have been reported in FeCo-based MgO MTJs by sputtering[61] and MBE[92]. These researches enable the comprehension of underlying fundamental physics of spin-dependent transport between tunnel barriers and ferromagnetic electrodes. Spin-torque-driven switching in high TMR MTJs, therefore, is an important experiment subject, due to its potential application to spin-transfer-torque magnetic random access memory (STT-MRAM). Understanding the spin-torque effect in high TMR MgO MTJs is a research project of great interest in our group. Due to previous efforts of John Read[67, 66] and Judy Cha[14, 13], we are able to grow high TMR MgO-based MTJs in the AJA chamber through the current in-plane tunneling (CIPT) measurement in collaboration with NIST in Maryland. Since John and Judy's efforts, high TMR CoFe-based MgO MTJs has been shown feasible in our AJA sputtering system. In the wake of this, I have been working on fabricating spin-transfer nanopillar device with high TMR MgO-based materials from AJA.

Through last few years, I have established a reliable and repeatable MgO AJA sputtering procedure and simple lift-off nanopillar fabrication process. In this chapter, I will present the details of achieving high TMR MgO MTJ sputtering process. I will describe the difficulties related to AJA MgO growth at Cornell and how we solved those problems. Next chapter, I will present the lift-off nanopillar approach which enable rapid and reliable nanopillar fabrication (less than 2 weeks). With both techniques, we could easily grow and reliably fabricate high TMR and low RA MgO MTJs for spin-torque studies.

3.2 MgO-based Materials Sputtering in the AJA

3.2.1 Sputtering High TMR MgO-basd MTJs in the AJA Sputtering System: Issues and Challenges

Capable of growing and characterizing high TMR MgO-based MTJs are both essential and indispensable for spin-torque studies in the MTJ. Simply achieving a reliable and repeatable sputtering recipe for high TMR MgO MTJ is highly challenging. First, the MgO target cracks easily even during short sputtering. MgO targets could rupture during initial pre-sputtering in the first few minutes. After MgO cracking, the sputtering condition (sputtering voltages, currents and sputtering rate) constantly change from time to time, since the cracking target is no longer stable and make the sputtering plasma change as well. Besides, the indium paste between the MgO and copper backer melt and flow causing significant shorting in the sputtering gun. This MgO sputtering reliability problem actually affect the experiment progress significantly.

Second, the RA-product is hard to be controlled in a multi-user sputtering system. In order to observe spin-torque effect in the MTJ, enough current densities need to pass through the tunnel barrier. Obtaining low resistance-area (RA) product for low resistance MTJs is necessary. Controlling RA-product within the windows ($<20\mu m^2$)for spin-torque experiments, therefore, is particularly problematic, even with frequent deposition rate calibration.

Third, MgO targets cannot be reused after chamber venting, because the sintered MgO targets from William Advanced Materials (used in our initial MgO studies) changes surface color (figure 3.1a) after sputtering. We changed the MgO target supplier from William Advanced Materials to Angstrom Science, because they provide another kind of MgO targets which is ceramic-like and does not change color after sputtering. The MgO targets from William Advance Materials appear grayish and change to dark gray after venting. The color variation suggests the modification of target surface chemistry and may have a effect on the sputtered MgO qualities. We do not reuse the targets. Another kind of MgO targets are from Angstrom Science. This MgO target looks like ceramic and could also easily cracking during deposition(figure 3.1b). As far as TMR is concerned, both targets have shown high TMR results regardless of the target condition while sputtering with 300W. Although in the beginning of developing MTJ fabrication, we are not sure if the MgO quality or the fabrication process lower than the TMR, since we do not have a reliable recipe or experience from past and research papers do not describe the detail process of MTJ fabrication. In addition to the physical target cracking, we also notice chemical composition of the sputtered MgO layer is contaminated. The secondary ion mass spectrometry (SIMS) show indium signal while ion milling. In term of TMR performance, the presence of indium signal does not degrade the TMR. Besides, while sput-

tered at 300W, the indium used to increase thermal conductivity between MgO and copper backer to dissipate the heat, the indium will melt and short out the sputtering. Those sputtering issues actually have become major issues hindering our experiment progress.

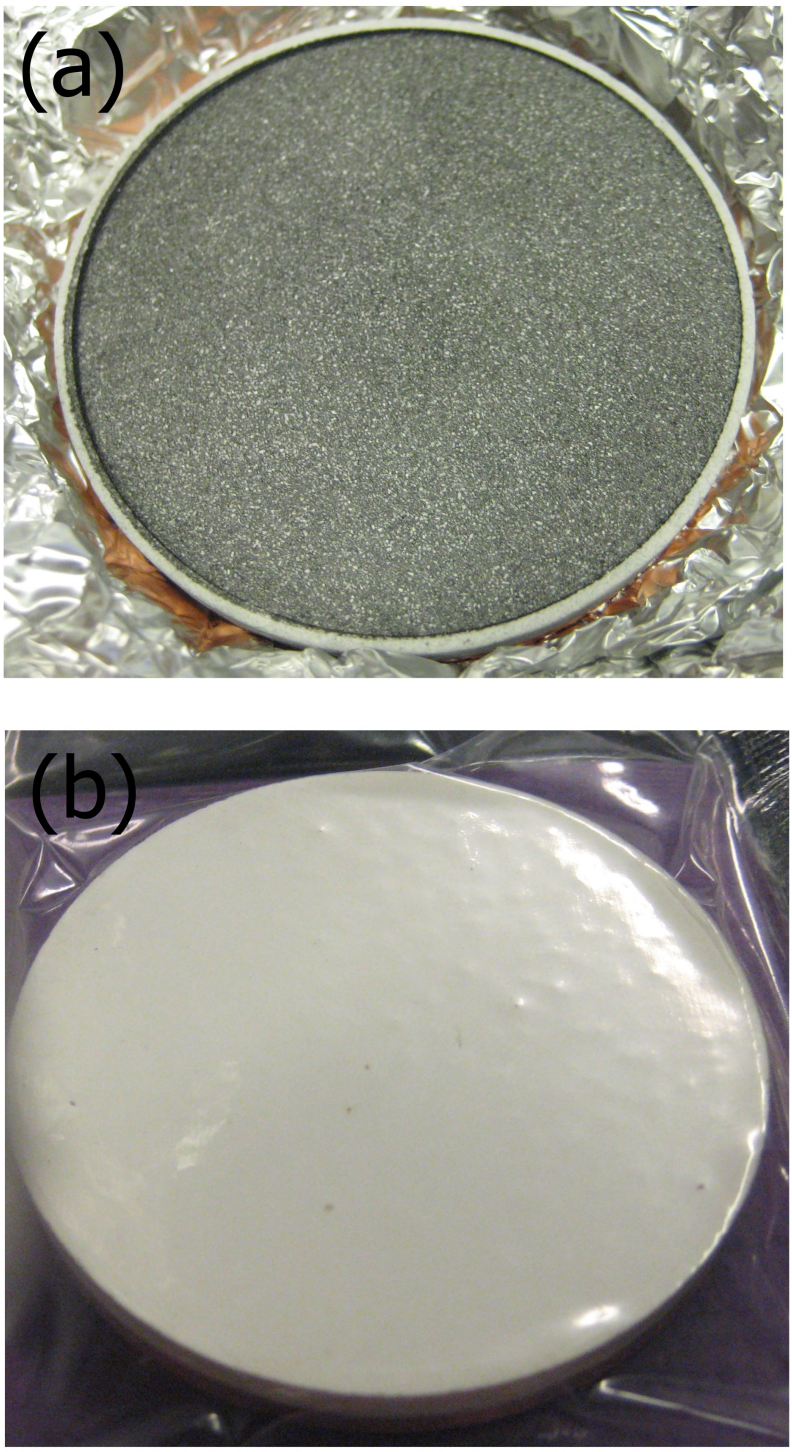

Figure 3.1: sintered MgO targets from two different companies. (a) is from William Advanced Materials. (b) is from Angstrom Science. MgO target color changed from dark gray to light gray after sputtering.

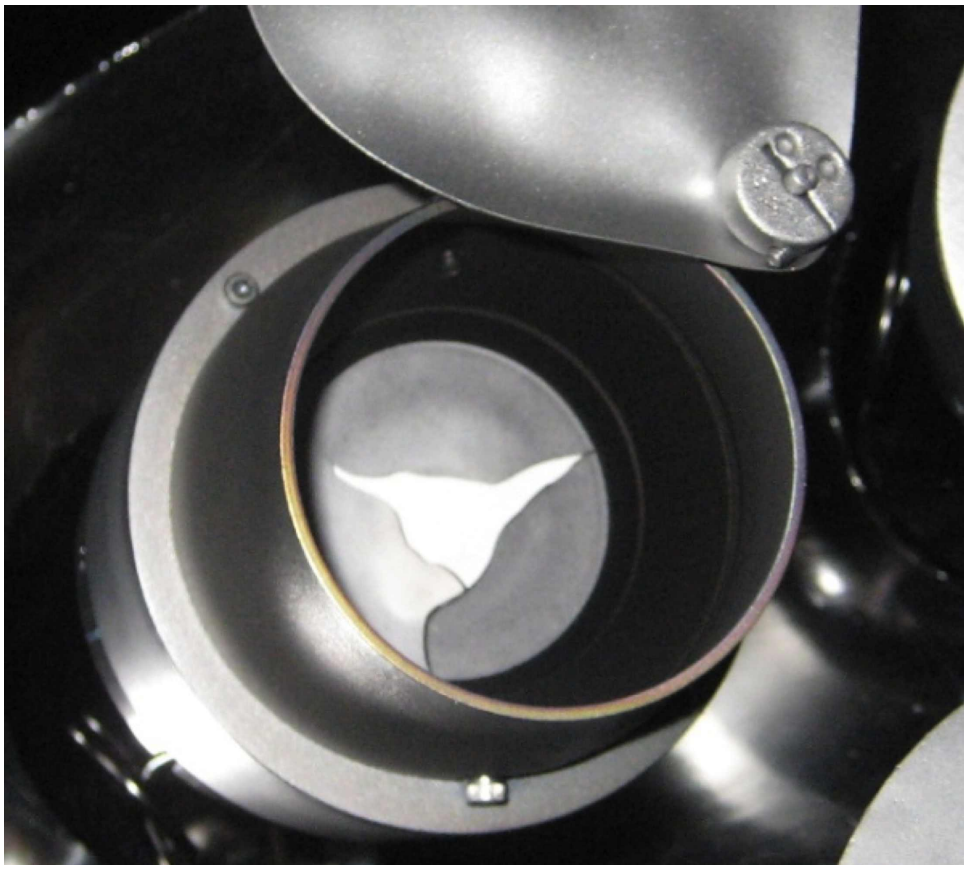

Figure 3.2: Ceramic-like MgO target showing cracking in the sputtering gun after sputtering with 300W. After cracking, sputtering condition change frequently and sputtering rate could vary significantly as well. Continuous using the cracked MgO target cause indium paste melting and flowing into sputtering gun.

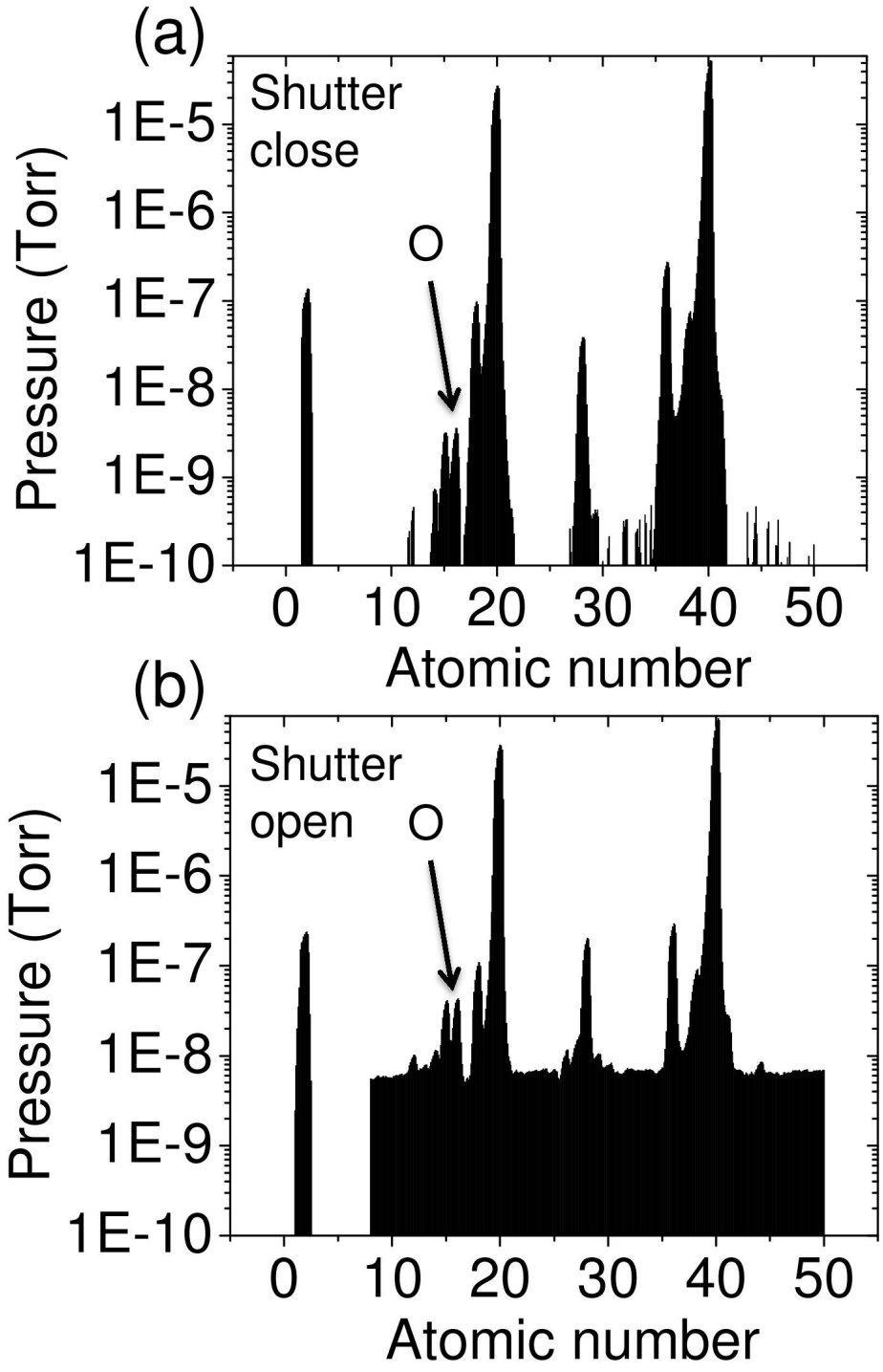

Figure 3.3: Residual gas analysis during MgO r.f. sputtering in the D7 sputtering chamber. (a) shows the residual gas while 200W MgO sputtering gun on with shutter close and (b) with shutter open. Significant increase of O peak increase while shutter open. While shutter close, the O pressure is 3×10^{-9}Torr. With shutter open, the O pressure increases to 4×10^{-8}Torr.

3.2.2 Sputtering High TMR MgO-basd MTJs in the AJA Sputtering System: Solutions

All of above issues can be attributed to a single root problem, which is the high sputtering power density over heating the MgO target during the RF sputtering. Resolving this problem requires lowering MgO sputtering power from 300W to lower power. Low sputtering power resolved the MgO targets cracking problem and indium contamination and provided repeatable MgO sputtering parameters. The question, however, now transformed to if lower power sputtered MgO oxide layer exhibit high TMR like 300W MgO? Other users already have also tested lower power sputtered MgO before my attempt. They did not succeed in achieving high TMR MgO or even not be able to get any sputtering rate at all. Eventually, I was told that the conclusion that lower power sputtered MgO (like 100W) does not be able to produce high TMR MTJs.

Different from others' attempt, I directly fabricated the 100W MgO into MTJ microjunction devices without sputtering rate calibration with 1-mask TMR characterization process (1-mask process will be discussed in the next chapter) and I had obtained high TMR ($\sim$ 200%) for high RA devices. One possible reason why previous attempts does not successful could attributed very slow sputtering rate ($\approx$0.004nm/sec). Calibrating the 100 W MgO deposition rate require much longer (like 30minute) deposition time to acquire accurate sputtering rate. After successfully lowering the MgO sputtering power and established a reliable MgO sputtering condition, we found the conductance vs voltage G-V curve in as-grow sample has shown more asymmetry than 300W sputtered MgO MTJ. We suspect that long MgO sputtering time over oxidized the bottom electrodes.

Second obstacles hindering our progress is achieving accurate RA-product. For spin-torque-driven switching to work, it require RA to be below or approximate to $10\Omega um^2$ to enable enough spin-polarized current to tunneling through the barrier to induce magnetic switching in the free layer electrodes.

To solve this RA issue, I use wedged MgO oxide layer to enable us to control MgO thickness to specific RA range for spin-transfer experiment. Achieving wedged high TMR MgO layer in AJA is not trivial. The first attempt we tried is by stoping the magnetic stage all the time during MgO RF sputtering. The TMR from this procedure is low (20% even for high RA area on the wafers). In the second trial, before we stop the stage rotation, we sputter MgO with at least 30sec stage rotation, before sputtering wedged MgO layer with no stage rotation. This approach has produce high TMR and low RA area on wafers for spin-torque switching experiments.

In addition to AJA MgO growth, we also attempt to grow CoFeB-based MgO MTJs in D7 prep2 sputtering chambers. We were unable to obtain any TMR at all from the multilayer stack sputtered in D7. These two attempts indicate the sputtering condition during RF sputtering MgO to produce high TMR is highly sensitive. Especially first few atomic layer is needed to be just right to produce high TMR MgO layer. Several attempts by Yun Li in D7 prep2 sputtering chamber to test the TMR of CoFeB-based MgO layer does not show any TMR at all, even though the XRD result from the annealed high TMR MgO multilayer stack sputtered in the AJA is almost identical to the XRD result of the same layer stack structure from D7 prep2 sputtering chamber. According to my understanding the Kurt J. Lesker sputtering system in D21, previous post-doc Takahiro Moriyama did test the TMR of RF-sputtered MgO. However, Taka told

me that he didn't observe any TMR at all, but only small signal from AMR.

3.2.3 Seed Layers and Capping Layers

Seed layer for promoting high TMR MgO MTJs is an important topic for us in the early stage of developing MgO MTJs. However, through the years, we have been testing several simple seed layers, we have not observed low TMR (below 100%) due to different seed layers. In the early MgO studies, NIST Maryland performed CIPT technique to characterize the performance of TMR of unpatterned MTJ wafers. In order for CIPT to work, the sheet resistance of bottom electrode layers is required to be at least twice lower than capping layers. This resisitivity configuration allow most of the tunneling current passing through the tunnel barrier and acquire resistance change through electrical measurement with unpatterned films. In the beginning of our MgO MTJ experiments, we have been using [Ta 2nm/CuN 20nm]$_4$ superlattice to smooth the seed layer and promote the epitaxial growth of CoFeB/MgO/CoFeB tunnel barrier and crystallization during annealing. Other than Ta/CuN/Ta superlattice, we also tested using only Ta or Ta/Ru/Ta, in terms of TMR performance, both of them have TMR as high as using Ta/CuN/Ta seed layer. It is worth noting that pure Ta can be used for seed layers for high TMR (>100%) MTJs. Ta, however, is easily oxidized even during vacuum annealing. Oxidized Ta would significantly increase the contact lead resistance and low the TMR if using 2-wire measurement.

As for capping layer, several studies have shown different capping layer affecting the TMR of MgO MTJs. For example, using Pt or Ni in the capping

layer could low the TMR of MgO MTJs. This decrease of TMR can be explained by mismatch lattice structure in the capping and MgO. Obtaining high TMR MgO MTJs require annealing temperature ~350°C, if the capping layer materials crystalized at lower temperature than MgO and CoFeB, it will ruin the bcc crystalline structure of MgO/CoFe interface, which is required for spin-filtering effects for achieving high TMR in MgO MTJs.

Figure 3.4 show the TEM cross-section image on a typical CoFeB/MgO/-CoFeB MTJ sputtering multilayer stacks in AJA. Ta/CuN/Ta superlattice is necessary for obtaining a smooth and low resistance bottom electrodes. However, Ta/CuN/Ta superlattice is not necessary for high TMR MgO-based MTJs.

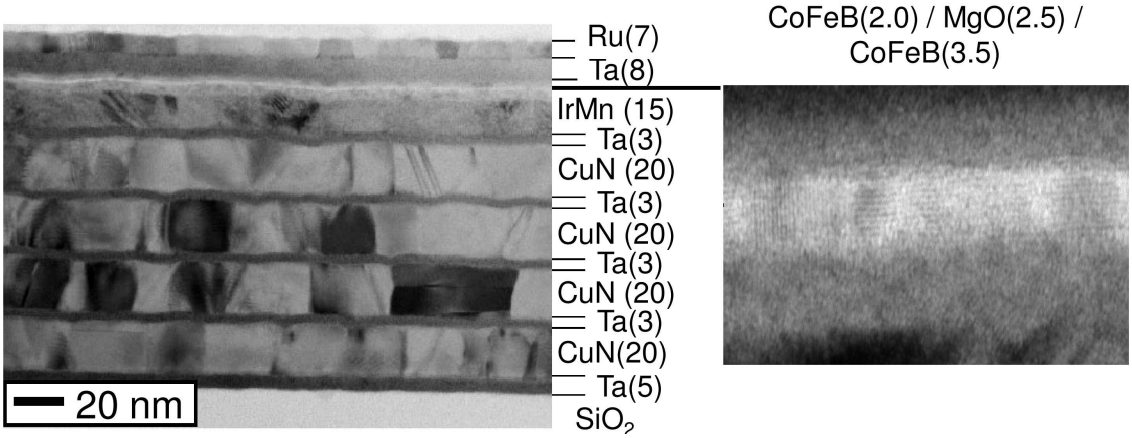

Figure 3.4: TEM cross-section image on a typical CoFeB/MgO/CoFeB MTJ multilayer stacks. Images are from unpublished result from John Read and TEM images are taken by Judy Cha.

3.2.4 Standard Reliable High TMR MgO Sputtering Parameters in the AJA

Briefly, we have achieved a reliable and repeat low RA-product and high TMR (>100%) CoFeB-based MgO MTJs in the AJA sputtering system at Cornell. I have summarized the sputtering parameters and gun configuration in the table 3.1. This recipe has been working very well for most people's experiment requirement to obtain reasonable high TMR MgO MTJs.

Several conditions could cause DC or RF sputtering does not working. The magnetic or normal metal sputtering targets could be used in different gun for DC sputtering. MgO RF sputtering, however, is more sensitive to the target condition (thickness, saturation magnetization, cable impedance and the holder type. MgO RF sputtering works in the gun 2 and 3 and does not excite plasma in the gun 6. Besides, if the plasma cannot be ignited, check if the automatic impedance network is out of auto-adjust region. If yes, change to manual mode and bring the phase and load to middle region which allowing auto-adjust properly work.

Notice the target configurations need to right for a reliable sputtering process. CoFeB alloys have very large magnetization. This kind of magnetic targets need to be as thin as 0.1″ or thinner. Thickness ~0.125″ is difficult to ignite the sputtering plasma without increase the base pressure to 5m 10 mTorr. As for the MgO target, the MgO need to be in the following configuration. The MgO is consisted of three parts. The MgO part need to be configured as 0.125″ thick. A 0.125″ copper backing plate is required to dissipate the heat from MgO. Indium bonding service is also necessary to promote the heat conduction between

the plate. Indium bonding service, however, usually use significant amount of indium paste which will melt and flow at 150°C. Once the sputtering at high power (like 200W or 300W), the indium paste will slowly flow out the gap between the MgO and copper backing plate and cause shorting of the sputtering gun.

Sputtering materals	Gun	Sputtering condiction
Ta 5nm	1	DC Sputtering at 100 W
Ru 20nm	7 or 6	DC Sputtering at 100 W
Ta 5nm	1	DC Sputtering at 100 W
IrMn 10nm	3	DC Sputtering at 75 W
CoFeB 4nm	4 or 5	DC Sputtering at 75 W
MgO 1 to 3nm	2	RF Sputtering at 100 W
CoFeB 3nm	4 or 5	DC Sputtering at 75 W
Ta 3nm	1	DC Sputtering at 75 W
Ru 4nm	7 or 6	DC Sputtering at 75 W

Table 3.1: Standard CoFeB-based high MgO MTJ sputtering multilayer stack structure and sputtering parameters. In the last three years, we have been using 2mTorr and 8sccm for Ar flow.

3.3 Annealing

3.3.1 Conventional annealing for MgO MTJs

Annealing MgO-based magnetic tunnel junctions (MTJs) is necessary to achieve high TMR. Typically, annealing to 350°C will achieve highest TMR in

CoFeB/MgO/CoFeB-based MTJs[92, 61]. Recently, TMR as high as 840% in FeCoB/MgO/FeCoB multilayer structure without IrMn anti-ferromagnetic layer. It is suspected that Mn diffusion into MgO tunnel barrier modifies the electronic structure and affects the spin-filtering effect in the MgO tunnel barrier interfaces. This result considerably lower the TMR performance in the MgO MTJs. Since we focus on the spin-torque physics in high TMR MgO MTJs, we did not optimize annealing recipe, but following the annealing recipe developed by John Read[65], but only simplified the annealing process and time.

Conventionally, we annealed the as-grown wafers in the high vacuum furnace quartz tube at Cornell Center for Materials Research (CCMR) at 350^oC for 2 hours under 10^7 Torr with cooling overnight to avoid any possibility of oxidation. This process is very reliable and repeatable. Annealing in the furnace quartz tube at CCMR, however, cannot apply large uniform field across the a whole 3" wafer. This situation actually has caused significant variation of devices performance over the wafers. In the early stage of our experiments, to resolve this issues, I and Yun Li have builded a quartz tube with ceramic heat inside the tube (see figure 3.5). We also acquire a large permanent magnet with the assistance by Prof. Ralph which could produce uniform external field B = 0.2T. With this annealing furnace, we could achieve reasonable vacuum ($\sim 10^{-5}$Torr) and annealing temperature up to 600°C. This vacuum level is not low enough to avoid surface oxidation of active metals, such as Ta, Cu or Cr, but is good enough for more inert capping layers, such as Ru and Pt.

In addition, we utilized a AlN-based ceramic heater ,which is a new product sold only by Watlow company (see the inset in the figure 3.5). This AlN-based ceramic heater is capable of heating up to 300°C within 2 seconds with ramping

rate 150°C/s. This heater is also utilized in the XPS ultra high vacuum (UHV) system in CCMR to perform in-situ annealing in the UHV chamber (~ 10^{-9}Torr.)

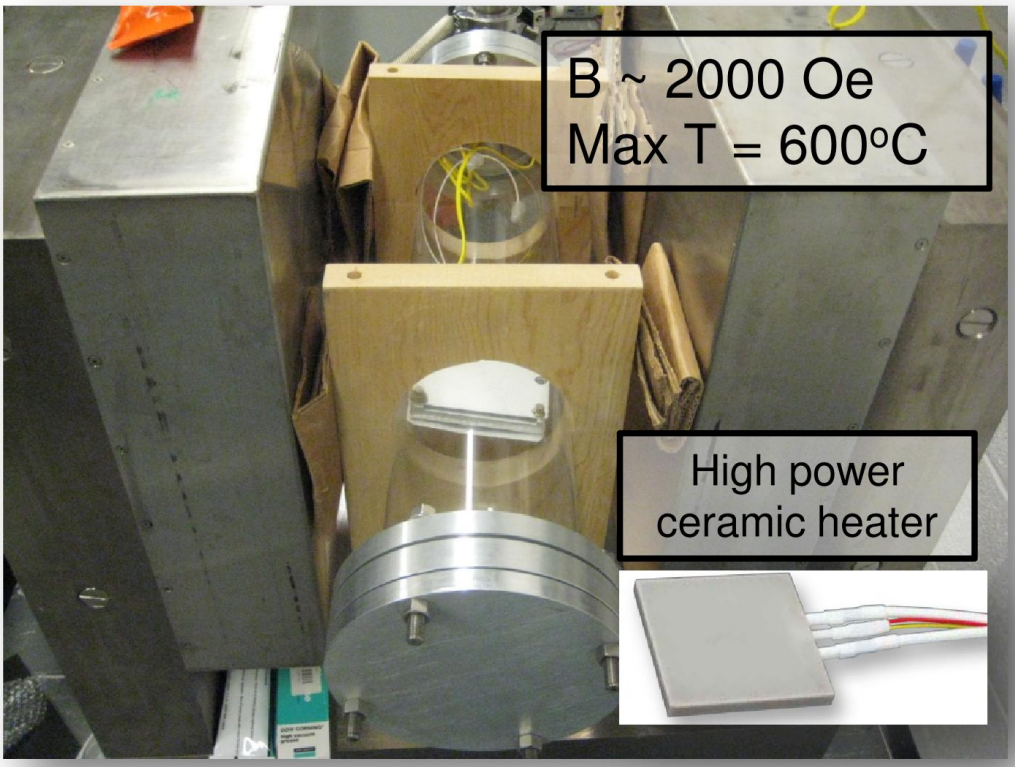

Figure 3.5: The vacuum annealing quartz tube with external magnetic field $B = 0.2T$. The annealing stage is built with a 2″×2″ advanced ceramic heater from Watlow Inc. The ceramic heater is capable of ramping rate up to 150°C/sec to maximum temperature 600°C without cracking the heater. The ceramic heater is able to operate in both atmosphere and high vacuum.

3.3.2 Pre-fabricaiton and post-fabrication annealing

Besides annealing a single whole wafer, we could also anneal the fabricated devices after device fabricated. Instead of doing pre-fabrication annealing (anneal-

ing a whole wafer), we prefer doing post-fabrication annealing. Post-fabrication annealing, however, requires high yield allowing multi-annealing test. The advatanges of post-fabrication annealing enables the studying how coherent tunneling is affecting spin-torque effect in MTJs also how electrodes and tunnel barrier crystallization affect spin-dependent transport in MTJs. In addition, to avoid any oxidation during the post-fabrication annealing, using precious and sputtering inert metals (like Pt, Au, or Ru) as contact leads is necessary to avoid any oxidation in the contact pads. We also found that using evaporated Cr/Au for leads is not good for post-fabrication annealing. The adhesion of evaporated metals is not as strong as sputter metals. Sputtering Ta/Ru or Ta/Pt are very robust and can even sustain air-annealing up to 350°C.

3.4 TMR and RA-product characterization

One of the most difficult challenges I was facing is to characterize the TMR and RA-product of sputtering CoFeB/MgO/CoFeB magnetic multilayer stack for spin-torque experiment, since we do not have CIPT tools or experience of achieving fabrication of high TMR MTJs at Cornell. In the early stage of fabricating spin-torque MgO MTJ nanopillars, it seems to be almost impossible to me. Without confidence of MgO MTJs qualities due to low TMR MTJs performance, or successful high TMR fabrication recipe, it takes me one one year to confirm a reliable fabrication process and high TMR MgO qualities growth is repeatable. One way to quickly test the performance of TMR and RA-product of tunnel junctions is using single-mask process to check TMR and RA. Making single-mask process has enough ΔR require high RA MgO layer ($\geq 10^6 \Omega \mu m^2$) and thick capping layer (≥30nm) to protect the tunnel barrier layer while the

probe engaging with devices. With thin capping layer (≤ 10nm), the TMR could significantly change while probe engaging penetrate the tunnel barrier. Typically the TMR of CoFeB-based MgO MTJs reach the limit while MgO thickness close to 2.5nm[92]. This approach enables quick TMR and RA-product characterization within a day and is especially beneficial for characterizing the TMR performance of new electrode materials like FeV, CoMnSi or Co. For a more accurate determination of TMR and low RA-product of MTJs, 3-masks photolithography process is required for 4-wire resistance measurement to eliminate the resistance from contact leads. For details of 3-mask photolithography process for MTJ fabrication, please refer to Table 3.2 and Ref. [23]

Process	Details and parameters
Photolith 1 (Define bottom leads)	Spin coat S1813 at 2000rpm. Bake at 115∘C. Expose at 5x stepper with 0.85sec exposure time. Develop at 726MIF for 60sec.
Ion milling (Isolate devices)%	Apply heat sink in the back of wafers avoiding overheating of resist. Ion mill away all layer except for resist-protected area. Soaking in acetone for 1 hour to strip off.
Photolith 2 (Define junctions)	Spin coat S1827 at 2000rpm. Bake at 115∘C for 2min. Expose at 5x stepper with 1.3sec exposure time. Develop at 726MIF for 90sec. Exposure time in this step is crucial, since this will define the actual junction areas. Notice that S1827 is prefered to speed up the 150nm SiO_2 lift-off
Ion milling (Define micro junctions)	Stop ion-milling in the middle of MgO to avoid any possible sidewall redeposition.
Evaporated 150nm SiO_2% and lift-off	Evaporate at least 150nm of SiO_2 to ensure the bottom leads and top leads well separated to avoid any possible shorting. Soak wafers in acetone for at least 30min to clearly lift-off SiO_2. Sonicate for 3min. Apply IPA to wash away acetone and blow dry.
Photolith 3 (Top leads)	Spin coat S1813 at 2000rpm. Bake at 115C. Expose at 5x stepper with 0.85sec exposure time. Develop at 726MIF for 60sec.
Sputter top leads	Ta 100W 20min / Ru 100W 10min in the AJA sputtering system. Evaporated Cr/Au or Ti/Au do not work.

Table 3.2: Summary of 3-mask micro junction fabrication process for high TMR MTJs.

CHAPTER 4

NANOPILLAR FABRICATION

4.1 Introduction and Motivation

Nanotechnology has become an important research area which explore the whole new phenomena of nature in the nanometer scales. The giant market of consumer electronic products have pushed both the semiconductor industries and nanofabrication facilities to become more popular and more affordable than ever before. This trend enables the resources of nanofabrication tools become easily accessible and affordable for solid-state experimentalist. Spin-torque (ST) effect is one of the exciting phenomena manifesting itself in the nanometer scale, which benefit from the advanced nanofabrication facilities. In the early development of spin-torque studies, being able to observe and measure ST effect demands fabricating magnetic multilayer stacks into 100nm scales, which enable the the magnetization of magnetic thin films to behave like a single-domain magnetic particle[33].

To probe spin-torque effect, the nanopillar geometry is a crucial device structure, because this device shape not only enable probing the fundamental electronic interaction between ferromagnetic layers, but also facilitate cross-point architecture which is beneficial for high density random access memory application. Fabricating magnetic multilayer stacks into the nanopillar geometry is an important experiment skill for studying spin-torque effect. Nanopillar fabrication, however, is not straightforward. Carbon-based nanomask process require experienced CNF users at least 6 to 8 weeks or longer to complete the process. Simplification of the nanopillar fabrication process, however, is a

necessary challenge and has been a long pursuing goal in our group for spin-transfer torque studies in current-perpendicular to plane (CPP) nanoscale system. Carbon-based hard nanomask approach established by Jordan Katine at Cornell around ten years ago is the most reliable and successful process for making nanopillars. Due to the long nanofabrication time and frequent request of AJA target change, turn-around time for achieving low RA high TMR MTJs has become very long and almost impossible to achieve the requirement of spin-torque MTJ devices. A fast and reliable nanopillar fabrication is an engineering challenge need to be overcome to further advance the comprehension of spin-torque physics at Cornell.

4.2 Produce Lift-Off HSQ/PMMA Nanomasks

Several attempts in our group have been done to simplify the nanopillar fabrication process. Achieving nanopillar size below 100nm, however, is laborious using the conventional carbon-based nanopillar fabrication scheme. Emley[20] attempted using HSQ as nanomasks to replace the PMMA and Cr lift-off steps in the nanopillar fabrication process and demonstrated promising results for using HSQ as nanomasks to make very small nanopillars (50×150nm shown in Figure 4.1and 4.2). Braganca and Liu[7] utilized chemical mechanical polishing (CMP) approach for self-aligned top leads for the nanopillar process, because of CMP tool reliabilities and repeatability, they did not succeed in having a reliable process. Luqiao used thick HSQ as etching mask with a releasing layer and showed good yield with nanopillar devices. Luqiao has demonstrated the possibility of a lift-off nanopillar fabrication process. As we know the feature of exposure theoretically is at the same order of magnitude as e-beam resist thick-

ness. In Luqiao's approach, due to thick HSQ layer (~250nm), Thick HSQ serving as both ion-milling and lift-off mask has the difficulties of achieving smaller pillar sizes. To resolve this issue, I attempt different approach to achieve smaller feature size by using thin HSQ and thick PMMA.

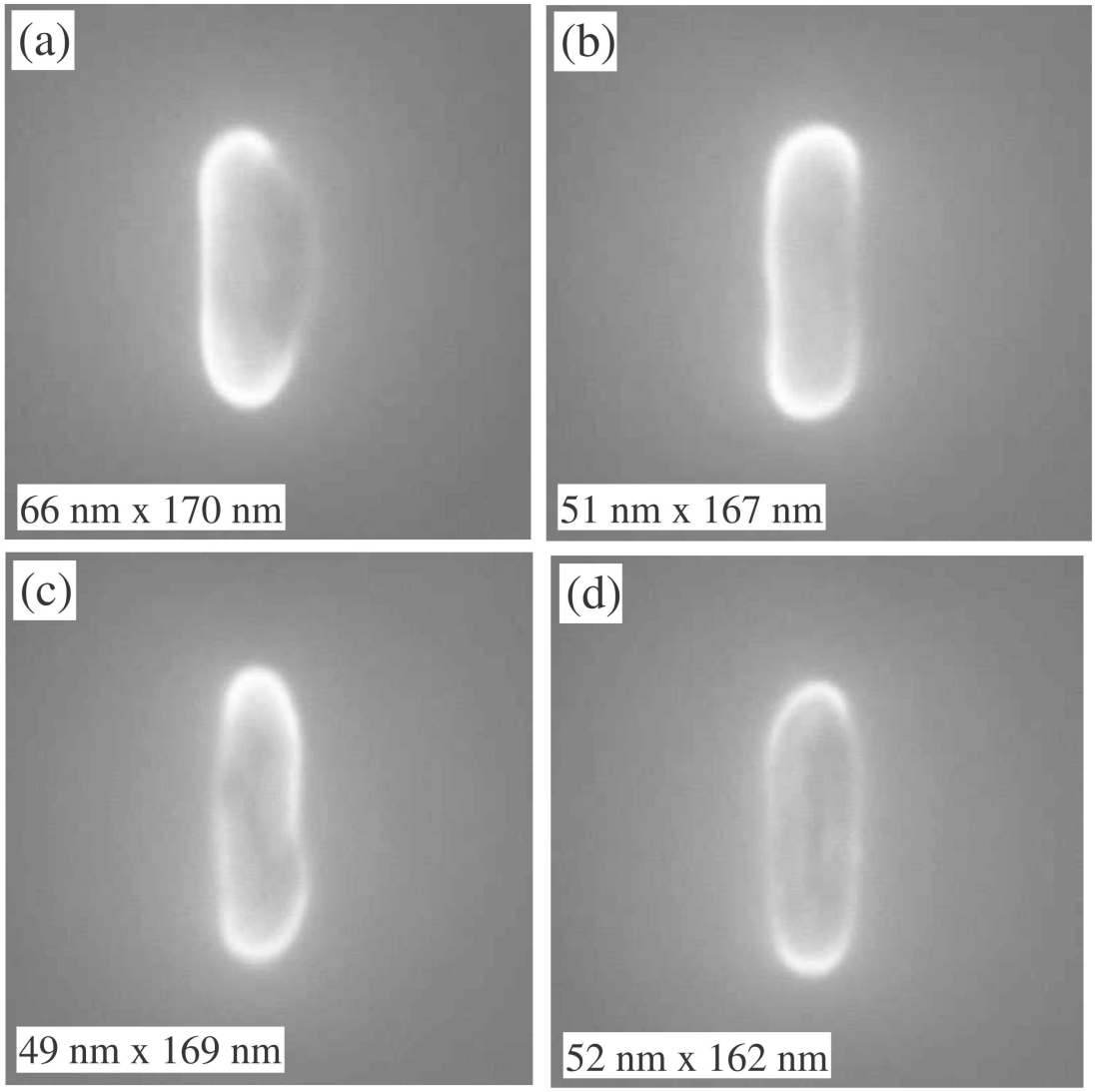

Figure 4.1: SEM images of E-beam exposed HSQ nanomask pillar. This results showed that HSQ is capable of producing single nanopillar feature to 50nm. (From Ref. [20])

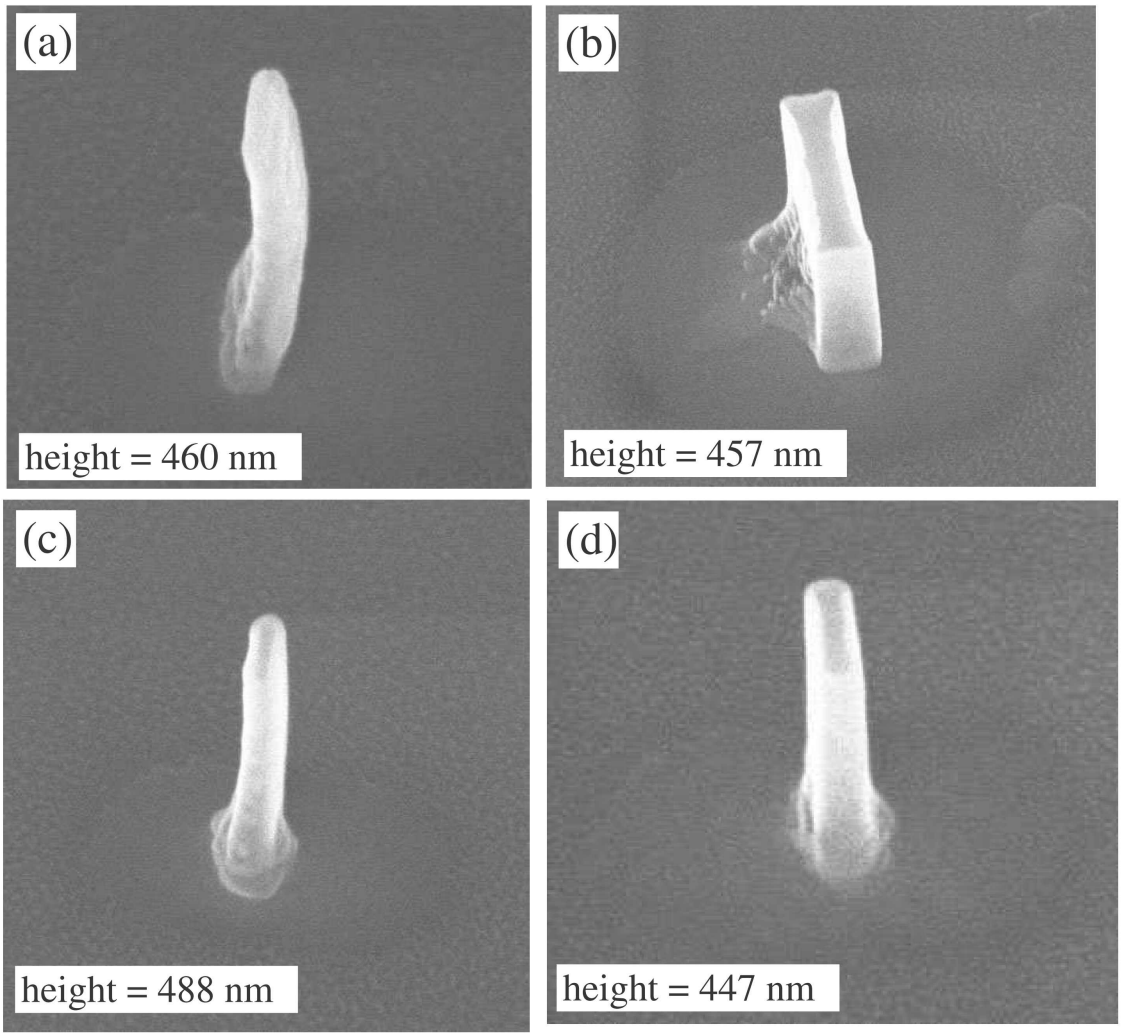

Figure 4.2: SEM images of HSQ nanomasks with tilted angles to reveal the 3D structure of nanomasks. HSQ nanomaks are very long (≈460nm). (Figures are from Ref.[20])

4.2.1 HSQ nanopillar fabrication process

There are two basic approaches for nanopillar geometry fabrication schemes. Figure 4.3 show the process difference in these two approaches. One is using

hard nanomasks to protect nanopillars from ion-milling steps. Then, coating the whole wafer use aluminum oxide to protect and isolate individual nanopillars. The approach could achieve ultra small nanopillar features (like 50nm×50nm or smaller). The concept, however, require precise opening nanopillars process to shoot for small windows to expose the top of nanopillars without damaging the devices. This approach requires at least 6 to 8 weeks processing time for experienced nanofabrication users. Detailed process illustrations, explanations and tool parameters can be found in both Nathan Emely's and Patrick Braganca's thesis[20, 7]. Second approach is using lift-off nanomask which is capable of resisting through ion-milling process and lift-off oxide close to the nanopillar height.

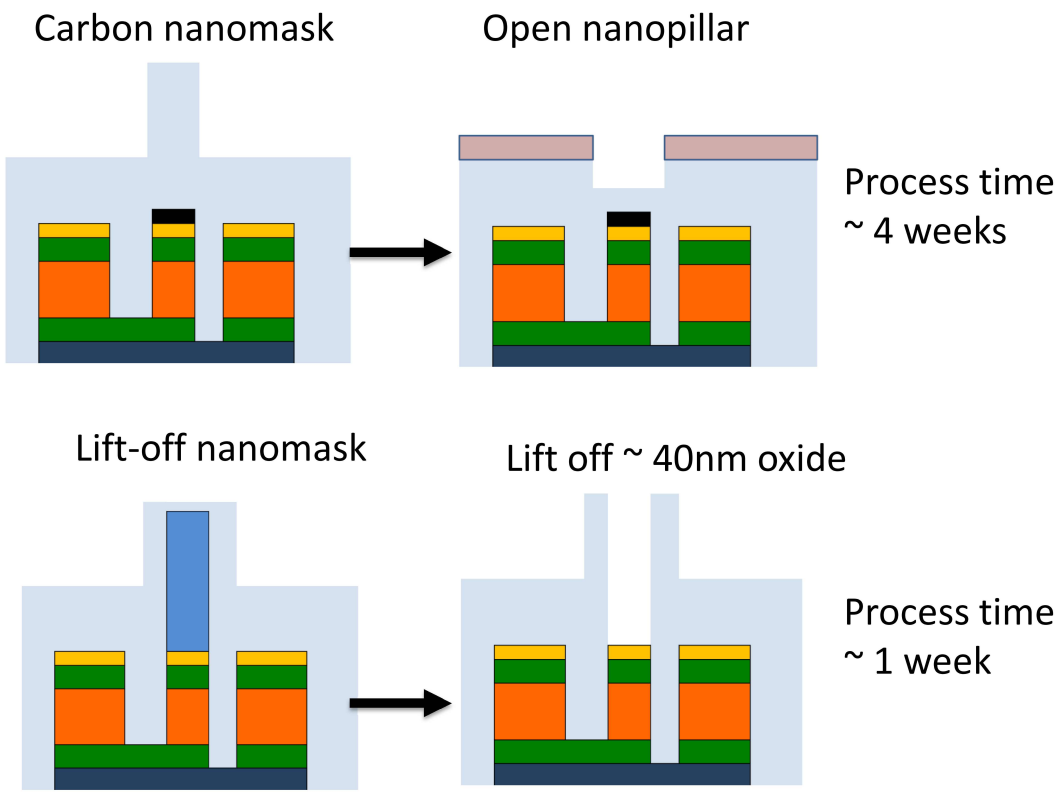

Figure 4.3: Two different concepts of nanopillar fabrication processs approaches. (a) is the hard nanomask approach. (b) is the lift-off nanomask approach.

To achieve features smaller than 100nm, the e-beam resist recipe requires thinner layers. This approach, however, is a trade-off between smaller features and resistance to ion-milling for high lift-off yield. It is required to have a different input to resolve this contradiction. Here, I resolve the trade-off by using a thin HSQ (80nm)/thick PMMA (170nm). In the literature[91], HSQ/PMMA bilayer resist has been shown a good lift-off resist to remove 80nm Cr. Yang *et al.*[91] do not use it as ion-milling etching mask before the lift-off, since in our case we will require HSQ/PMMA serve both ion-milling masks and lift-off masks. I have found after ion-milling, the thick PMMA become very difficult to

strip-off completely and is a serious problem while block the contact between top leads. To solve this issue, I have developed an approach to debugging the process. In the following sections, I will discuss more details of my results of this HSQ/PMMA lift-off process. The carbon-based nanomask process can be found in Nathan Emely's thesis[20].

4.2.2 Electron-Beam Lithograph Pattern Design

Even though the electron-beam lithography design is the first step, but it is the most crucial step in the nanopillar fabrication, which require understanding of the complete fabrication process, including properties of the e-beam resists, e-beam tools, fracturing software, plasma etching, ion milling and so on. Especially, CAD design requires fully understanding of E-beam tools and carefully consideration over pattern size, writing time, field stitching, resolution, electron proximity effect. Therefore, it is necessary and highly recommended to have an experienced e-beam user to discuss the E-beam CAD design before proceeding to exposure. Recently, Cornell CNF prepared an online web pages regarding e-beam pattern preparation guidelines and procedures. This document can be found under the e-beam tools section in the CNF website.

Designing the a "good" E-beam pattern design require consideration over all fabrication steps to have a successful and reliable E-beam lithography. Typically, each nanopillar pattern file is designed and converted individually to ensure each nanopillar located in the center of each exposure. This design approach complicates E-beam tool job files and sometimes it is hard to find the error in the syntax of E-beam job files. Instead, I draw all features in a die in

a single L-Edit CAD files. This way reduces the possibility of making mistakes compiling E-beam job files. In addition, due to the improvement of fracturing software (Layout Beamer), we now could easily center individual nanopillars in the center of each exposure field. We could use single die as CAD drawing unit, instead of drawing an individual nanopillars its own CAD files. This approach saves tremendous amount of time and avoids possiblilities of converting mistakes. Designing whole die in a single CAD file also allow more complicated pattern structure without extra efforts. In addition, due to the advanced of E-beam software, we could directly define dose to each GDS number. This approach has enable easy dose check to figure out a good dose range for nanopillars and have more advantages over single assigning dose in the E-beam job files in JEOL.

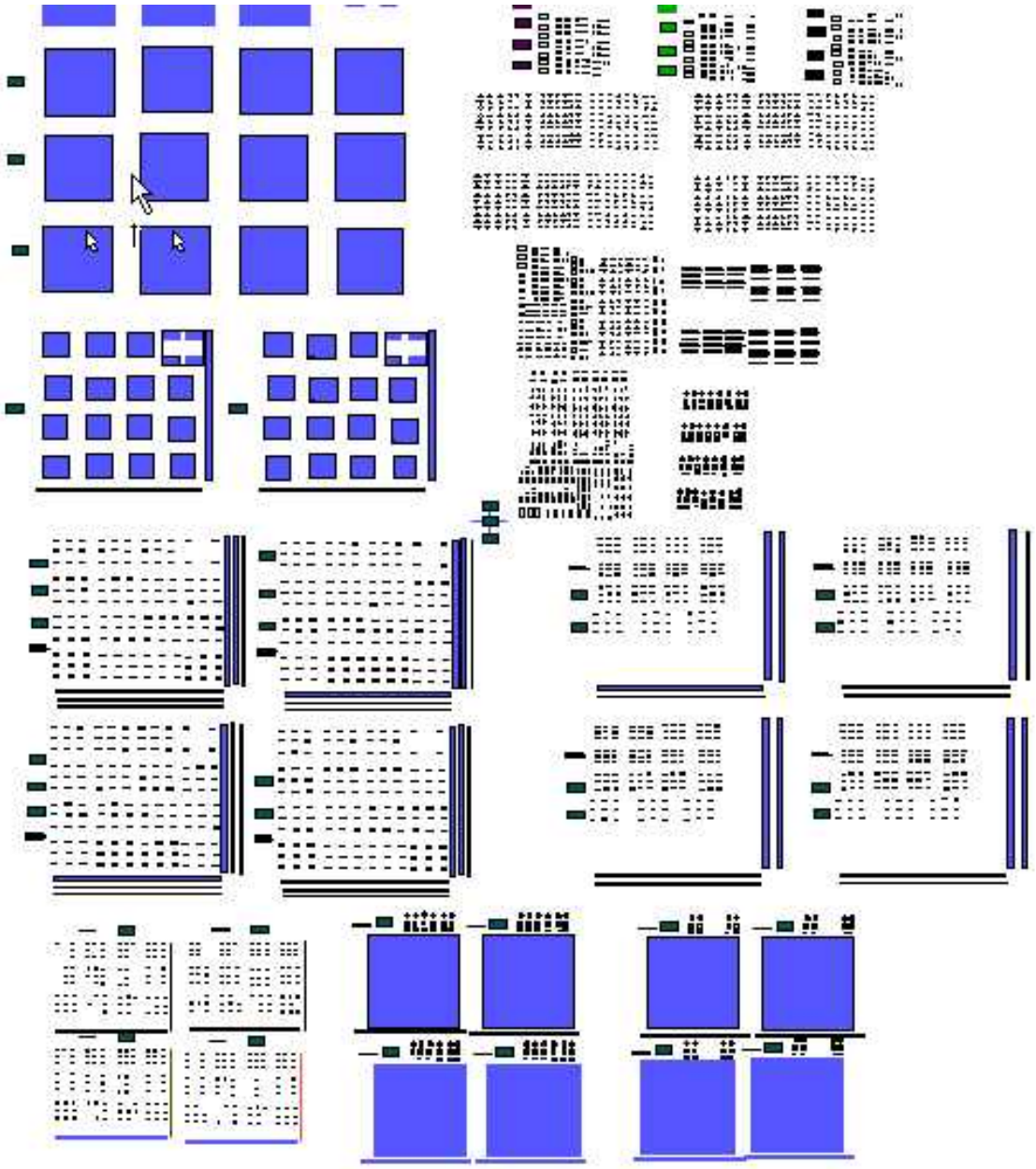

Figure 4.4: Large dot array design by L-Edit. The size of the whole dot array is around 100μm. Periodic array pattern can be easily identified with eye and optical microscope. Since E-beam exposure time is proportional to exposure areas and the number of stage movement, this design only increase the total exposure time by 5 minutes for a 9×9 die in a 3″ wafer

One critical parameter is the aspect ratio for the HSQ nanomask. To achieve high aspect ratio requires precise control of e-beam exposure. The new converting software in CNF, Layout BEAMER, enables the precise control of every exposure and stepping field in a graphical way. In order to produce high aspect-ratio nanopillars, we will need to achieve high aspect-ratio of HSQ nanomask. Figure 4.12 show the AFM images of the HSQ/PMMA nanomask and the nanopillars after ion milling.

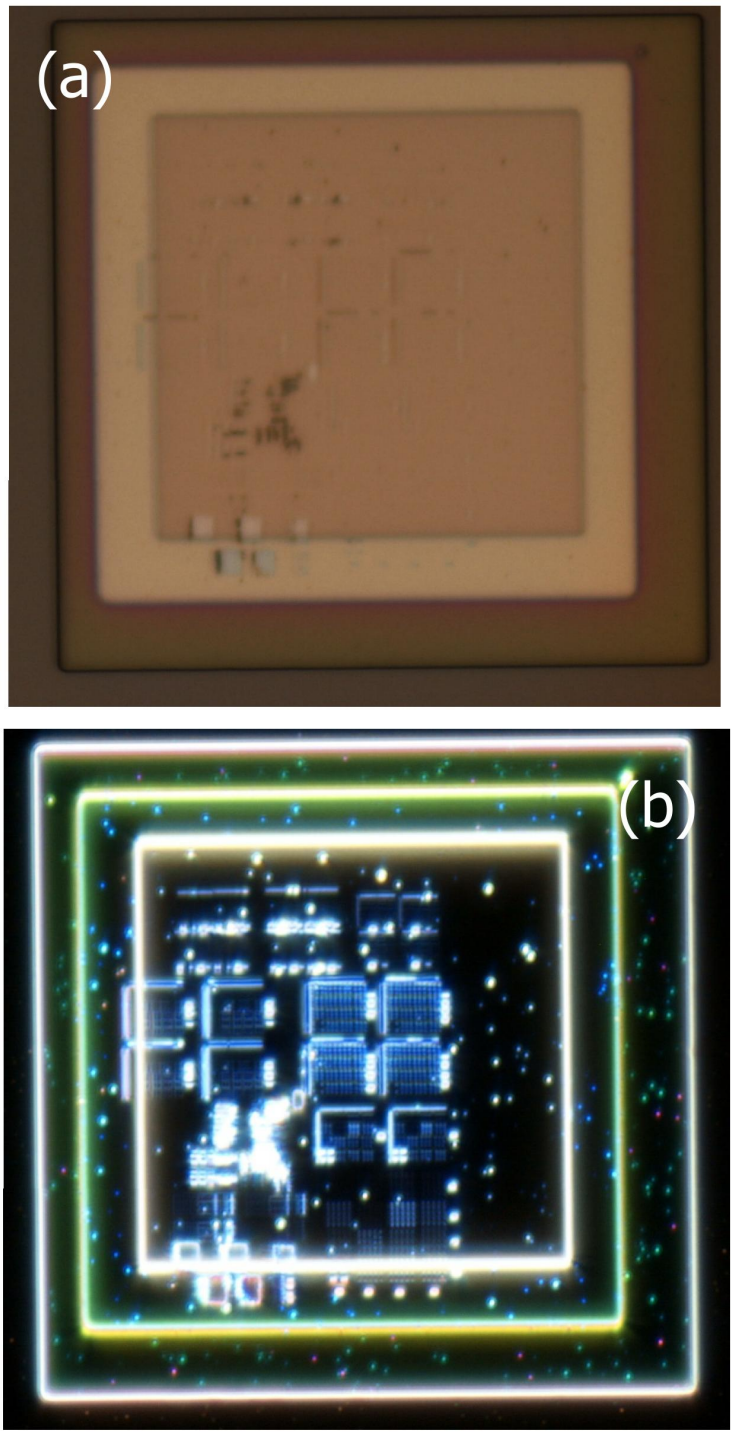

Figure 4.5: Large dot-array assisting quick inspection with microscope to test the lift-off yield. (a) is the bright-field optical image. (b) is the dark-field optical image. Small features on the order of the nanometer scale can be observed clearly using dark-field.

In addition, one time-consuming characterization in the nanopillar fabrication process is the characterization of nanopillars. In the past, to characterize the e-beam exposure result require SEM to check nanopillar exposure. To speed up the characterization, I take advantages of large field size in the JEOL9300 (1mm×1mm) to enable simple nanopillar characterization. Very large dot array is centered in each die. This approach let us inspect if an e-beam exposure is successful or not by simply using optical microscope. Figure 4.5 show the large dot array in each die of the wafers. Figure 4.5 (a) is the optical bright field image and (b) is the optical dark field image. Under dark field, nanopillar array can be easily identified and spotted without SEM characterization.

4.2.3 E-beam Resist Preparation for HSQ/PMMA Lift-off Nanopillar Fabrication Process

The thermal treatment of HSQ/PMMA lift-off nanomaks has significant effects on the lift-off yield. It is necessary to follow to recipe closely for inexperienced user. I will discuss the properties of the E-beam resists and present the recipe for HSQ/PMMA lift-off nanopillar process. I have found that reducing thermal annealing time for PMMA and HSQ could improve lift-off yield and reduce sonication time. Typically, PMMA is heated on a 170°C hot plate for 15min before E-beam exposure to ensure the solution liquid fully vaporized. This annealing recipe is to use PMMA as E-beam resist and to activate the sensitive of PMMA to electron beam. However, after long heating time, PMMA is difficult to be completely removed without any reside. Usually, PMMA can be clearly removed if used as E-beam lift-off resist with bilayer under-cut profile. Because large-area

Process	Details and parameters
Spin on omnicoat twice	Ramp at 1000rpm, spin at 2000rpm and back on 180^{o}C for 1min. Repeat this twice.
Spin on 4% 495k PMMA	Ramp at 2000rpm, spin at 4000rpm. Back on hot plate at 180^{o}C for 1min.
Spin on 6% HSQ	Ramp at 2000rpm, spin at 4000rpm. Back on hot plate at 180^{o}C for 1min. (6% HSQ can be used without defrost.)

Table 4.1: E-beam resist preparation procedure

of PMMA extends through the whole wafer, lift-off of PMMA could be very clear without residues. Here, only HSQ is served as E-beam resist and transfer pattern over PMMA underneath with oxygen plasma. Only nanoscale area of PMMA layer is left. Under this condition, PMMA cannot be removed clearly without violent lift-off procedure. To optimize nanomask lift-off yield, we use the Remover PG which is developed for clean scum-free removal of SU-8. (The detailed lift-off recipe is presented in the later section). The process details for E-beam resist treatment is summarized in the table 4.1.

4.2.4 HSQ/PMMA Nanomasks

I have test the limit of the smallest features can be achieved using the HSQ/PMMA nanomask. Figure 4.6 show the SEM images of HSQ/PMMA nanomask. This result demonstrated that the HSQ/PMMA nanomask could achieve aspect-ratio as small as 1:3 (≈40nm×140nm) and achieve the nanomask

feature on the order of 40nm for 6% of HSQ resist. GeometryTests are also done with 2% HSQ resist. 2% HSQ/PMMA nanomasks has low lift-off yield (lower than 10%) and not applicable for the lift-off nanopillar process.

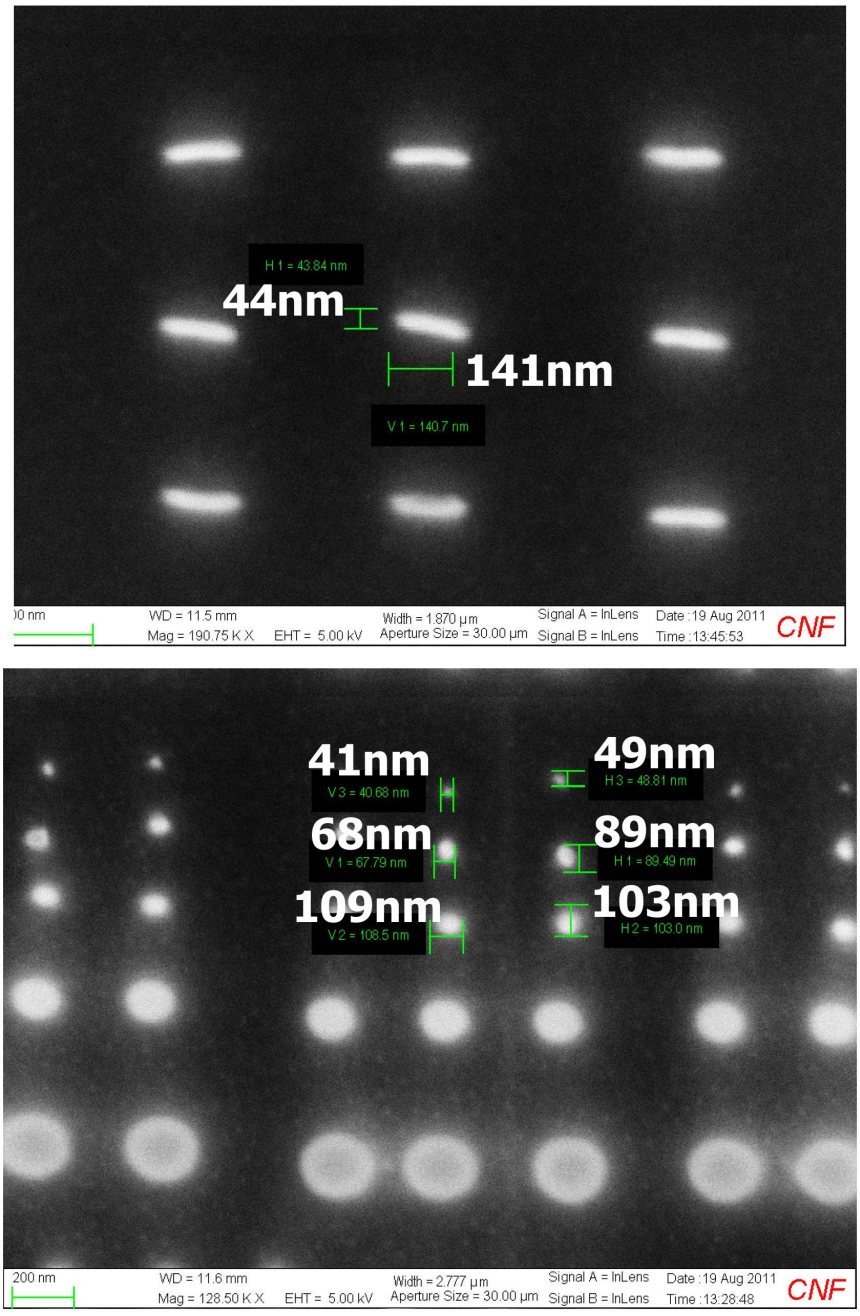

Figure 4.6: SEM images of HSQ tri-layer nanomask. (a) This SEM image exhibit the HSQ/PMMA nanomask with 5nm×100nm design in CAD file. The SEM image shows ~44nm× 141nm (1:3) aspect ratio. (b) The image show the capabilities of HSQ/PMMA nanomask can be as small as ~40nm.

Another important issue is the choice of E-beam tools. JEOL6300 is a new e-beam tool which is designed for fabricating very small features on the order of 10nm or below with 5th len aperture correction. To acquire 10nm accuracy, it is required to change 5th len in JEOL6300 other than the default 4th len. Unfortunately, adjusting 5th len requires good experience of tuning stigimation and wobble of the electron beam in JEOL to optimize the resolution. Because of this manual adjustment, it have made the multi-user JEOL6300 less reliable, due to the significant instabilities and inconsistency of users' adjustment. To avoid that problem, I choose JEOL9300 instead of 6300.

4.3 Pattern into Nanopillars: Ion-milling and Lift-off Oxide

4.3.1 Ion milling

Ion-milling, oxide evaporation and oxide lift-off are crucial steps in the fabrication, since those steps are irreversible steps in the nanofabrication process. Once one incorrect parameters are used in those steps, the wafers might be no longer possible to produce working devices. Detailed parameters are summarized in the table 4.2. In this section, I will summarize our experiment and results from several important references related to high TMR MgO MTJ fabrication.

First issue need to be aware of is the sidewall re-deposition. Sidewall re-deposition has been a known issue for spin-torque experiment in the ion-beam milling process. Ozatay *et al.*[60] has shown that sidewall re-deposited oxide in Py/Cu/Py spin-valve nanopillars affects both field-driven and spin-torque-driven switching of nanomagnets. The sidewall re-deposition in the MTJ could

further short the tunnel barrier and lower the TMR. In the literature, there is almost no researches addressing this issue or detailed recipes, but only briefly mention that the fabrication is done with conventional photolithography and leave all the detail for low RA and high TMR MTJ fabrication process. The first few MTJs devices (wafers from John Read) fabricated at Cornell by me and Yun Li exhibit very low TMR (≈20%) even in the annealed wafers. The TMR signal of those low TMR devices can be enhanced to ≈100% after slowly applying large currents, which indicating the MTJs are shorted. Avoiding sidewall re-deposition, therefore, is an issue needed to be resolved for achieving high performance MgO MTJs at Cornell.

Before I addressed how I avoid all the factors of shorting the MTJ, I would like to discuss the details of sidewall shorting. Figure 4.10 show the relationship between the shape of the photoresist and the profiles of sidewall re-depositon. During the ion-milling process, while Ar ions are accelerated toward the wafers, the sputtered-out materials could adhere to the sidewall of the photoresist, as well as the pillar structure itself. While the pillar structure is with a ultrathin tunnel barrier, even small amount (~1nm) of materials re-deposited to the sidewall could induce significant shorting problems, since the tunnel barrier is approximately the same thickness or thinner (~1nm). Therefore, for low RA MTJs for spin-torque experiment, sidewall shorting is a more significant problem than high RA junctions.

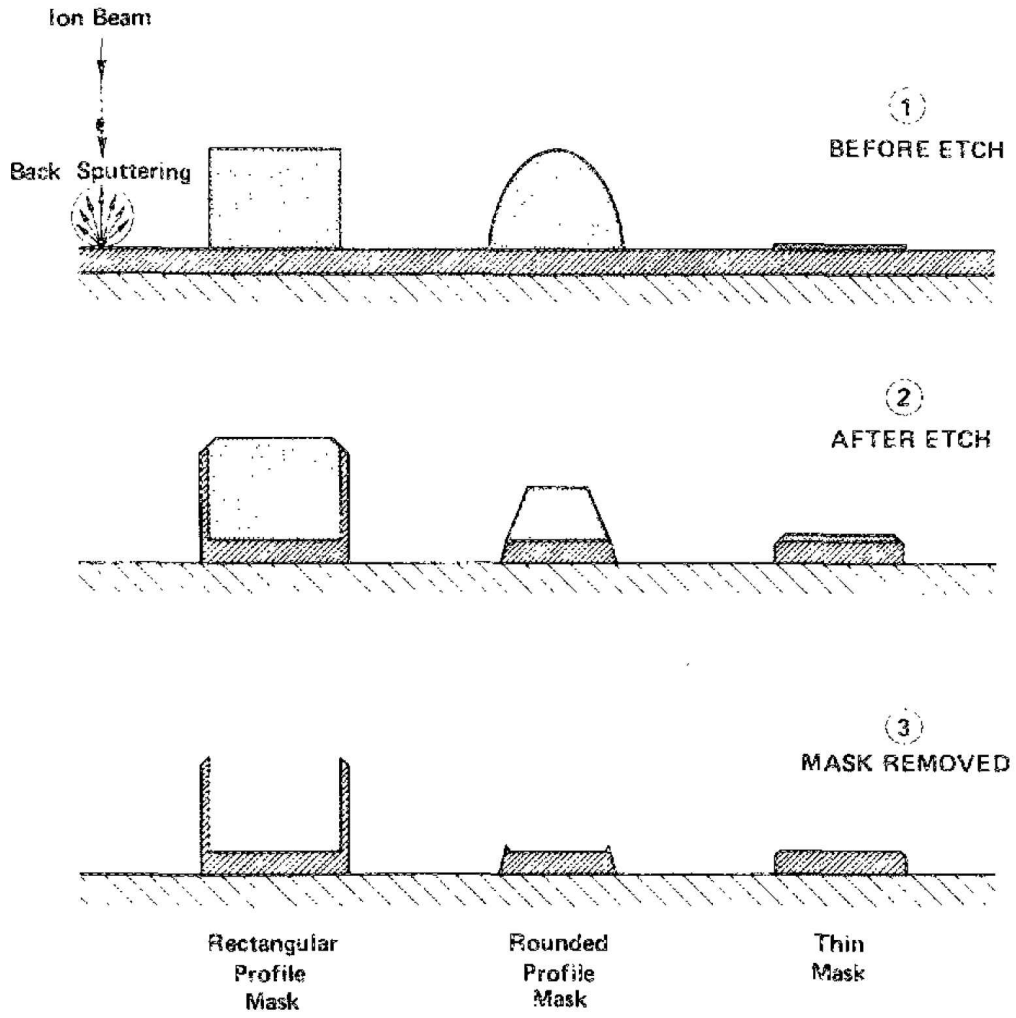

Figure 4.7: Illustration images of sidewall re-dposition from ion-beam milling.(Ref.[42])

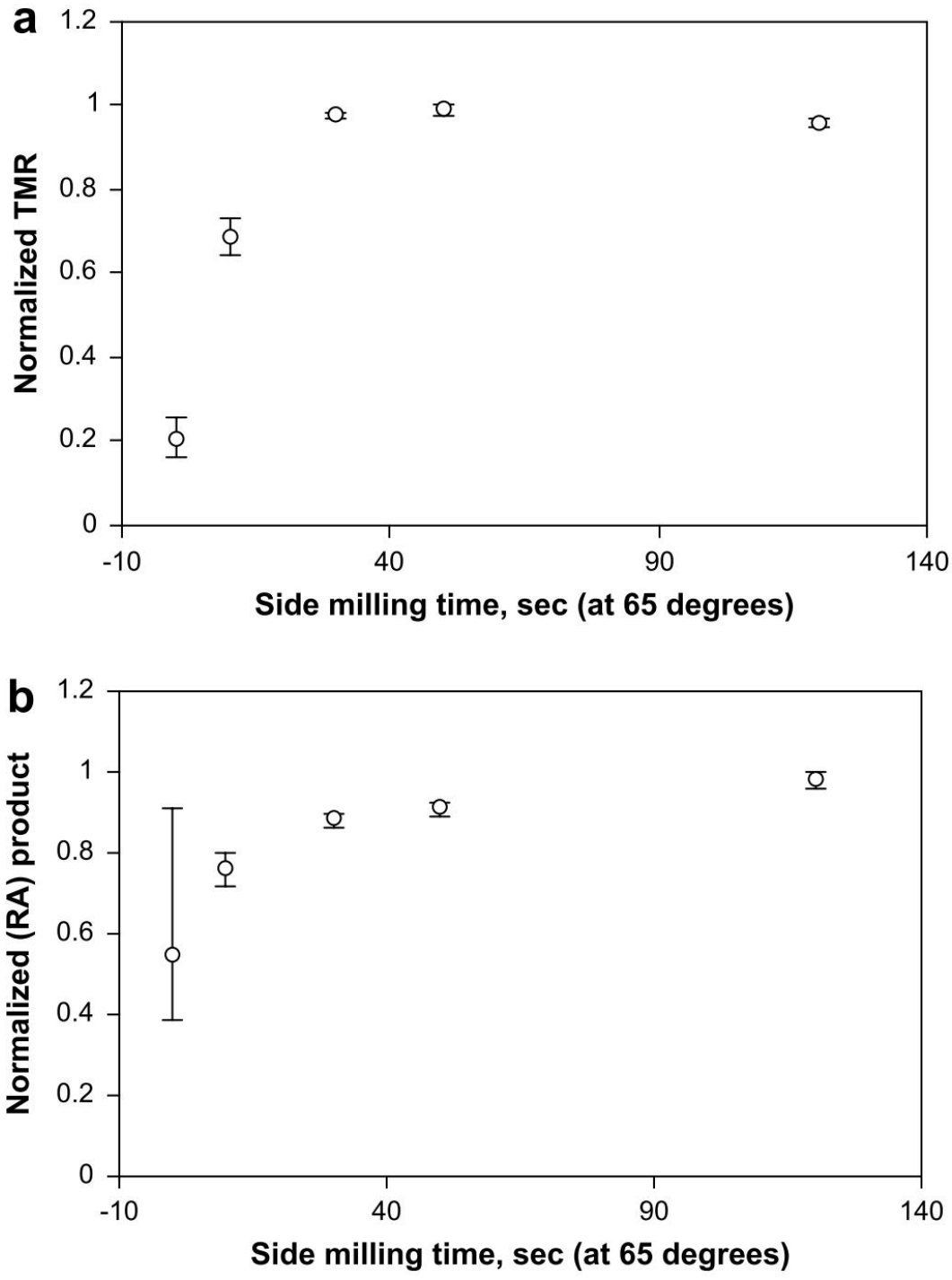

Figure 4.8: Normalized (a) TMR and normalized (a) resistance×area (RA) product as a function of second side ion-milling time at angle 65°.(Ref.[62])

Basically, there are two different strategies to avoid sidewall shorting problems. First approach is to avoid any sidewall re-deposition in the beginning. To achieve this we could stop ion-beam milling in the middle of tunnel barrier and perform a very short sidewall cleaning by high-angle ion-milling. Stopping ion milling in the middle of ultra-thin tunnel barrier is difficult and almost impossible without the end-point detector. Our new ion-milling system equipped with second ion-mass spectroscopy (SIMS) allowing us accurately determine the end-point of our ion-milling step. What we have found is that if stopping ion-milling in the middle of the tunnel barrier and the bottom electrode, we could have TMR as high as ≈200% in high RA micro junctions. Once over etching into IrMn layer or even further into buffer layers, the TMR will start decreasing significantly. Figure 4.9 show SIMS from ion-milling the magnetic tunnel junction layer stack in the device isolation fabrication step. I usually stop in the transition from MgO to bottom CoFeB electrode. This transition time usually take 1 to 2 minutes. Note that even side milling is helpful for enhancing TMR performance. However, Katine *et al.*[34] found that long side-milling could cause edge damage and decrease the GMR performance in spin-valve sensor.

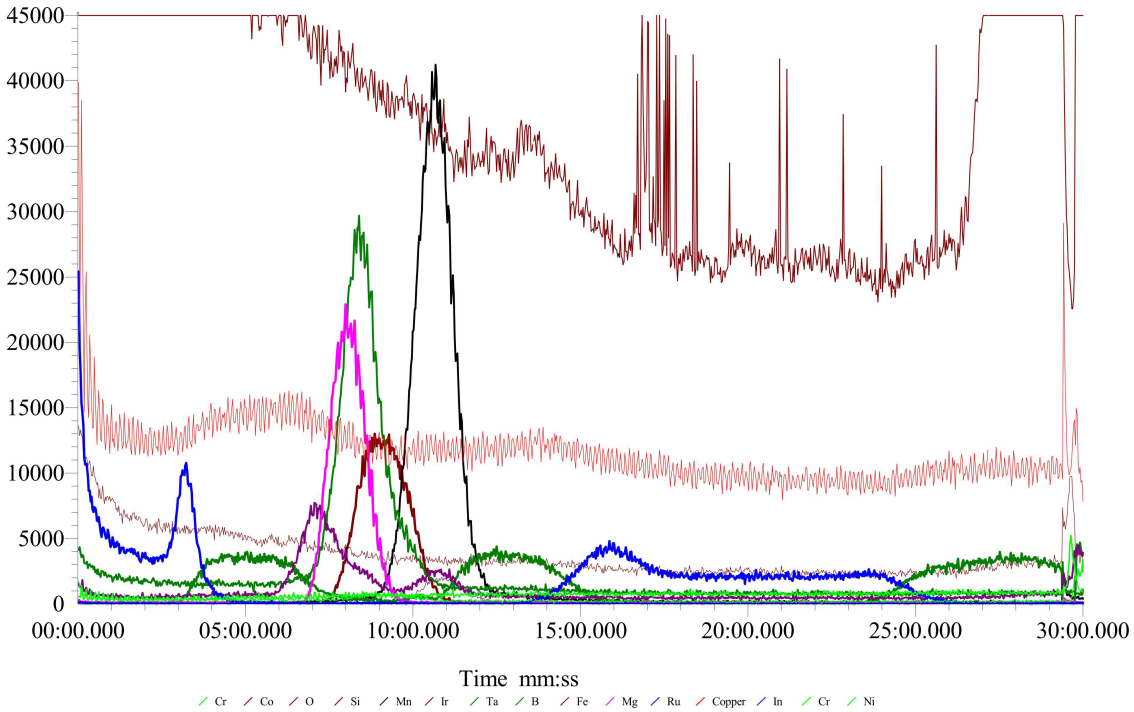

Figure 4.9: SIMS result from a typical MgO-based MTJ devices.

Recently, Peng *et al.*[62] carefully examined how the ion-beam milling recipes affect TMR and how to avoid sidewall shorting problem. They show that TMR cannot be fully recovered by sidewall cleaning. Our results also show the same conclusions. Instead, stop ion-beam milling in the middle of tunnel barrier is a better and reliable approach in our experiment results.

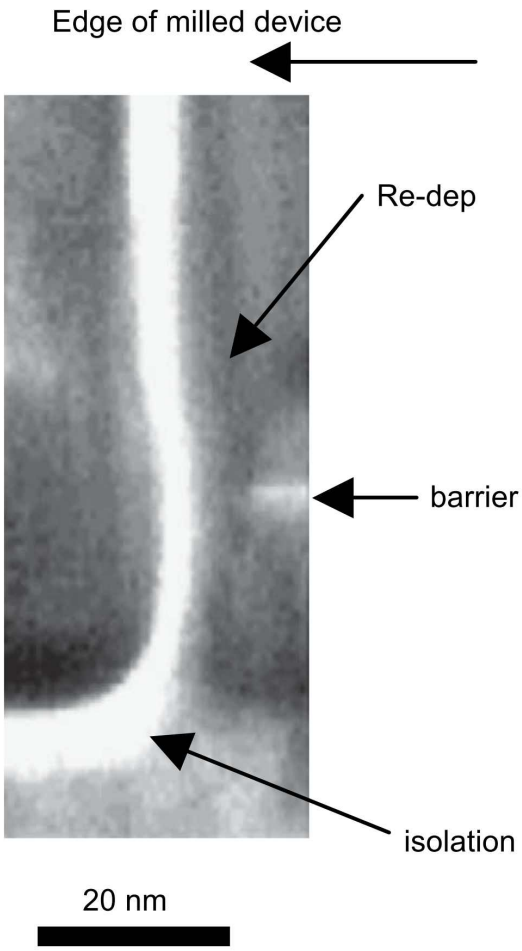

Figure 4.10: Side re-deposition across the tunnel barrier shorts the device and lower the TMR. Using high-angle ion milling can not fully recover the TMR. The thickness of the metal side-redeposition is thicker than the tunnel barrier. (Ref.[62])

4.3.2 Lift-off Oxide

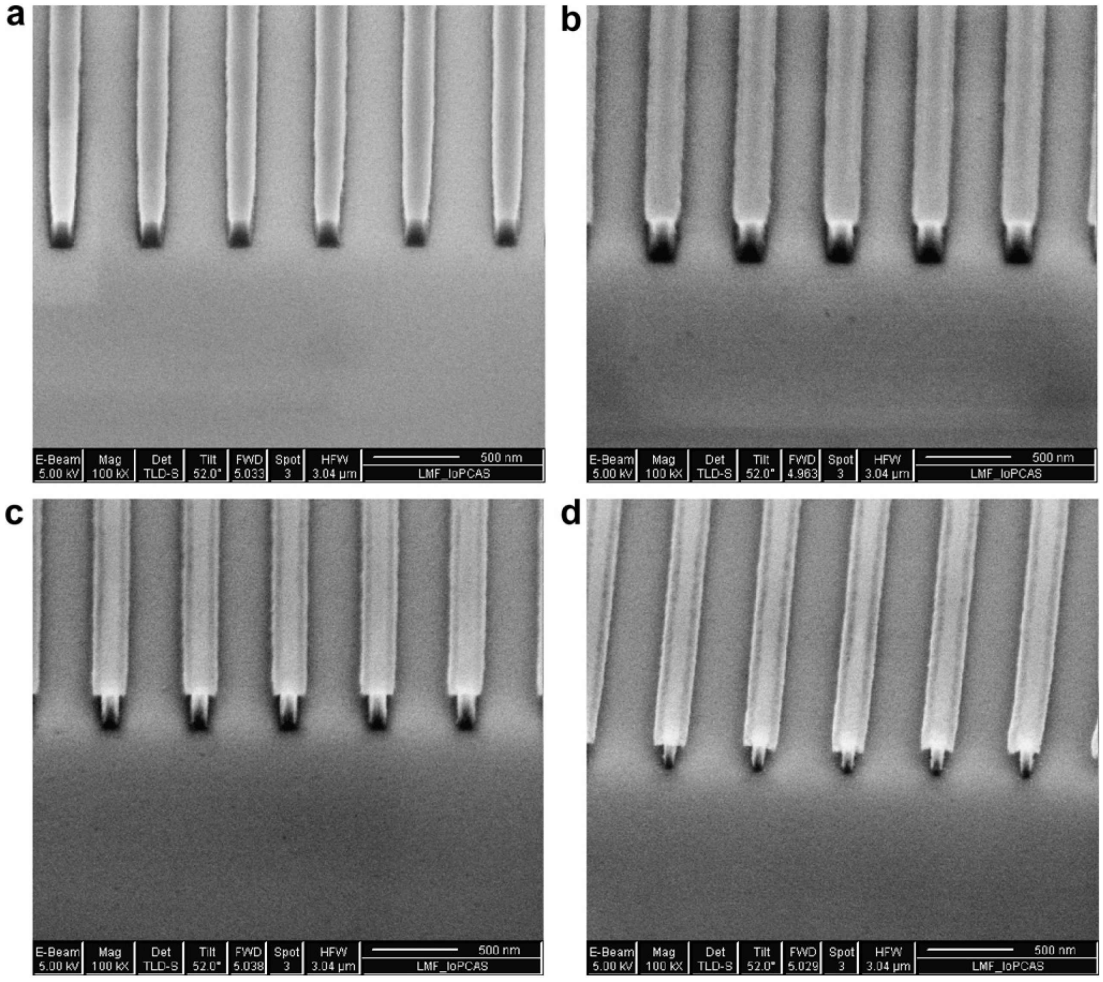

Figure 4.11: HSQ (50nm)/PMMA(200nm) bilayer structure with over oxygen plasma etching. (a, b, c, d) are with various oxygen plasma cleaning time. The longer over O_2 plasma etching time gives sharper under-cut profile in the HSQ/PMMA bilayer. (From Ref.[91])

To have clear and high lift-off yield, a good under-cut E-beam resist profile is necessary, especially for our nanomask lift-off process, which serves as ion-milling mask and lift-off mask at the same time. Since the nature of HSQ (ba-

sically SiO_2) and PMMA (transparent plastic) is chemically different, HSQ is a perfect oxygen plasma etching mask for PMMA. PMMA can be removed clearly with oxygen plasma. Figure 4.11 show the under-cut profile in HSQ/PMMA bi-layer can be modulated by oxygen plasma over etching time.

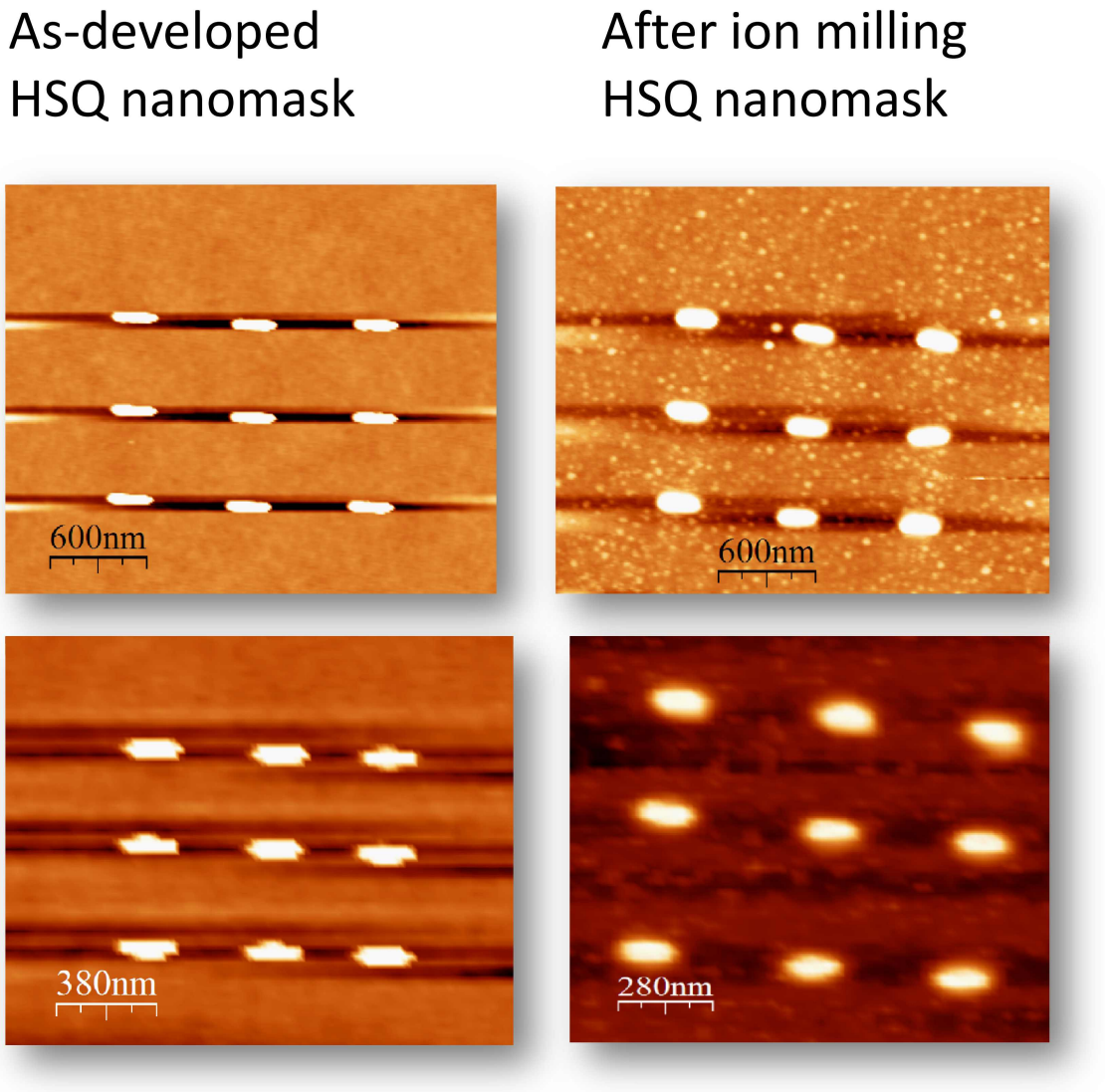

Figure 4.12: AFM images of HSQ/PMMA lift-off nanomask before and after ion-milling. Ion-milling angle is 5^o. AFM images exhibit reduced aspect-ratio after ion-milling

There are several choices for growing protecting oxide for the nanopillar. Here, we choose to use evaporated silicon oxide instead of PECVD or sputtering silicon oxide. Due to low pressure and large mean free path of gas in the e-beam evaporating process, evaporated SiO_2 does not coat the sidewall well, plus the shadowing effect of the under-cut profile of HSQ/PMMA nanomask. Evaporated SiO_2 is the oxide to provide enough sidewall isolation without increasing the difficulties of lift-off. PECVD or sputtering oxide could coat the sidewall thoroughly and therefore, is very difficult for lift-off process. In that situation, growing oxide for the lift-off nanopillar process is rather complicated. To make the lift-off process work, we need to grow oxide thick enough to protect nanopillars from ambient atmosphere. At the same time, we need the oxide thin enough for high-yield lift-off process. A typical suggestion is the oxide need to be three time thick than the nanopillar. To have high lift-off yield, the nanomask also needs to be at least three time thicker than the lift-off materials.

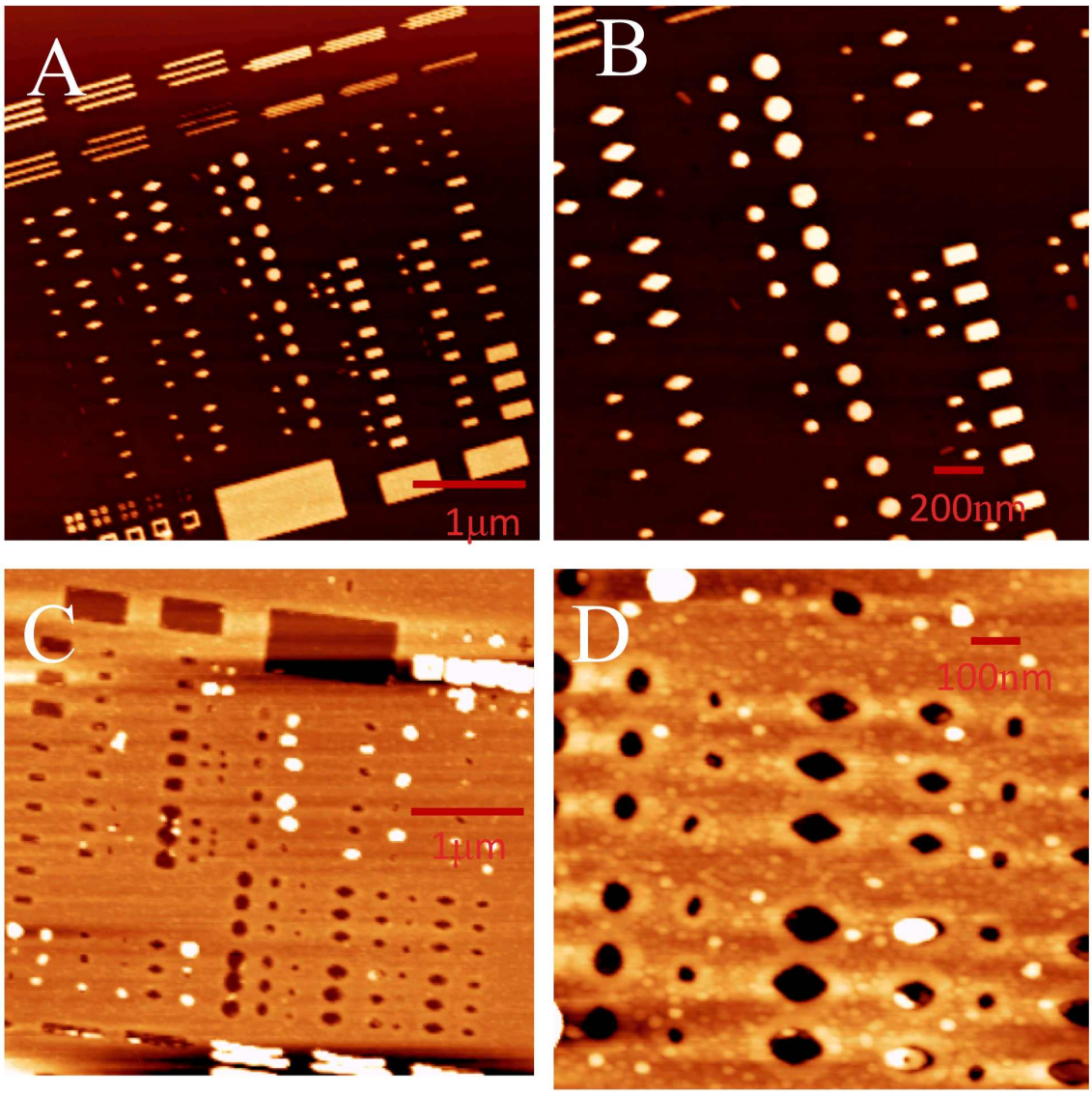

Figure 4.13: AFM images of HSQ/PMMA lift-off nanomasks and the image after lifting off 40nm evaporated SiO_2. (A, B) are AFM images of HSQ/PMMA nanomask. Various shapes, such as rectangles, circles, and diamonds can be seen clearly. (C, D) are AFM images after lifting off 40nm SiO_2. The shape geometry is still maintained after ion-milling and lift-off. Theses figures show that the doses affect the lift-off yield.

Fig.4.13 shows AFM images of the HSQ nanomask before lifting off and after lifting off a 40nm SiO_2 thin films. In the Fig.4.13(a)(b), HSQ nanomasks can be

made into rectangle, circle, and diamond shapes very accurately until the size approaching 50nm or smaller. All of the shapes look all the same and lose its features. However, interestingly, E-beam exposure dose affects the lift-off yield more than the size of CAD. In the Fig.4.13(C)(D), the dose is higher in those devices close to the bottom of the images. We could see low-dose devices do not fully lift-off, but higher dose devices do regardless if its size is smaller. This result suggest that thick PMMA may play a role in the lift-off process in our recipe. We know IPA alone can develop (or remove) E-beam exposed PMMA and we also sonicate the wafers in IPA for 30min that may help lift-off yield as well.

Process	Details and parameters
Ion milling (Defining nanopillars)	Ion-milling parameter in INTELVAC: 150V, 150V, 35mA, angle 3°. 30sec shutter cycle duty is necessary for high lift-off yield. Stop the milling in the middle of tunnel barrier to avoid any redeposition.
Evaporate SiO_2	Deposit evaporated SiO_2 for desirable thickness in the EVEN hour evaporator at 1nm/sec. 3 times the nanopillar height is enough for protecting nanopillars. Thicker oxide lower the lift-off yield. Typically, we use 40nm SiO_2
Lift-off oxide	Soak at Remover PG hot bath at 75^oC for 30min. Sonicate the same hot bath for 30min. Soak in IPA and sonicate for 30min. Check lift-off results with optical microscope. Repeat the process if lift-off fail.

Table 4.2: Ion milling, oxide grow and lift-off procedure

The ~100nm holes left on the top of nanopillars are capable of persisting through the conventional photolithography processes before putting down the top leads. To enhance the device yield, light oxygen plasma clean, ion-milling or RF back-sputtering are recommended before putting down the top leads. In addition, once the nanopillars are fabricated and are protected with oxide. The nanopillars can be robust enough sustaining air-annealing without changing in the TMR. To achieve this, the materials of top leads are required to be inert. We have been using Ta 50nm/Ru 20nm for our leads and this choice are robust enough for air-annealing.

4.4 Summary of HSQ tri-layer nanomask process

Fabricating a two-terminal ~100nm nanopillar is a difficult and sensitive process. Through last few year helping other working on the nanopillar lift-off process, I realized it required patience and attention to the details of fabrication process. Usually, the performances of tools are very stable and repeatable. Most mistakes are from human operation and ignorance of the sensitivity of nanofabrication processes.

The following table summarizes the process of HSQ/PMMA nanopillar lift-off process.

Process	Step details
Spin coat e-beam resist	spin coat omnicoat at 1700 rpm and bake at 180^{o}C for 1min twice. Spin coat PMMA at 4000rpm for 1min and bake 170^{o}C for 1min. Spin coat HSQ 6% at 4000rpm for 1min and bake at 170^{o}C for 1min.
E-beam exposure	JEOL9300 e-beam exposure. For 9×9 dies for 3" wafers, it takes about 40minutes
Develop e-beam resist	Develop wafers in 726MIF for 2minutes. You will see most HSQ resist become white and washed away.
Inspection	Use optical microscope under dark field mode to inspect if the exposure is successful.
Transfer pattern to PMMA	Oxygen plasma in Oxford 80 under 50mmTorr, 20sccm and 100W for around 1min20s.
Ion milling to define nanopillars	Use INTELVEC ion milling with SIMS. Use 30/30sec shutter cycle to avoid over heating. (Also referred to Table 4.2)
Isolate and protect nanopillar	Evaporated 40nm SiO_2 in EVEN HOUR evaporated. The deposition rate need to be $\approx$ 1nm/sec. If evaporating too fast or too slow, the oxide layer could be easily peel-off.
Lift off with Remover PG	30min in Remover PG at 75^oC for 30min. Sonicate with the same hot Remover PG for another 30min. Use optical microscope to check the dot array if lift-off is successful or not. If not, sonicate for another 30min to 1 hour.

Table 4.3: Summary of the HSQ/PMMA/Omnicoat lift-off process. (Continued in the next page on Table 4.4)

Process	Step details
Define bottom lead	Photolithography and ion milling to define bottom lead. Lift off PR.
Protect short	Photolithorgraphy and evaporated at least 3 times the bottom lead height. I have been using at least 150nm SiO_2. Deposition rate for CNF EVEN hour evaporator needs to be 0.1nm/sec for a good oxide layer
Sputter top leads	Photolitography for top leads. Oxygen plasma descum before top leads sputtering. Sputter Ta 50nm / 20nm Ru. Lift off PR.

Table 4.4: Summarie the HSQ/PMMA/Omnicoat lift-off process (continued Table 4.3)

CHAPTER 5

SPIN-TORQUE EFFECT IN ASYMMETRIC MAGNETIC TUNNEL JUNCTIONS

5.1 Motivation

Engineering spin-transfer switching has been an important topic for its potential applications for non-volatile magnetic memory. Many efforts focus on engineering the magnetic properties or configuration in order to lower the critical switching current density, such as tapered structures[6], perpendicular structures[46], hybrid of in-plane and out-of-plane polarizers[41], double fixed layers[25], and non-uniform current injection through holes in the spacer layer[59]. These approaches have demonstrated promising results in reducing the critical current one or two orders of magnitude.

In magnetic tunnel junctions (MTJs), electronic structures, however, a play significant role in the spin-torque effect. Recently, experiments[58, 50, 15] and theories[32, 80, 81, 47, 36] have shown that asymmetric electrodes in MTJs can change the spin-torque vectors and even affect spin-torque switching. Asymmetric electrodes[58] affect the switching behavior significantly, even inducing back-hopping switching, suggesting that the perpendicular torque could be as strong as coercive field and induce switching. More recently, Chanthbouala *et al.* [15] showed that out-of-plane torque (field-like torque) plays a major role in the domain-wall (DW) motion in the CoFeB/MgO/CoFeB/NiFe MTJ. The ST-FMR measurement exhibits a strong anti-symmetric Lorentzian ST-FMR signal at zero bias which indicates non-zero field-like torkance. This would induce highly asymmetric field-like torque under high voltage bias [50]. These

results suggest that spin-torque switching behavior can be affected not only by the magnetic properties of ferromagnetic materials (such as the out-of-plane polarizer, saturation magnetization M_s and magnetic anisotropy K_u), but also the electronic properties of the electrodes (the band structure and density of state).

Another motivation for this study is to understand the fundamental spin-dependent transport and the interaction between the spin-polarized current and the ferromagnetic materials in the MTJ. One of the reasons why the spin-dependent magneto-transport is not very well-understood is because of the limitation of measurable physical quantities. For example, the explanation of TMR voltage bias dependence still does not constitute consensus in the society. One model is based on the Slonczewski-type simple parabolic band model. Another explanation is based on the magnon-scattering process. Both explanations could show reasonable accuracy to explain the TMR bias voltage dependence. It is, however, still not clear which mechanisms dominate the whole process. Because of newly discovered spin-transfer torque vector measurement, we could directly probe the spin-polarized channels in the MTJ. Slonczewski *et al.*[75] calculated that spin-transfer torkance (the derivative of spin-torque vector with respect to voltage) can be expressed as $d\mathbf{T}_{\parallel,R}/dV = \hbar/4e(G_{++} - G_{--} + G_{+-} - G_{-+})\mathbf{S_R} \times (\mathbf{S_R} \times \mathbf{S_L})$. Through measuring spin-transfer torkance, we could acquire the extra information regarding the spin-polarized current channels. This measurement technique we could further comprehend the spin-dependent interaction in the MTJ structure.

In this chapter, I will first present the results of scanning transmission electron microscopy (STEM) with aberration correction on asymmetric FeCoB / MgO / FeNiB and symmetric FeCoB / MgO / FeCoB MTJs. ("Asymmetric"

MTJ refer to the top and bottom electrodes consisted of different ferromagnetic materials next the tunnel barrier.) In addition, we study tunneling conductance as a function of voltage (dI/dV-V) and TMR voltage bias dependence (TMR-V) behaviors in the symmetric FeCoB / MgO / FeCoB and asymmetric FeCoB / MgO / FeNiB MTJs and discuss how these results inspired me to the next step of FeCoB/MgO/FeB MgO-based MTJ. In the second part of this chapter, I will present the results of FeCoB / MgO / FeB and FeB / MgO / FeCoB MTJ and discuss how density of states of ferromagnetic electrodes affects the transport behaviors we observed in the tunneling conductance dI/dV-V and TMR voltage bias dependence TMR-V measurement. Furthermore, I will present the spin-torque effect in the asymmetric MgO-based MTJs and explain the spin-torque vector in terms of the electronic and the band structure of ferromagnetic materials.

5.2 Asymmetric $Fe_{60}Co_{20}B_{20}$/MgO/FeNiB MTJs

Reducing critical switching current densities is an important research topic, because further lowering power consumption for memory application is essential for mobile electronics. One way to lower the critical current of spin-torque switching is to use low saturation magnetization M_s ferromagnetic materials for the free layer electrode. Based on the LLG equation with the spin-torque term[74, 77] in the spin-valve nanopillar, the critical current is

$$I_c^{\pm} = \frac{\alpha}{\theta^{\pm}} \frac{2e}{\hbar} M_s V [H_{eff} + 2\pi M_{eff}] \tag{5.1}$$

Where $I_c^{\pm}$ is the critical switching current of positive and negative current polarities for the free layer, α is the Gilbert damping constant, $\theta^{\pm}$ is the spin torque

efficiency parameter, e is the electron charge, M_s is the saturation magnetization of the free layer, and $4\pi M_{eff}$ is the effective demagnetization field.

Based on Eqn. 5.1, the critical switching current is proportional to the square of the saturation magnetization of the free layer electrode $I_C \sim M_S^2 V\alpha$. To effectively reduce the critical current is to lower the M_s. Braganca *et al.*[5] showed that using Py/Cu/Py ($M_S = 880 emu/cm^3$ for Py) could effectively reduce I_c when comparing to using Co/Cu/Co ($M_S = 1400 emu/cm^3$ for Co) as the free layer [33]. Spin-torque switching in MTJs was first demonstrated around 2004 [24, 30]. Those experiments used CoFe-based MTJs. The saturation magnetization for CoFe is $1180 emu/cm^3$. The critical switching current $J_c = 0.5 \times 10^7 A/cm^2$[24]. A reasonable next step to reduce the critical current in MTJs, therefore, is to replace CoFe-based alloy to low saturation magnetization materials M_s (such as Py) as has been done in the spin valve spin-torque switching. Read *et al.*[66] has shown that NiFeB could possibly match with MgO and form high TMR (>100%) MgO MTJs. Since then, I have worked on fabricating $Fe_{60}Co_{20}B_{20}$/MgO/FeNiB MTJs into nanopillar devices and studied the spin-torque effect in the $Fe_{60}Co_{20}B_{20}$/MgO/FeNiB.

Note that due to the mistake of the $Py_{80}B_{20}$ sputtering target supplier, the first $Py_{80}B_{20}$ target we ordered is not $Py_{80}B_{20}$, which is $(Ni_{80}Fe_{20})_{80}B_{20}$, but $(Ni_{20}Fe_{80})_{80}B_{20}$. The wrong target is confirmed by using the scanning transmission electron microscopy (STEM) studies by Pinshane Huang. I have also further performed SIMS and XPS studies on the $Py_{80}B_{20}$ and obtain the same result as Pinshane. The FCB-$Py_{80}B_{20}$ TMR results showed in figure 5.1 (d) from Ref. [66] should be corrected to $(Ni_{20}Fe_{80})_{80}B_{20}$. In addition, I used FeNiB for the abbreviation of $(Ni_{20}Fe_{80})_{80}B_{20}$.

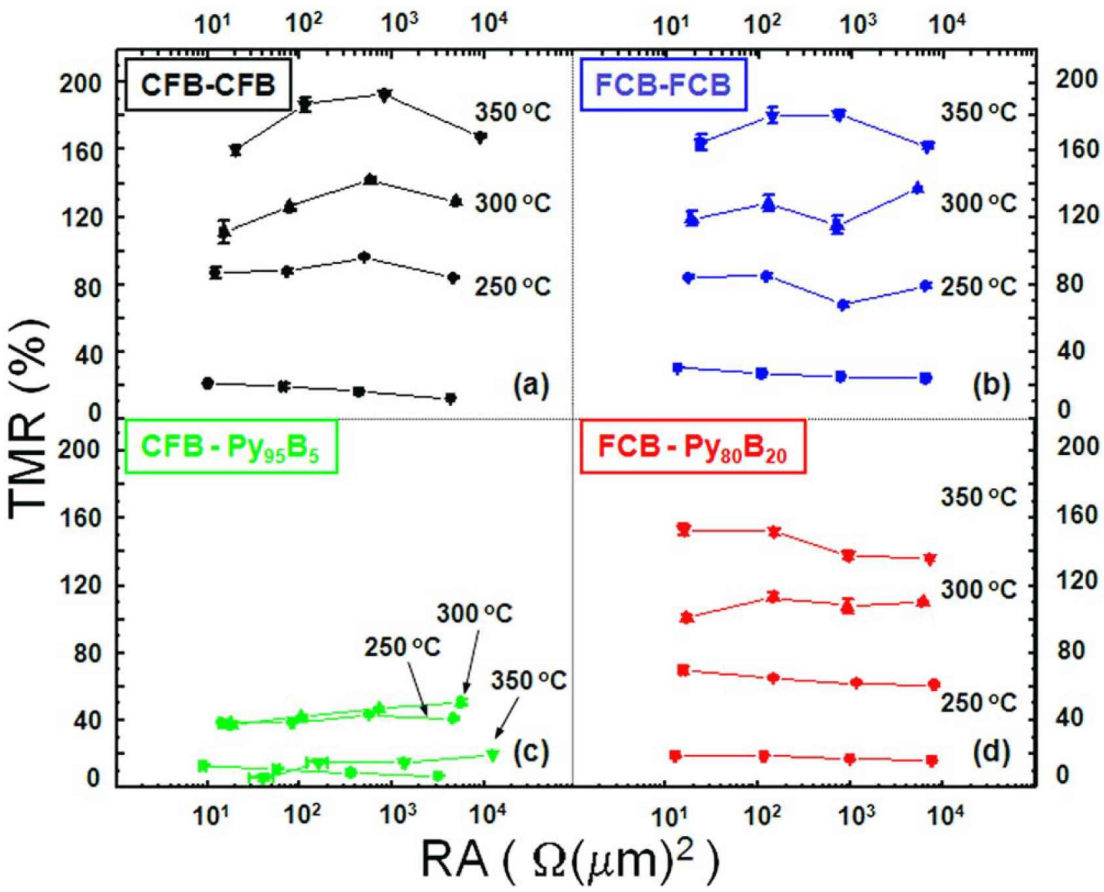

Figure 5.1: TMR vs RA-product plots under various annealing temperatures with various electrode materials FCB=$(Co_{20}Fe_{80})B_{20}$, CFB=$(Co_{80}Fe_{20})B_{20}$, $Py_{80}B_{20}$ and $Py_{95}B_5$ in MgO-based MTJs. (a) IrMn / CFB / MgO / CFB annealed at 250°*C*, 300°*C* and 350°*C* Similarly, (b) IrMn/FCB/MgO/FCB, (c) IrMn/CFB/MgO/$Py_{95}B_5$. (d) IrMn/FCB/MgO/$Py_{80}B_{20}$. Note that due to the mistake of the $Py_{80}B_{20}$ sputtering target supplier, the $Py_{80}B_{20}$ target we used in this experiment is not $Py_{80}B_{20}$, but $(Ni_{20}Fe_{80})_{80}B_{20}$. In the following chapter, I will use FeNiB to represent Fe-rich $(Ni_{20}Fe_{80})_{80}B_{20}$.

5.2.1 Sample Geometry and Measurement

The multilayer stacks are [Ta 5 / CuN_x 20 / Ta 2]$_4$ / IrMn 15 / FeCoB 4 / MgO 1.1 / FeNiB 3/Ta 8 / Ru 7 (in nm) and [Ta 5 / CuN_x 20 / Ta 2]$_4$ / IrMn 15 / FeCoB 4 / MgO 1.1 / FeCoB 3 /Ta 8 / Ru 7. The composition of FeCoB is $Fe_{60}Co_{20}B_{20}$. FeNiB here is sputtered from a FeNiB target. From STEM-EELS analysis by Pinshane, the composition of the FeNiB ferromagnetic layer layer electrode is close to $Fe_{64}Ni_{16}B_{20}$. Those magnetic multilayer stacks used in this thesis are grown in the AJA sputtering system with DC and RF sputtering. The devices used for spin-transfer effect studies are fabricated with E-beam, photolithography and ion-milling into $\sim$ 150nm $\times$ 250nm nanopillar structures for spin-torque study.

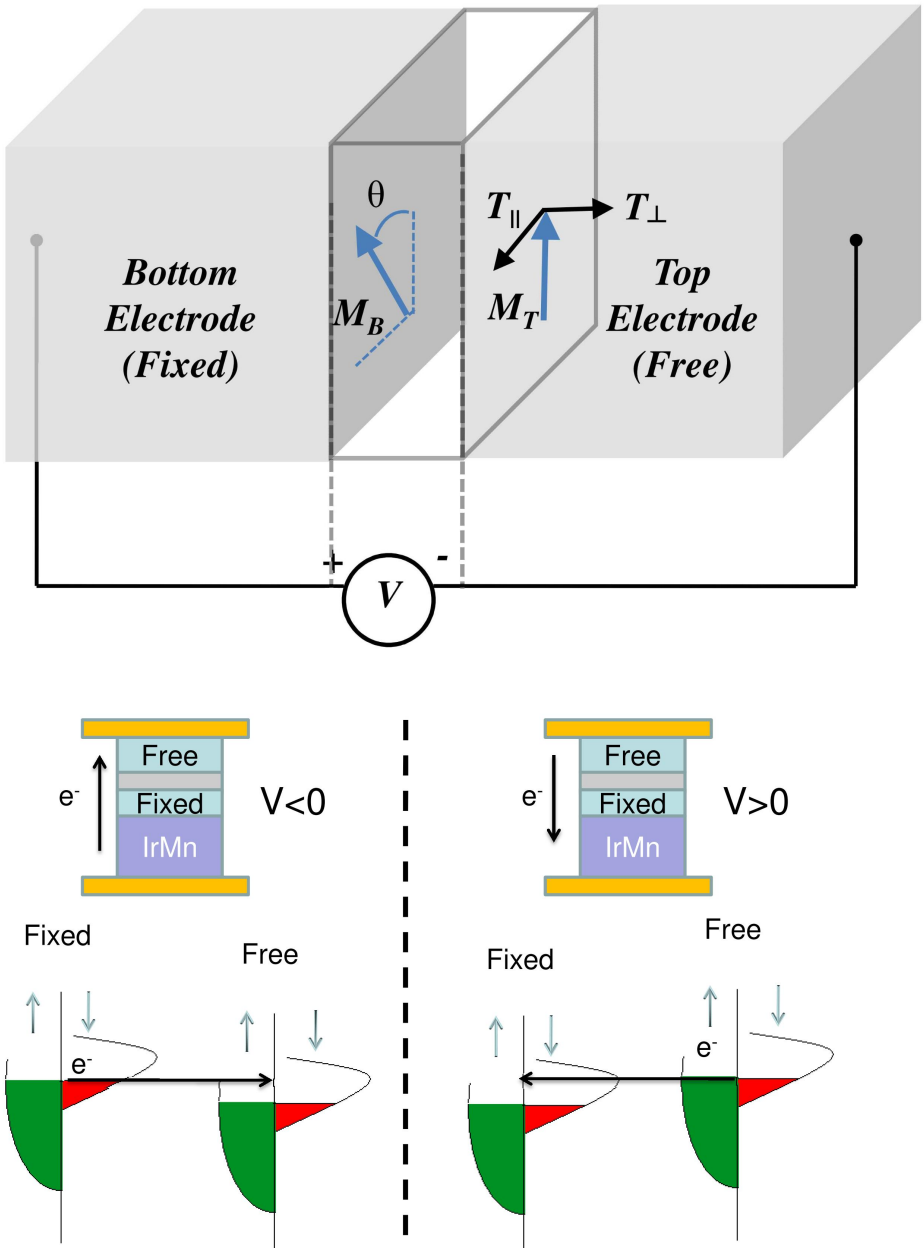

Figure 5.2: This figure illustrates the definition of voltage polarity, ferromagnetic band structures, and the device structure. With positive voltages V>0, electron currents flow from top electrodes (free layers) to bottom electrodes (fixed layers). With negative voltage (V<0), electron current flows from the bottom electrode to top electrodes.

The voltage polarities convention I use throughout my thesis is consistent

with typical spin-torque measurement in our group spin-valve spin-torque results. Electron currents flow from free layer (top) to fixed layer (bottom) with positive voltages. With negative voltages, electron currents flow from fixed layer to free layer regardless of electrode materials. Figure 5.2 further illustrate the definition of sign convention. Both dI/dV-V and TMR voltage bias dependence measurements are performed with the 4-wire measurement to eliminate the voltage drop from the resistance of contact leads to obtain the maximum TMR and accurate bias voltage in dI/dV across the junctions. The equipment used to measure currents and voltages is the Keithley 2600 source meter. The dI/dV measurement is acquired by measuring the I-V curve and perform numerical derivative calculation to obtain the differential tunneling conductance dI/dV. The TMR-V measurement is performed with DC bias voltage constantly applied to devices with external magnetic field sweeps to acquire the resistance of parallel and anti-parallel states.

5.2.2 MgO-based MTJs Material Characterization

The material characterization technique I use here to check the MTJs is based on both secondary ion mass spectrometry (SIMS) and scanning transmission electron microscopy (STEM) with aberration-correction. STEM with aberration-correction enabling us to probe the chemical composition at the atomistic scale through electron energy loss spectroscopy (EELS). Previous studies[66, 13] based on the atomic-scale spectroscopic imaging have reveal the details of the CoFeB/MgO interfaces. The CoFeB / MgO / CoFeB MTJ structures actually form a thin layer of Mg-B-O layer which consisted of $Mg_2B_2O_5$ and $Mg_3B_2O_6$ compounds from MgO and B_2O_3. In addition the CoFeB electrodes actually con-

verted into polycrystalized CoFe, since the B, a glass forming materials, diffuse out of the electrodes after 350°C annealing process. In addition, the existence of B also help reduce both the cobalt oxide and iron oxide at the CoFeB/MgO interfaces in the MTJ[67]. The phenomena help to promote CoFe/MgO interface, instead of CoFe/FeO_x/MgO.

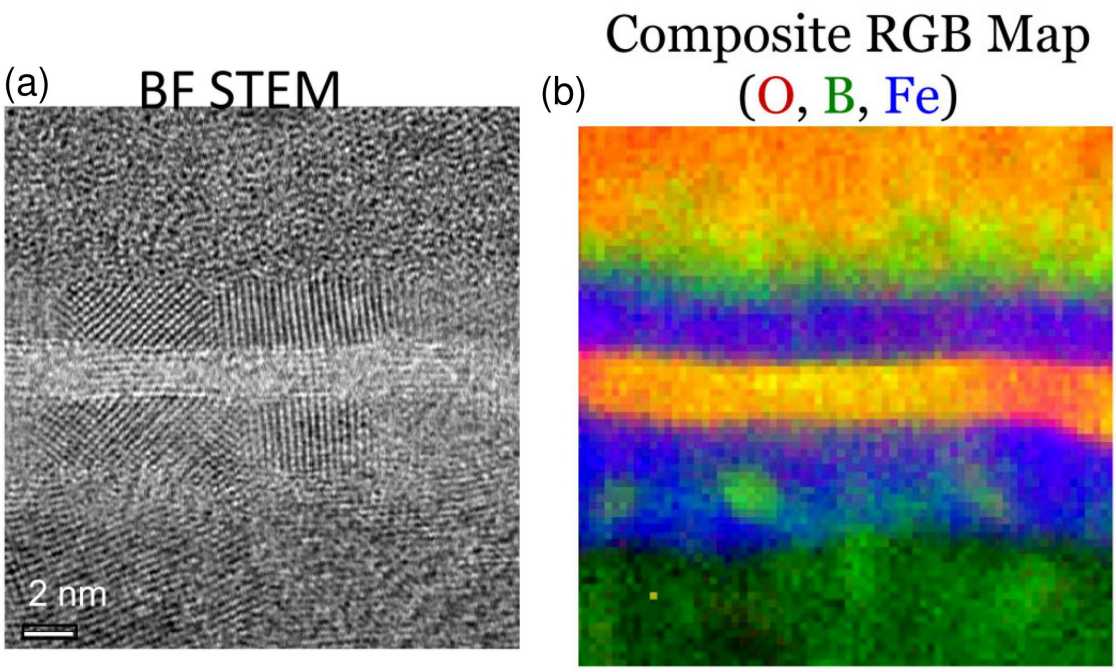

Figure 5.3: Bright-field STEM image (a) and STEM EELS chemical map (b) for $Fe_{60}Co_{20}B_{20}$ / MgO / $Fe_{60}Co_{20}B_{20}$ electrodes. Non-uniformity of bottom ferromagnetic electrode appears in the thick $Fe_{60}Co_{20}B_{20}$ fixed layer. CoFeB composition is $(Co_{20}Fe_{80})B_{20}$ In addition, B diffuses out of amorphous electrodes and segregates in the fixed layer. (Data from Pinshane Huang).

Figure 5.3 shows atomic-scale spectroscopic image (SI) results form STEM-EELS results of IrMn/$Fe_{60}Co_{20}B_{20}$ /MgO /$Fe_{60}Co_{20}B_{20}$. These results are derived from a collaboration with Pinshane Huang a graduate student working with Prof. David Muller. Figure 5.3 (a) is the bright field STEM images. The

$Fe_{60}Co_{20}B_{20}$/ MgO/ $Fe_{60}Co_{20}B_{20}$ multi-layer thin films are grown in AJA by DC and RF sputtering. We fabricated the same layer stack in both micro and nano MTJs. The TMR performance for CoFeB-based MgO MTJs is ~100%. We observed that both the CoFeB electrodes and the MgO tunnel barrier exhibit polycrystalline structures after annealing at 350°C. Note that in figure 5.3 (b) the thick fixed FeCoB layer exhibits non-uniformity primarily in the annealed films, but the thin free FeCoB layer appears to be more uniform. This non-uniformity has a significant amount of B located in those spots. Overall, B leaves FeCoB electrodes diffusing into both MgO and Ta layers and makes FeCo layer polycrystallize.

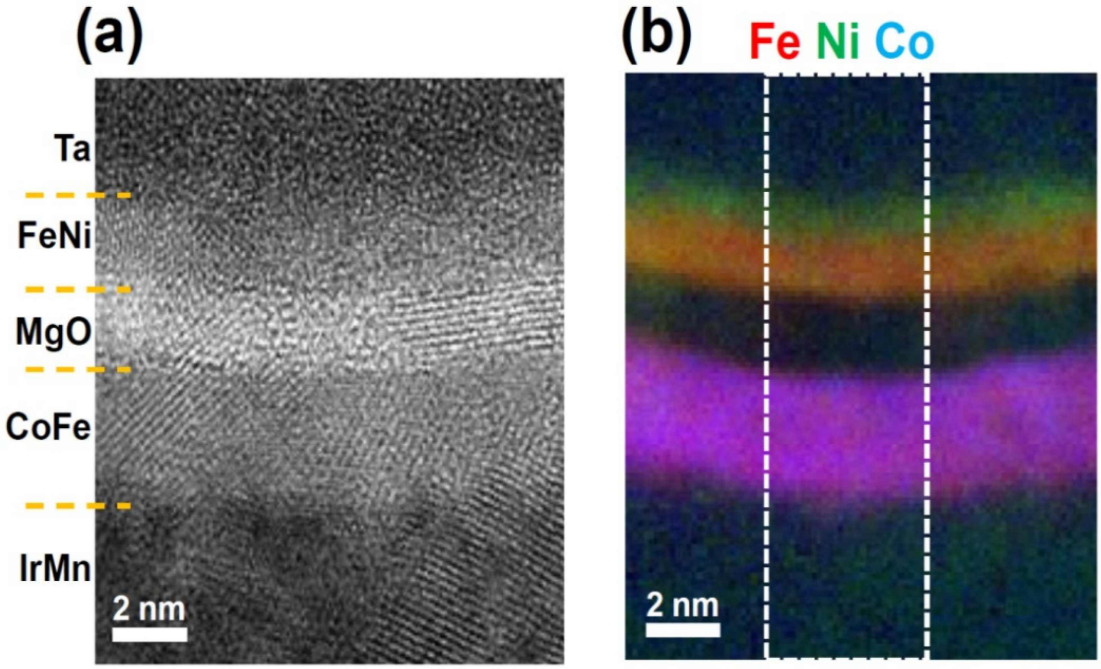

Figure 5.4: STEM EELS chemical map for CoFeB/MgO/FeNiB electrodes. (a) Bright-TEM images of asymmetric CoFe/MgO/FeNi electrodes. Polycrystalline structure can be observed. (b) EELS-chemical map image. Fe and Ni appear phase segregation in the free layers. (Data from Pinshane Huang)

Figure 5.4 consists of the atomic-scale spectroscopic imaging of IrMn / $Fe_{60}Co_{20}B_{20}$ / MgO / FeNiB MTJs. Clear polycrystallized thin films are observed. The grain size is estimated to be around 5 to 10nm. Atomic-scale chemical map exhibits Fe and Ni segregations in the free layer. The CoFeB fixed appear to be very uniform in the image. The same magnetic multilayer stack is fabricated into the nanopillar structure. The spin-torque effect in the asymmetric electrode MTJs appear to be exotic. The details of the spin-torque is covered in the latter section. The CoFeB fixed layer does not exhibit uniformity spots which appear in the IrMn/$Co_{40}Fe_{40}B_{20}$/MgO/$Co_{20}Fe_{20}B_{20}$ MTJ.

5.2.3 Magnetotransport and Spin-torque Effect in the FeCoB/MgO/FeCoB and FeCoB/MgO/FeNiB MTJs

In this section, I will present the tunneling conductance (dI/dV-V), TMR voltage bias dependence (TMR-V) and spin-torque switching effect of both symmetric IrMn / $Co_{40}Fe_{40}B_{20}$ / MgO / $Co_{40}Fe_{40}B_{20}$ and asymmetric MgO-based MTJs.

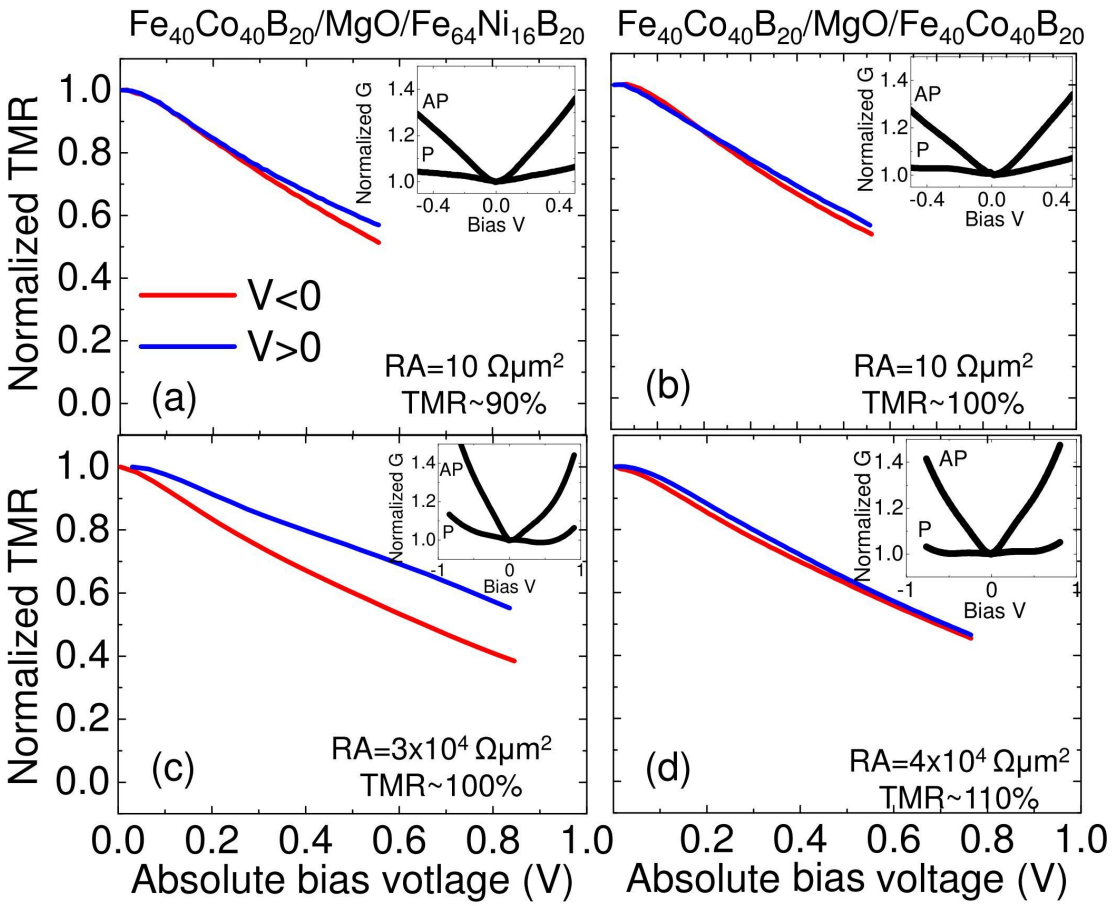

Figure 5.5: Normalized TMR bias dependence and tunneling conductance dI/dV (the insets) with respect to the bias voltages in (a, b) nanopillar devices and (c, d) microjunction devices. In asymmetric $Fe_{40}Co_{40}B_{20}/MgO/Fe_{64}Ni_{16}B_{20}$ device, the asymmetry in the TMR bias dependence is more stronger than symmetric $Fe_{40}Co_{40}B_{20}/MgO/Fe_{40}Co_{40}B_{20}$ device.

Figure 5.5 shows the TMR bias dependence of both symmetric $Fe_{40}Co_{40}B_{20}$ / MgO / $Fe_{40}Co_{40}B_{20}$ and asymmetric $Fe_{40}Co_{40}B_{20}$ / MgO / FeNiB MTJs. First, we notice in the asymmetric FeCoB/MgO/FeNiB MTJs, the strong asymmetry in both differential tunneling conductance dI/dV-V and TMR voltage bias dependence TMR-V. Strong asymmetry in the TMR bias dependence is also ob-

served in both low RA and high RA $Fe_{40}Co_{40}B_{20}$ / MgO / $Fe_{61}Ni_{16}B_{20}$ MTJs. Symmetric $Fe_{40}Co_{40}B_{20}$ / MgO / $Fe_{40}Co_{40}B_{20}$ MTJs, however, exhibit symmetric TMR bias dependence in both RA devices. The TMR decrease rate for positive voltages is 59%/V and for negative voltages is 81%/V in asymmetric FeCoB/MgO/FeNiB high RA MTJs (figure 5.5(c)). The TMR decrease rate in symmetric FeCoB/MgO/FeCoB is ~71%/V and is fairly close for both polarities compared to asymmetric MTJs. The majority decrease of TMR with respect to voltages can be explained based on magnon excitation[54, 55]. The small asymmetry of TMR due to voltage bias polarities is not very well understood. Possible explanations will be discussed in the later section.

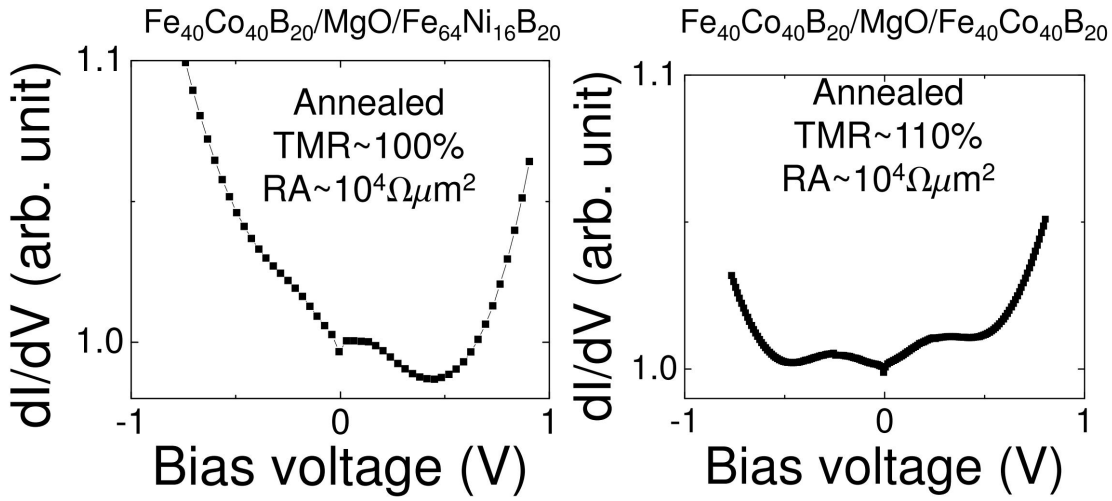

Figure 5.6: Differential conductance dI/dV-V of (a) FeCoB/MgO/FeNiB and (b) FeCoB/MgO/FeCoB. Oscillation in the dI/dVI within low bias $\pm 0.6V$.

Figure 5.6 shows the differential conductance of both symmetric and asymmetric MTJs. Note that around low voltage regimes ($\leq \pm|0.6V|$) there are oscillations of dI/dV-V. There are local minimums (dips) and local maximums (shoulders) in the annealed high TMR MgO MTJs. Those oscillations do not appear

in the as-grown MgO MTJs. Two shoulders appear in figure 5.6 at ±0.25V and dips appear at ±0.5V.

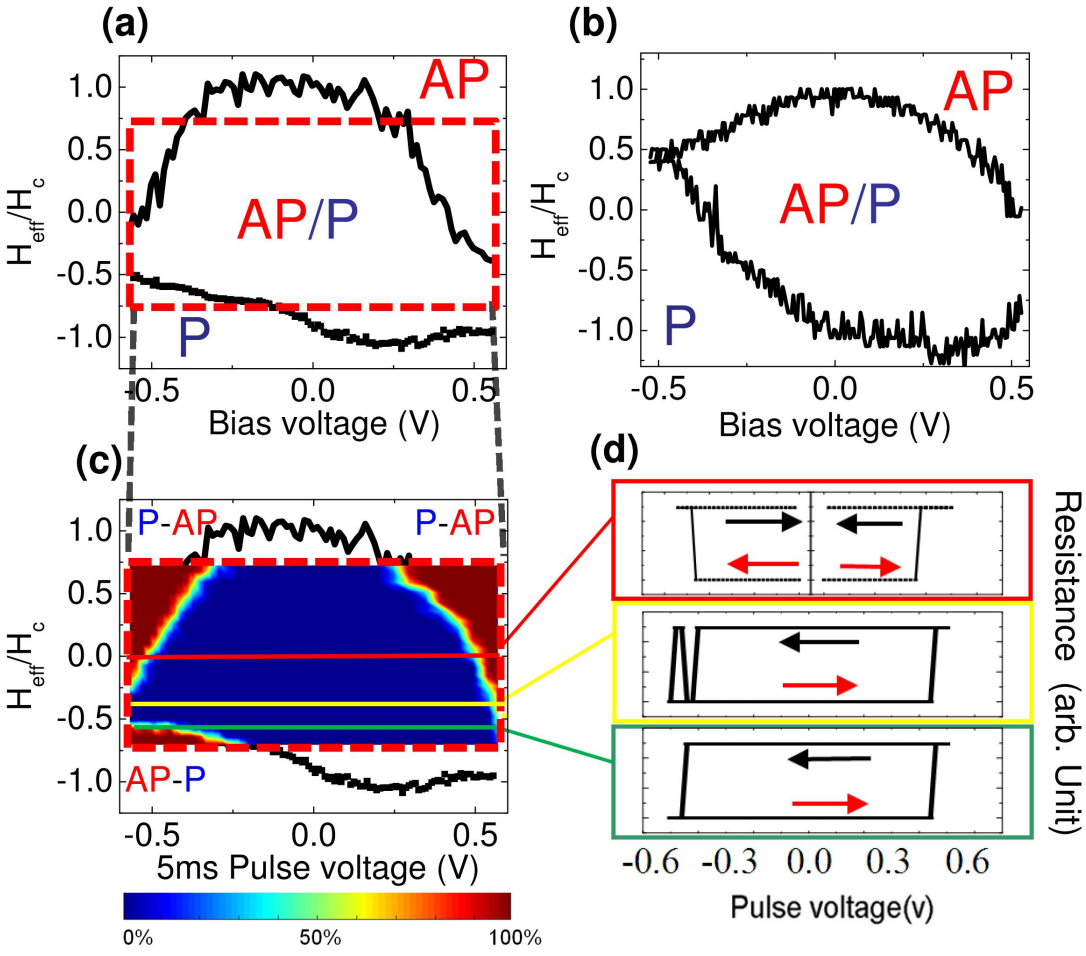

Figure 5.7: Swithing phase diagrams of IrMn/CoFeB/MgO/CoFeB and and IrMn/CoFeB/MgO/FeNiB. (a, b) are the switching phase diagrams of FeCoB/MgO/FeNiB and FeCoB/MgO/FeCoB. The color contour plot of the switching probabilities of FeCoB/MgO/FeNiB overlap with (a). (d) are the pulse voltage switching behavior under various pulse voltages.

Since we are interested in the spin-torque effect in the high TMR FeCoB/MgO/FeNiB MTJ nanopillars. We quickly exam the spin-torque effect through

measuring the switching phase diagram. As seen in Figure 5.7, the switching results are more complicated than we expected. To describe and understand the switching behavior of $Fe_{40}Co_{40}B_{20}$ / MgO / FeNiB, I have adopted the concept of switching phase diagram (SPD), which simply measures the switching events under various voltages and fields and plots the data in a contour plot. The approach enable using 2D contour plot to fully represent the switching behavior. In the asymmetric MTJ $Fe_{40}Co_{40}B_{20}$ / MgO / FeNiB, finding a field regime capable of performing bipolar switching was difficult when we first attempted the current switching experiments. We could only observe bipolar switching within a small field regime $Fe_{40}Co_{40}B_{20}$ / MgO / FeNiB samples.

To conclude the $Fe_{40}Co_{40}B_{20}$ / MgO / FeNiB studies, in the initial studies of asymmetric $Fe_{40}Co_{40}B_{20}$ / MgO / FeNiB MTJs, FeNiB after annealing exhibits phase segregation in Fe and Ni, therefore, is not an ideal control experiment for understanding how electrode chemical composition affecting switching behaviors. This result does encourage me further explore the spin-torque effect in the asymmetric system. To fully comprehend how electrode materials in the MTJ affecting switching, we change electrode materials to simple element FeB and alloy FeCoB. Since B leaves electrodes after annealing and provide high TMR MgO MTJs, we consider $Fe_{80}B_{20}$ and $Fe_{40}Co_{40}B_{20}$ as simple Fe and $Fe_{50}Co_{50}$ after annealing. The measurement results of $Fe_{80}B_{20}$ and $Fe_{40}Co_{40}B_{20}$ is presented in the later section.

5.3 Asymmetric FeCoB/MgO/FeB MTJs

Previous studies based on the FeCoB/MgO/FeNiB asymmetric MTJ suggest that asymmetric electrodes could affect switching significantly and induce unreliable switching events. At the same time, Oh *et al.*[58]reported using $Co_{20}Fe_{60}B_{20}$ and $Co_{49}Fe_{21}B_{30}$ as free layers with $Co_{40}Fe_{40}B_{20}$ as the fixed layer exhibiting back-hopping at low voltages. We made a similar observation in our studies of FeCoB/MgO/FeNiB. These results suggested that not only are the magnetic properties parameters which affect switching, but also, the electronic structures in the MTJ have an impact on spin-torque switching.

To understand how electronic structures in the MTJ affect spin-torque behaviors, I first carefully examined the electronic transport in the asymmetric MTJs through measuring the differential conductance v.s. bias voltages dI/dV-V, TMR voltage bias dependence, the spin-torque-driven switching phase and spin-torque ferromagnetic resonance measurement (ST-FMR)

The asymmetric MTJs structure I used here are Ta 5nm/Ru 20nm/Ta 5nm/IrMn 10nm/FeCoB 4nm/MgO/FeB 2nm/Ta 3nm/Ru 4nm and Ta 5nm/Ru 20nm/Ta 5nm/IrMn 10nm/FeB 4nm/MgO/FeCoB 2nm/Ta 3nm/Ru 4nm. The composition of FeCoB is $Fe_{40}Co_{40}B_{20}$ and FeB is $Fe_{80}B_{20}$. The magnetic multilayer stacks are sputtered in AJA system using DC and RF sputtering. The nanopillar devices are fabricated using conventional photolithograph, E-beam lithography and ion-milling.

5.3.1 Results of Tunneling Conductance dI/dV-V in Asymmetric $Fe_{40}Co_{40}B_{20}$ / MgO / $Fe_{80}B_{20}$ MTJs

To understand the basic transport properties of MTJs, we measure the tunneling conductance versus bias voltage by applying external fields to set the initial state either in the parallel (P) or antiparallel (AP) states. We measure the tunneling currents at various bias voltages. Then, we take the I-V curve to obtain the numerical calculated dI/dV-V curve.

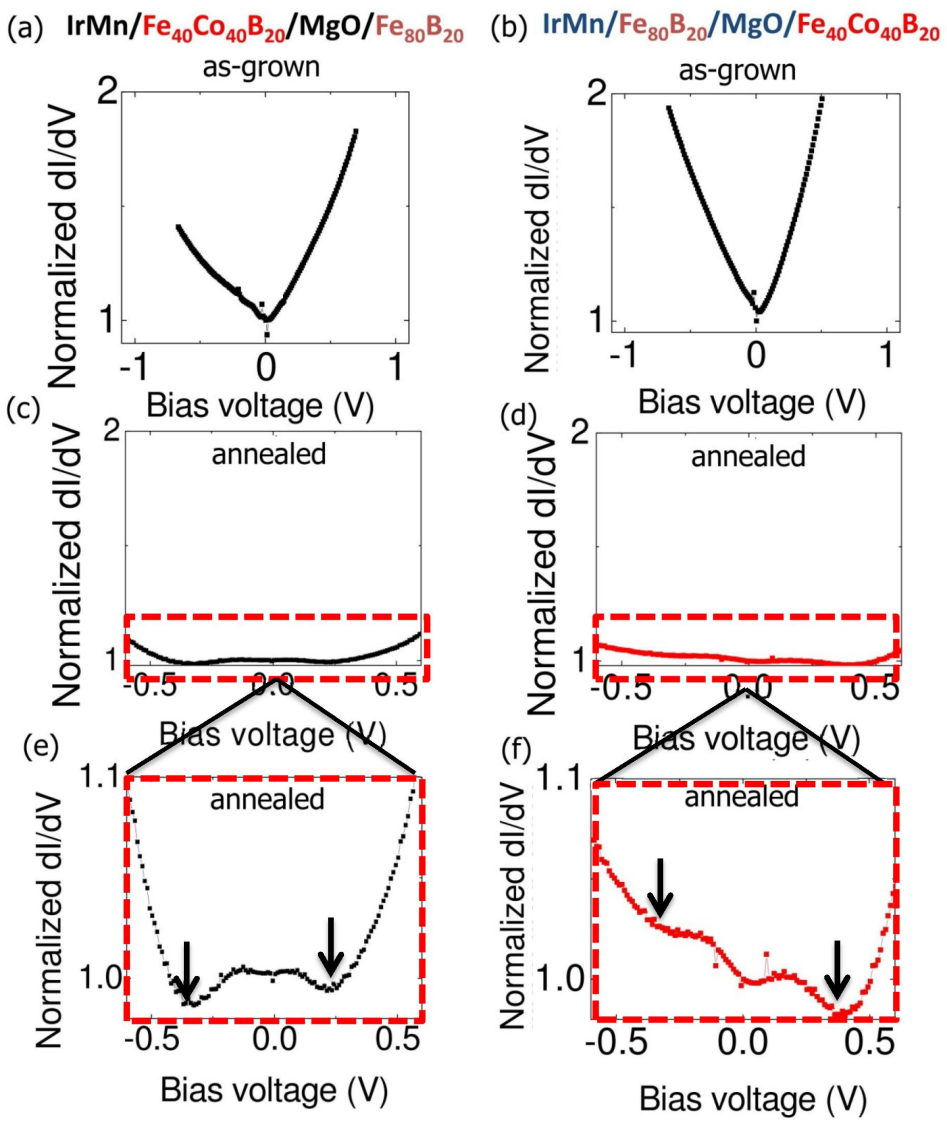

Figure 5.8: dI/dV as a function of voltage in asymmetric IrMn / $Fe_{40}Co_{40}B_{20}$ / MgO / $Fe_{80}B_{20}$ MTJs. Figures from left (right) column are devices with IrMn / $Fe_{40}Co_{40}B_{20}$ / MgO / $Fe_{80}B_{20}$ (IrMn/$Fe_{80}B_{20}$ / MgO / $Fe_{40}Co_{40}B_{20}$) (a, b) are the dI/dV in as-grown devices. (c, d) are devices after 350°C annealing. (e, f) are the same plot as (c, d) with different y-scale show the reverse of oscillatory feature while exchange the top and bottom ferromagnetic electrodes.

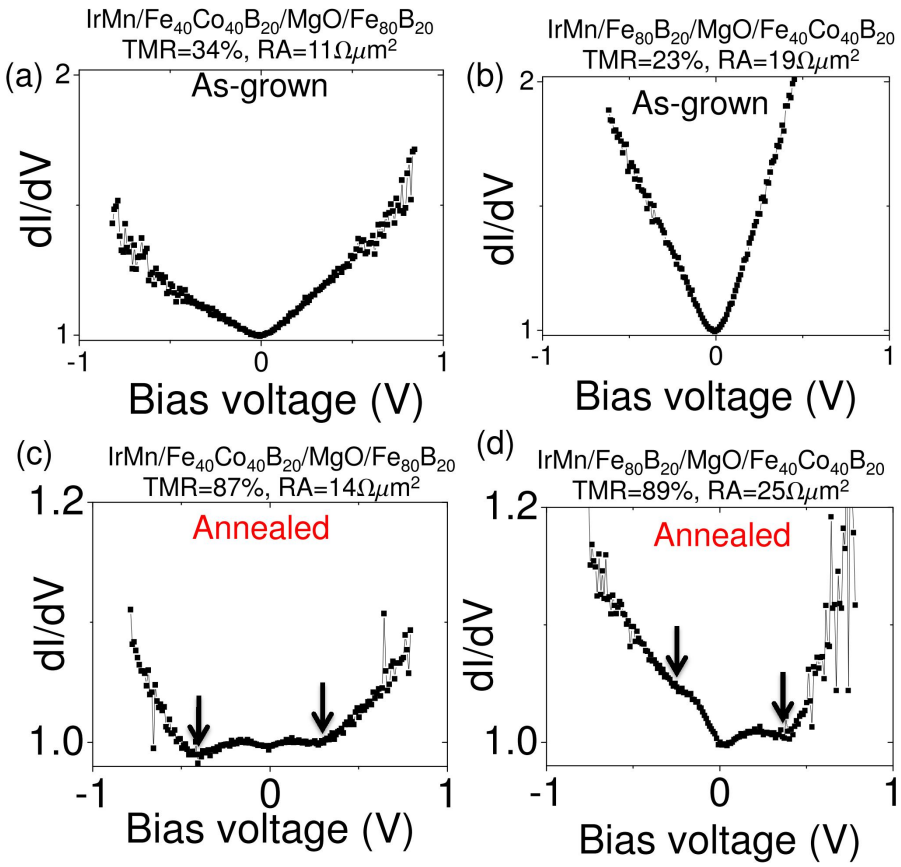

Figure 5.9: As-grown and annealed tunneling conductance as a function voltage dI/dV-V in the asymmetric low-RA IrMn / $Fe_{40}Co_{40}B_{20}$ / MgO / $Fe_{80}B_{20}$ and IrMn / $Fe_{80}B_{20}$ / MgO / $Fe_{40}Co_{40}B_{20}$ nanopillar MTJs.

Figure 5.8 and 5.9 show the tunneling conductance as a function of voltage dI/dV-V curves from different RA-products in the asymmetric IrMn / $Fe_{40}Co_{40}B_{20}$ / MgO / $Fe_{80}B_{20}$ MTJs and in the similar structures, IrMn / $Fe_{80}B_{20}$ / MgO / $Fe_{40}Co_{40}B_{20}$ (in which $Fe_{40}Co_{40}B_{20}$ and $Fe_{80}B_{20}$ electrode are reversed). Figure 5.8 shows high RA-product asymmetric microjunction MTJs and figure 5.9 shows low RA asymmetric nanopillar MTJs. In the as-grown MTJs, the dI/dV-V plot exhibits a stronger increase in the positive voltage than in the negative voltage. Annealed MTJs show not only weak voltage dependence

which has been observed in $Fe_{60}Co_{20}B_{20}$ / MgO / FeNiB, but also exhibit dips (local minimums) and shoulders (local maximums) in the dI/dV-V. In IrMn / $Fe_{40}Co_{40}B_{20}$ / MgO / $Fe_{80}B_{40}$, the dips appearing in parallel conductance are close to -0.40V and +0.25V (figure 5.8(e)). On the other hand, in IrMn / $Fe_{80}B_{20}$ / MgO / $Fe_{40}Co_{40}B_{20}$ the dips appeared in the bias voltages closer to +0.4V and -0.3V(figure 5.8(f)). The bias voltage locations of dips and shoulders in dI/dV-V remain the same regardless of tunnel barrier thickness, device area, and measuring temperatures. The amplitude of dips and shoulders, however, changes under various MgO thicknesses. This result suggests that the voltage locations of the dips and shoulders might be related to the electronic features in the electrode or electrode/interface, since these fine oscillation features do not change their locations. More detailed discussions will be presented in the next section.

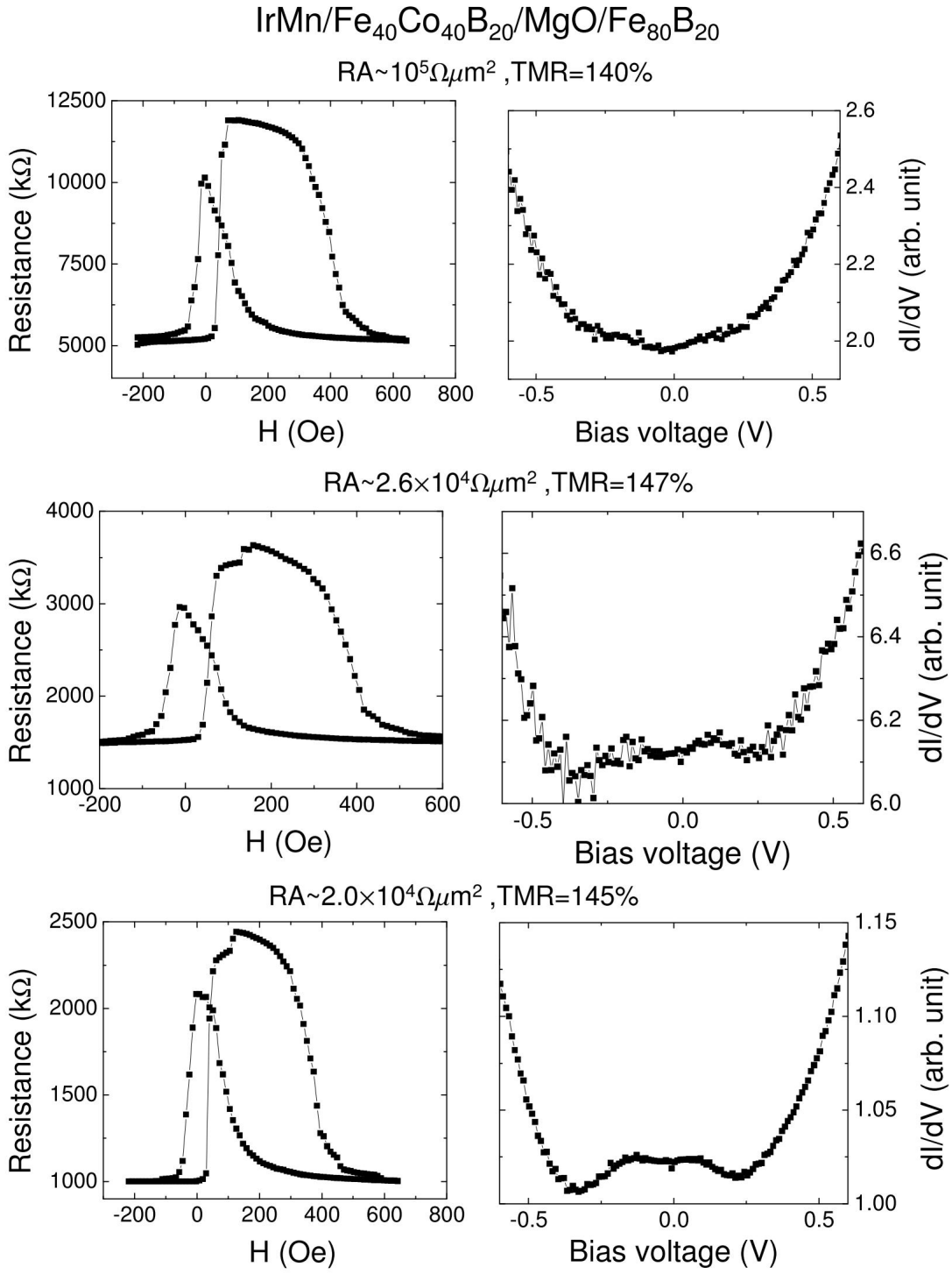

Figure 5.10: Various RA-product high TMR (>100%)$Fe_{40}Co_{40}B_{20}/MgO/Fe_{80}B_{20}$ micro junctions. The local minimum features appear in all the tunneling conductance and remain constant regardless of tunnel barrier thickness.

Figure 5.10 shows the H-R loop and tunneling conductance dI/dV of $Fe_{40}Co_{40}B_{20}$/MgO/$Fe_{80}B_{20}$ MTJs. The three different samples shown in figure 5.10 are from the same $Fe_{40}Co_{40}B_{20}$/MgO/$Fe_{80}B_{20}$ wafer. The variation of the RA-product is achieved using a wedged MgO layer. The dips and shoulders appearing in the dI/dV-V do not change the voltage bias locations, but the amplitudes do vary with different MgO thickness. The dips and shoulders almost disappear in the thick MgO MTJs, but are much stronger with a thin MgO. Another sample with the IrMn / $Fe_{80}B_{20}$ / MgO / $Fe_{40}Co_{40}B_{20}$ stack shows similar results in the variation of features with various MgO thickness (data not shown here).

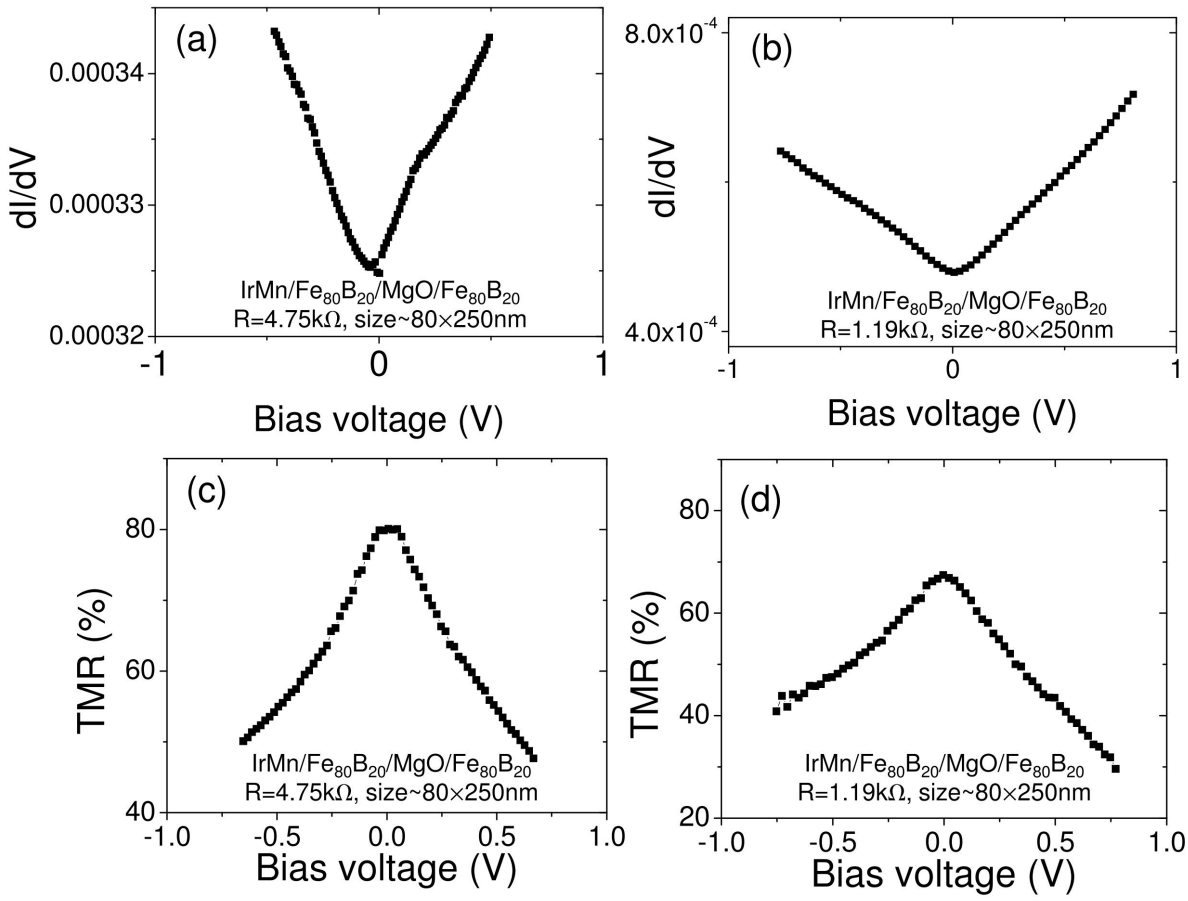

Figure 5.11: Tunneling conductance dI/dV and TMR bias dependence of $Fe_{80}B_{20}/MgO/Fe_{80}B_{20}$ from nanopillar devices. The high RA $Fe_{80}B_{20}/MgO/Fe_{80}B_{20}$ structure exhibits less asymmetry in the TMR bias dependence than the low RA devices.

Figure 5.11 show the tunneling conductance and TMR bias dependence of $Fe_{80}B_{20}/MgO/Fe_{80}B_{20}$ nanopillar devices. High RA devices exhibit symmetric TMR bias dependence, but low RA show asymmetry in the TMR bias dependence. Similar asymmetry in TMR voltage bias dependence is also reported by Yuasa et al.[92]. They attributed this asymmetry to dislocation in the bottom and top electrode between the Fe/MgO interfaces. Here, we attribute this TMR asymmetry in the symmetric Fe/MgO/Fe junction to the over-oxidized bottom

electrode.

To conclude, in our observations of the tunneling conductance dI/dV-V, we found small oscillation features associated with ferromagnetic electrode materials. The local dips and shoulders features can be reversed when the electrodes are reversed. The signal amplitude of small oscillation features is sensitive to MgO tunnel barrier thickness. The location, however, is not. These small oscillations may be associated with the electronic structure of the $Fe_{40}Co_{40}B_{20}$/MgO and $Fe_{80}B_{20}$/MgO interfaces. The details of the possible explanation will be discussed in the next section.

5.3.2 Discussion of the Tunneling Condutance Features

To explain the small oscillation features within ±1.0V in the tunneling conductance, we must consider the DOS effect. First, we have found that both as-grown samples show identical TMR and conductance bias dependence. After annealing, the TMR bias dependence and conductance have shown totally opposite voltage bias dependence. The reversal of the conductance-voltage curve indicates that the annealed device is dominated by electrode materials or the electrode/barrier interfaces. In the as-grown samples, the growing process of tunnel barrier dominates the spin-dependent transport properties. In addition, we also grew RF-sputtered MgO under different powers (100W and 300W). With 300W MgO, the growth time for 1nm MgO is ~1min. For 100W MgO, the growth time is ~3min. We found that with 300W MgO, the as-grown symmetric junctions show more symmetric TMR and conductance bias dependence than with 100W grown MgO.

Briefly, the tunneling current $I_{L\to R}$ and tunneling conductance dI/dV-V in MTJs can be described with the following formula from the ballistic model of tunneling is

$$I_{L\to R} = \int_{\epsilon}^{\epsilon+eV} D_L(E_F) D_R(E_F + eV) dE \tag{5.2}$$

The differentiate tunneling conductance is proportional to the product of the DOS:

$$\frac{dI}{dV} \propto D_L(E_F) D_R(E_F + eV) \tag{5.3}$$

According to Eqn. 5.3, we can measure the tunneling conductance to estimate the DOS. We, therefore, studied the tunneling conductance as a function of voltage in as-grown and annealed symmetric and asymmetric MTJ samples. This equation has been commonly applied in the scanning tunneling microscopy experiments (STM) to probe the electronic structure of the surface states at the nanometer scale. However, conclusive experiments to observe the electronic structure of a normal metal are few[82, 39]. LeClair *et al.*[39] pointed out several difficulties associated with observing the band structure or DOS in normal metal junctions. First, the bands or DOS contributing to the tunneling conductance are believed to be from highly dispersive *s*-hybridized bands[88]. Second, there are many factors which contribute to the tunneling conductance. For example, in addition to the elastic tunneling, the inelastic tunneling process (magnons and phonons) and the scattering process affect the tunneling conductance. Third, a full theoretical analysis of the same material structure is difficult to be performed with exactly the same experimental studies. Last, a well-known

physical and electronic structure which can modulated to convincingly compare with theory and experiment is rare.

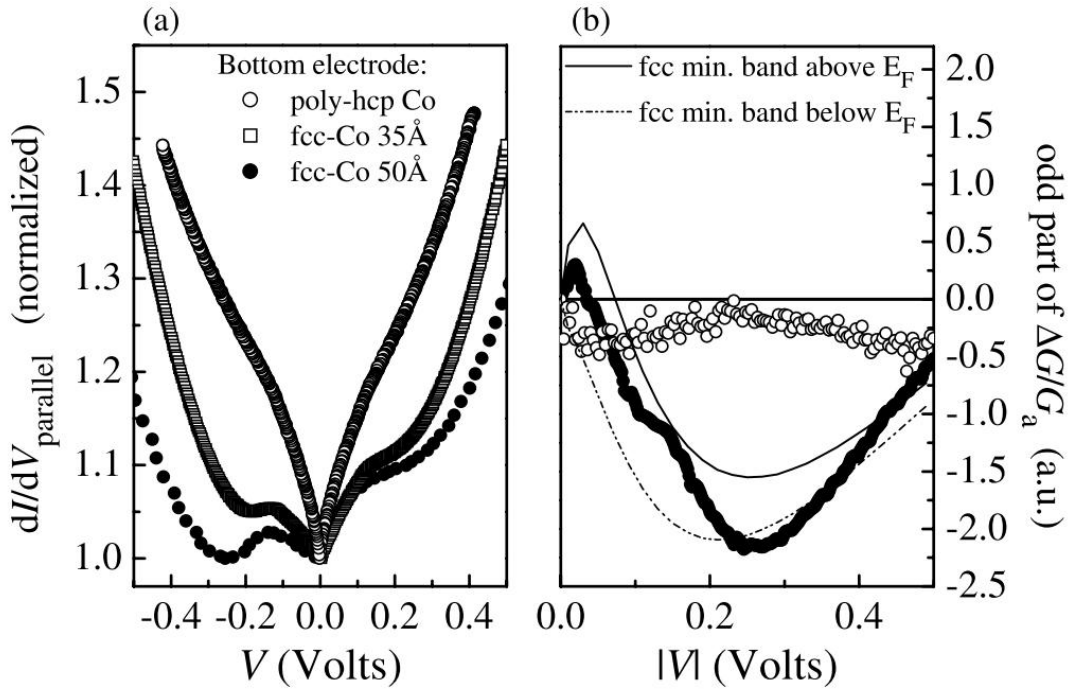

Figure 5.12: Observation of DOS effect in the poly-crystallized fcc-Co structure. (a) show the dI/dV in the parallel state with various Co electrode compositions. (b) show the odd part of ΔG/G and the bcc local minimum of DOS.

Recently, several groups have observed small oscillation features causing dips and shoulders in the tunneling conductance dI/dV-V in Co/AlO_x/Co[39], Co_2MnSi/MgO/CoFe[84] and CoFeB/MgO/CoFeB[49, 84], Co/MgO/Co[57] or the inelastic electron tunneling spectra in Fe/MgO/Fe[1] . LeClair *et al.*[39] first reported the observation of small oscillation features in the Co/AlO_x/Co (see figure 5.12). Matsumoto *et al.*[49] also observed similar features in the CoFeB/MgO/CoFeB and suggested that the Δ_5 or $\Delta_{2'}$ evanescent states are not responsible for the decrease in the parallel conductance, rather the cause of the

conductance reduction is due to the electronic structure of interfaces between MgO(001)/ bcc CoFeB(001) or a particular feature of Δ_1 states in MgO(001) or bcc CoFeB(001). One possible explanation for the local minimum can be attributed to the minority spin Δ_5. A similar explanation is also adopted by Co_2FeAl/MgO/CoFe MTJ studies by Ref. [87].

More recently, Bonell *et al.*[4] has examined the FeCo/MgO/FeCo(001) system in detail through spin- and symmetry-resolved photoemission, magneto-transport, and *ab initio* calculations to fully comprehend how the electronic structure involved in the electronic transport in the FeCo/MgO/FeCo MTJs. Bonell *et al.* further proposed that the physical mechanism can be explained by the fact that a Δ_1 symmetry minority spin state is below the Fermi level in the high Co concentration FeCo alloy, which is confirmed by both spin-resolve photoemission and *ab initio* calculation. Due to the existence of the Δ_1 symmetry minority spin state below the Fermi level, this feature could induce the decrease in tunneling conductance since there is no available state in the DOS. In addition, this result is qualitatively consistently with the bulk state calculation predicated by Schwarz *et al.*[72].

Other possible mechanisms affecting the tunneling conductance include asymmetric trapezoidal tunnel barriers[10] which lead to parabolic dependence of tunneling conductance on voltage with the minimum conductance offset from V=0. This explanation fails to explain the fine feature oscillation in the tunneling conductance. Another possible explanation is the dynamic resonant tunneling assisted by electron interference as a result of Fowler-Nordheim (FN) tunneling[22]. Electrons tunneling in the FN regime exceed the potential barrier and tunnel directly into the conduction band in the tunnel barrier. The

electrons can be treated as plane waves. These electrons may then establish standing waves within the barrier and induce resistance oscillation. This phenomena has been observed and proposed by Miller *et al.*[52] in the high TMR CoFeB/MgO/NiFeB tunnel junctions. It could provide a plausible explanation for resistance oscillation. This result, however, would not provide an explanation to the barrier-thickness independence of the oscillation features shown in figure 5.10.

To conclude, to explain the small oscillations feature in the tunneling conductance dI/dV-V on various $Fe_{80}B_{20}$ / MgO / $Fe_{40}Co_{40}B_{20}$, $Fe_{40}Co_{40}B_{20}$ / MgO / $Fe_{80}B_{20}$, $Fe_{40}Co_{40}B_{20}$ / MgO / FeNiB and $Fe_{80}B$ / MgO / $Fe_{80}B_{20}$, the peak in the minority spin state with Δ_1 symmetric in the FeCo alloy provides a reasonable explanation for the magnetotransport in FeCo/MgO/FeCo-based MTJ and similar finding in the literatures on different MgO-based or AlO_x-based MTJs. This conclusion implies that due to the significant progress of material growth technique, highly ordered ferromagnetic materials and tunnel barriers can be grown even in a sputtering system. Therefore, the band structure effect, which is originally from periodic crystal structures, can be observed. The features in the spin-dependent DOS also start to play a role in magnetotransport behaviors.

5.3.3 Results of TMR Voltage Bias Dependence in Asymmetric FeCoB/MgO/FeB MTJs

In the previous section, we found that the electronic structure of the ferromagnetic materials could affect the charge transport and the tunneling conductance dI/dV-V and could cause small oscillation features in the tunneling conduc-

tance. Spin-torque effect, however, is more sensitive to the spin-dependent transport in the MTJs. To measure the spin-dependent transport behavior in the MTJ, we could measure the TMR voltage bias dependence.

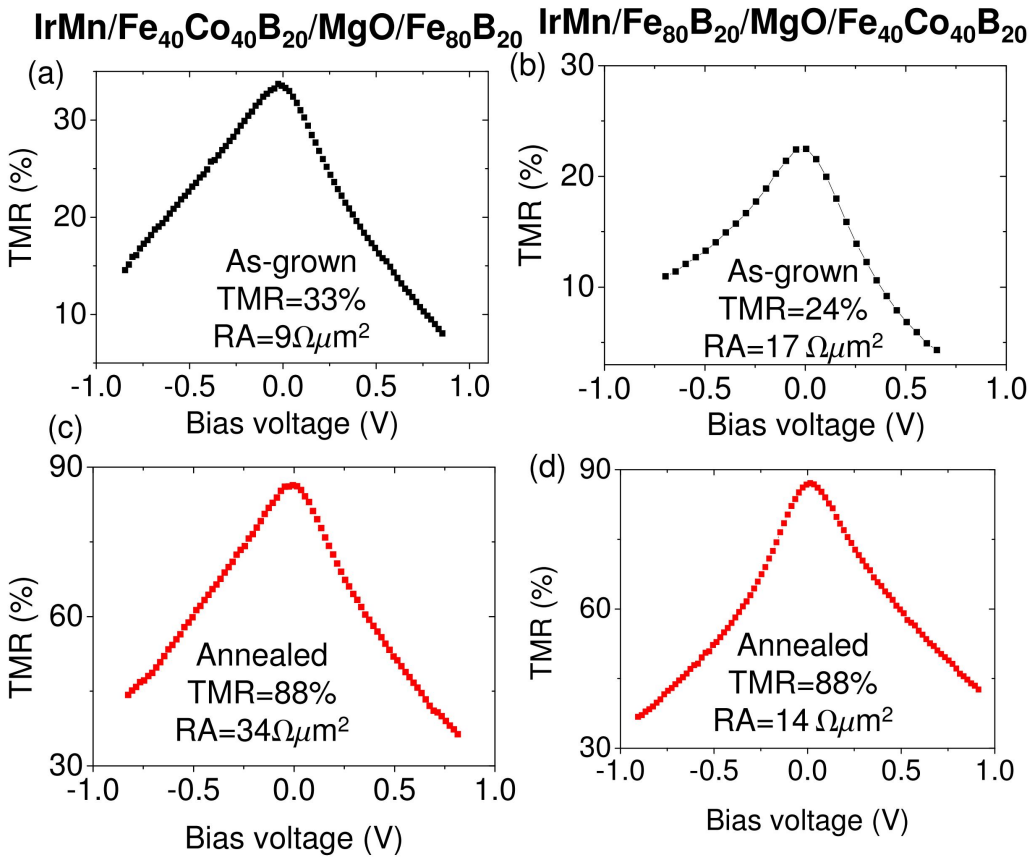

Figure 5.13: TMR voltage bias dependence in asymmetric FeCoB / MgO / FeB MTJs. (a, b) are as-grown and (c, d) are annealed MTJs. (a, c) are TMR-V from the IrMn / $Fe_{40}Co_{40}B_{20}$ / MgO / $Fe_{80}B_{20}$ layer structure (b, d) are TMR-V from IrMn/$Fe_{80}B_{20}$ / MgO / $Co_{40}Fe_{40}B_{20}$ layer structure. As-grown MTJs exhibit stronger positive TMR voltage bias dependence in both structure. Annealed MTJs, however, show stronger negative TMR voltage bias dependence.

Figure 5.13 shows the TMR as a function voltage (TMR-V) curves in as-

grown and annealed asymmetric IrMn / $Fe_{40}Co_{40}B_{20}$ / MgO / $Fe_{80}B_{20}$ and IrMn / $Fe_{80}B_{20}$ / MgO / $Fe_{40}Co_{40}B_{20}$. Regardless of electrode materials, both as-grown MTJs exhibit a stronger TMR decrease with the positive voltages than with the negative ones. The TMR decrease rate with respect to voltage is 29.8%/V for positive voltages and 22.5%/V for negative voltages. In the annealed MTJs, the TMR decrease rates are opposite. IrMn / $Fe_{40}Co_{40}B_{20}$ / MgO / $Fe_{80}B_{20}$ (Fig.5.13c) display a strong TMR decrease with positive voltage, but IrMn/FeB/MgO/FeCoB exhibits a stronger TMR decrease with negative voltages than with positive ones. For example, annealed IrMn/FeCoB/MgO/FeB (Fig.5.13(c)) has a TMR decrease rate of 51.2%/V for negative voltages and 58.9%/V for positive voltages. These results point out that the electronic structure in the FeB/MgO, FeCoB/MgO interfaces, or the band structure of $Fe_{80}B_{20}$ and $Fe_{60}Co_{20}B_{20}$ dominate the TMR voltage bias dependence TMR-V in the annealed asymmetric MTJs. This differs from the growing process of over-oxidized bottom electrodes in the as-grown MTJs.

5.3.4 Discussion

To explain our TMR voltage bias dependence results, we first consider the spin-polarized tunneling in the MTJ. Early spin-polarized tunneling experiments by Meservey and Tedrow showed that conduction electrons in ferromagnetic metals are spin-polarized, and the spin is conserved in the tunneling process. Julliére's model[31] further predicted that the TMR in ferromagnet/insulator/-ferromagnet could be represented by the following formula:

$$TMR = \frac{G_P - G_{AP}}{G_{AP}} = \frac{2P^L_{spin}P^R_{spin}}{1 - P^L_{spin}P^R_{spin}} \tag{5.4}$$

Where $G_{AP,P}$ is the conductance of parallel and anti-parallel state of MTJs. $P^{L,R}_{spin}$ is the spin-polarization of two ferromagnetic electrodes. The TMR decrease directly reflects the decrease in the spin polarization of tunneling electrodes.

Currently, the TMR voltage bias dependence is still not well understood. Several possible explanations include conductance increases, magnon excitation, and the band structure effect lowering spin polarization. Detailed discussions of the physical mechanisms of TMR bias dependence can be found in Ref.[55]. Calculations show that magnon excitation plays a significant role in TMR bias decreases[93, 9]. These theoretical explanations, however, cannot provide a explanation of local minimum features of the high TMR MgO MTJ with spin-filtering effect, which will be shown in the later figures 5.8. Typically, asymmetric TMR voltage bias dependence in $Co/Al_2O_3/Py$ has been reported [54, 55]. The band structure effect lowering spin polarization usually is considered as small effects. Recent discoveries of high TMR MgO-based MTJs[92, 61] due to the spin-filtering effect, has overcome the limitation of TMR based on the simple Julliére model which only considers ferromagnetic electrodes. This is different from Al_2O_3-based MTJs. The voltage dependence of the parallel conductance in the MgO-based MTJ is much weaker compared to anti-parallel conductance.

The explanation that strong DOS in the minority band induces the small oscillation in the tunneling conductance and asymmetry in the asymmetric TMR voltage bias dependence is able to provide a quantitative understanding of the magnetotransport results in the electric and spin-dependent transport features.

First, a strong local minimum has been commonly observed in several MgO-based tunnel junctions. The locations of local minimals have been consistently in the same location regardless of different resistance area product (my data). This suggests that the local minimum results from ferromagnetic electrode materials instead of MgO tunnel barriers. When we reversed the $Fe_{40}Co_{40}B_{20}$ / MgO / $Fe_{80}B_{20}$ to $Fe_{80}B_{20}$ / MgO / $Fe_{40}Co_{40}B_{20}$ (IrMn remained in the bottom electrode), the local minimum also changed to a different location. In addition, theoretical calculations also show that bcc Fe(001) has a stronger local DOS in the minority band than bcc Co in the higher energy, and since TMR is related to the spin polarization of electric currents, the large DOS in the minority band will also reduce the spin-polarization and therefore the low TMR with positive voltage bias.

However, recent experimental results suggest that the effective spin polarization of tunneling electron currents also depends on the tunnel barrier and structure in the magnetic multilayer stack[71]. Teresa *et al.*[82] show that the TMR ratio in $Co/SrTiO_3/La_{0.7}Sr_{03}MnO_3$ junction exhibits negative TMR (-50%), and the barrier can affect and even reserve the spin polarization of tunneling currents. Shi *et al.*[73] has shown important results by using STEM EELS with aberration corrected STEM operated at 200kV. They have a clear image of low inverse TMR $CoFe/AlO_x/CoFe$ showing a thin and discontinous Fe_3O_4

5.3.5 Results of Spin-torque Effects in Asymmetric $Fe_{40}Co_{40}B_{20}$ / MgO / $Fe_{80}B_{20}$ MTJs

In previous sections I have discussed how the electronic structures in the ferromagnetic materials affect both the charge (tunneling conductance dI/dV-V) and spin-dependent transports (TMR voltage bias dependence) in the MTJs. In this section, I will present the spin-torque effect measurement in the asymmetric and symmetric MTJs based on four different electrode configurations.

To estimate the spin-torque effect in a nanopillar MTJ device, we measure the switching phase diagram, which measures the variation of antiparallel-to-parallel (AP-to-P) and parallel-to-antiparallel (P-to-AP) switching fields under various DC-biased voltages. This approach enables us to directly probe the current-induced effects in the MgO-based MTJs.

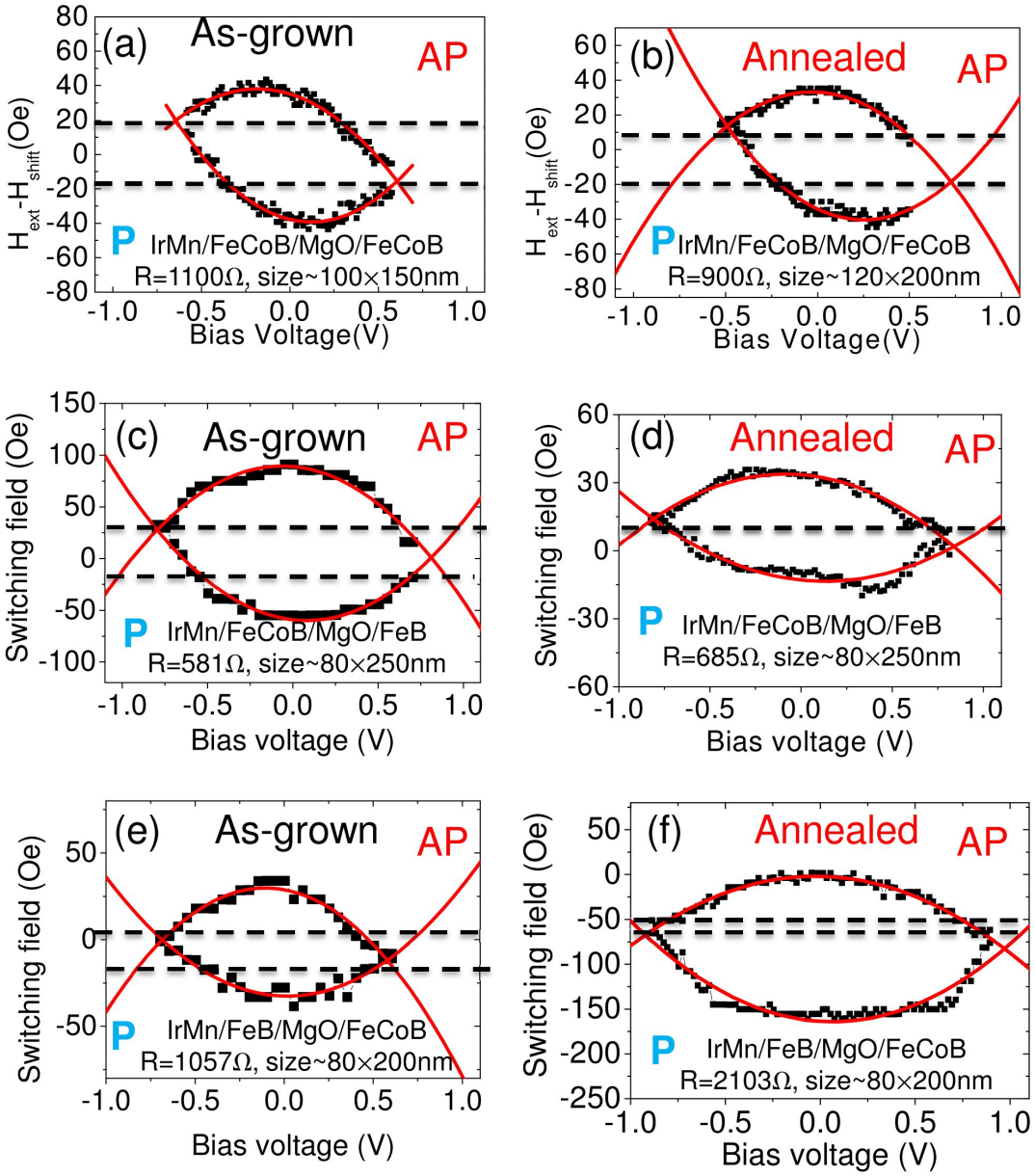

Figure 5.14: Switching phase diagrams in symmetric IrMn / $Fe_{40}Co_{40}B_{20}$ / MgO / $Fe_{40}Co_{40}B_{20}$ and asymmetric IrMn / $Fe_{40}Co_{40}B_{20}$ / MgO / $Fe_{80}B_{20}$ MTJs. (a, c, e) are the SPDs of as-grown nanopillar MTJs. (b, d, f) are the SPDs of annealed nanopillar MTJs. TMR for those MTJs are ≈20% for as-grown MTJs and ≈90% for annealed MTJs.

Figure 5.14 shows DC-biased switching phase diagrams of both symmetric $Fe_{40}Co_{40}B_{20}$ / MgO / $Fe_{40}Co_{40}B_{20}$ and two asymmetric $Fe_{40}Co_{40}B_{20}$ / MgO / $Fe_{80}B_{20}$ MTJs. In figure 5.14(a, c, e) are the SPD of as-grown MTJs and (b, d, f) are the SPD of annealed MTJs. The two dot lines in the SPD represent a region (between the lines) in which the MTJ is capable of performing bipolar switching. At least three samples are measured for each type of devices. The SPD are not highly repeatable from sample to sample. Consistent features in the SPDs, however, can still be found in different types of devices. The first repeatable feature in the SPD is that SPDs of as-grown MTJs usually exhibit larger areas of bipolar switching when compared to their own annealed devices, with the exception of symmetric $Fe_{40}Co_{40}B_{20}/MgO/Fe_{40}Co_{40}B_{20}$ devices. The second repeatable feature is the dramatic switching behavior changes in the SPD (d, f). Our DC-biased SPD measurement has a strong heating effect under high voltage bias due to the RA of our MTJ nanopillars. To analyze the SPD results, we could estimate the spin-torque vectors based on the thermal-activated model[43, 44, 58],

$$H_c = H_k(1 - [\frac{2k_BT}{H_kM_sv_0}\log(tf_0)])^{1/2} \tag{5.5}$$

$$V_c = V_{c0}[1 - \frac{k_BT}{E_b}ln(t_P)f_0] \tag{5.6}$$

$$t^{\pm} = f_0^{-1}exp(\frac{E_b^{\pm}(1 \mp V/|V_C^{\pm}|)}{k_BT^*}) \tag{5.7}$$

$$E_b^{\pm} = \frac{H_KM_Sv_0}{2}(1 \pm \frac{H_{ext} - H_{sh} + b_J}{H_K})^{3/2} \tag{5.8}$$

where $t^{\pm}$ is the relaxation time, f_0 is the attempt frequency (=$10^9 s^{-1}$), k_B is the Boltzmann constant, T^* is the effective junction temperature considering the joule heating effect, H_K is the anisotropy field including the magnetocrystalline anisotropy and the shape anisotropy, $V_C^{\pm}$ is the critical switching voltage at $T^* = 0K$. This approach by fitting the SPD through thermal-activation model require multi parameter fitting (more than 5 fitting parameters). Therefore, it is difficult to provide a conclusive results to understand the spin-torque vectors in the asymmetric MTJs. Our SPD results are very complicated when compared to typical symmetric SPD. Instead of analyzing the SPD, we utilize sensitive spin-torque ferromagnetic resonance (ST-FMR) to directly probe the spin-torque effect in the symmetric and asymmetric MTJs under four different electrode configurations.

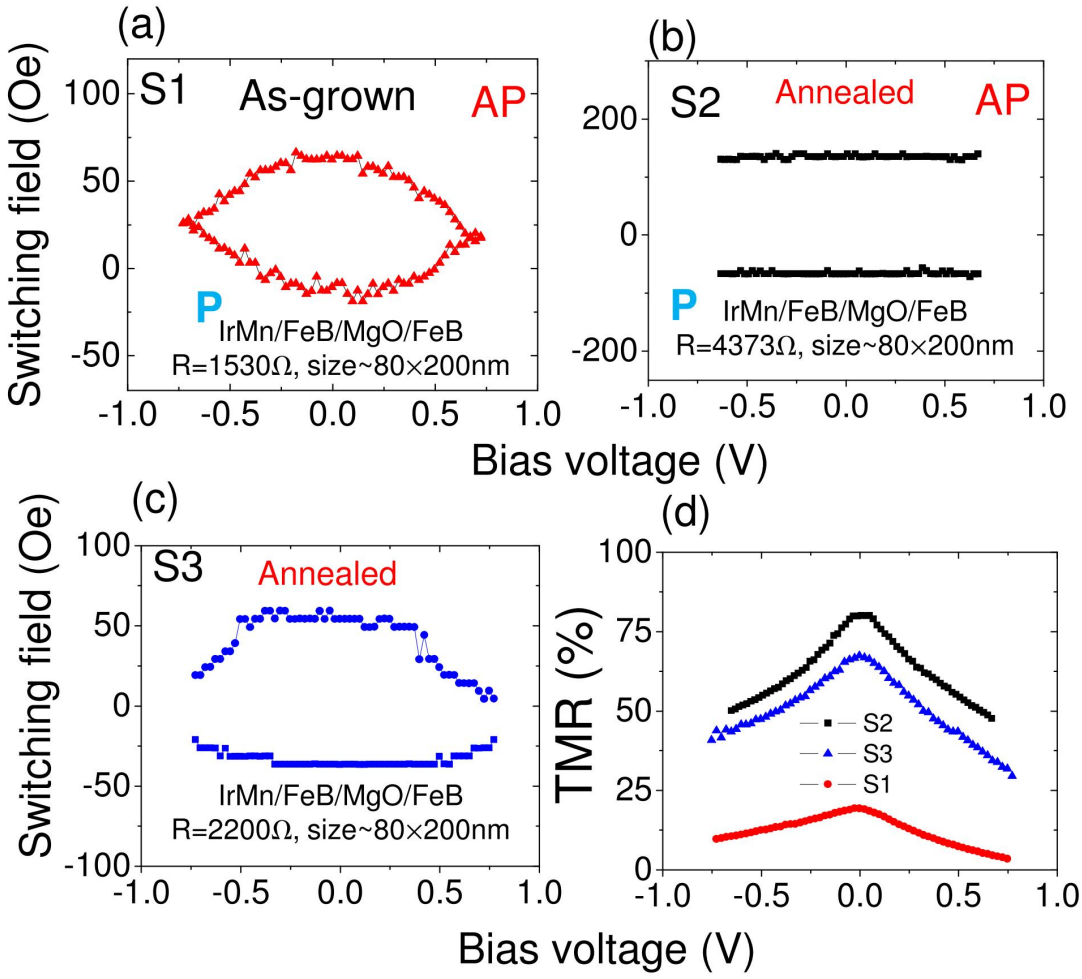

Figure 5.15: Switching phase diagrams (SPD) of various RA FeB/MgO/FeB nanopillar MTJs and TMR voltage bias dependence. (a) SPD of as-grown FeB/MgO/FeB. (b, c) SPDs of annealed FeB/MgO/FeB with two low and high RA-product. (d) TMR bias dependence of three samples.

In addition to conventional symmetric $Fe_{40}Co_{40}B_{20}$ / MgO / $Fe_{40}Co_{40}B_{20}$, we also studied the SPD of $Fe_{80}B_{20}$ / MgO / $Fe_{80}B_{20}$. Figure 5.15 shows the SPD of as-grown and annealed $Fe_{80}B_{20}$ / MgO /$Fe_{80}B_{20}$ MTJs. As-grown $Fe_{80}B_{20}$ / MgO / $Fe_{80}B_{20}$ exhibit bipolar switching within a field regime and lower RA product before annealing. After annealing, we found the RA-product increase signifi-

cantly. We could easily observed RA-product increase more than 100% in the same devices before and after annealing. In addition, the TMR voltage bias dependence exhibit significant asymmetry when comparing to CoFeB-based MgO MTJs. Similar TMR bias asymmetry also observed in the literature[92]. According to our previous studies[67, 14], Fe easily forms Fe_3O_4 next the tunnel barrier. Comparing to top electrodes, the bottom electrode could be sigifinificantly oxidized during the RF sputtering MgO process from O_2 plasma (shown in Figure 3.3).

5.4 Introduction of Spin-Torque Ferromagnetic Resonance

In the previous section, I used switching phase diagrams (SPD) to estimate the spin-torque effect in both symmetric and asymmetric MTJs. We already observed the different switching behaviors in the annealed asymmetric MTJs. However, due to our higher RA in the MTJs, the heating effect seemed to dominate the spin-torque switching effect, and it is difficult to get an accurate estimate under high voltage bias. To qualitatively measure the spin-transfer torque effect in the MTJ nanopillars, several measurement schemes have been developed in the last several years. These measurement schemes are based on thermal activation models[58], variations of microwave emission spectra[17] and spin-transfer-driven ferromagnetic resonance (ST-FMR)[69, 70, 38]. The ST-FMR technique is currently the most sensitive technique for probing the bias and angular dependence of the spin-transfer torque in the MgO-based MTJs. I will first introduce the basic concept of ST-FMR measurement, and then I will present ST-FMR measurements of both symmetric and asymmetric MTJs.

Briefly, ST-FMR measurements are made by applying a sufficiently strong external field to offset the free layer. A microwave-frequency current I_{RF} is sent through a bias-tee and is mixed with a DC voltage from the capacitor side of the bias-tee. While I_{RF} excites spin-torque-driven dynamics in the free layers, spin-torque effect will induce a resistance oscillation in the nanopillar devices. We could further enhance the signal-to-noise ratio through a lock-in amplifier by sending the I_{RF} at a lock-in frequency, such as 100Hz to 2KHz depending on the type of bias-tee.

Mathematically, we could express the I_{RF} in the following form:

$$I_{RF}(t) = |I_{RF}| \cos(\omega t) \tag{5.9}$$

where ω is the microwave frequency of the oscillating RF current. The resistance oscillation from the spin-torque device should have

$$R(t) = R_o + \Delta R \cos(\omega t + \delta) \tag{5.10}$$

where δ is the phase difference from the oscillating RF current and the resistance variation delay responding to the oscillating RF current. The voltage drop across the junction is the product of the current and the device resistance.

$$V(t) = I(t) \times R(t)$$

The mixed voltage as a function of time will be

$$V_{mix} = I_{RF} \cos(\omega t) R_o + I_{RF} \cos(\omega t)(\Delta R \cos(\omega t + \delta))$$

The time average of the DC mixed voltage from the nanopillar will be

$$< V_{mix} >= A \cos(\omega t) \cos(\omega t + \delta)$$

To quantitatively analyze the spin-torque vector from the ST-FMR DC-mixed voltage signal, we could solve the generalized Landua-Lifshitz-Gilbert equation. Note that in order for ST-FMR to work, the microwave-driven current is required to be a small perturbation, since the theoretical approach use a small perturbation approximation. Under small perturbation condition, increasing applied power is also proportional to the increasing of the FMR signal amplitude. While the amplitude of theFMR signal is no longer proportional to increasing power. This is indicated in that it is no longer in the small perturbation regimes. The LLG equation with both spin-torque vectors,

$$\frac{d\hat{\mathbf{m}}}{dt} = -\gamma\hat{\mathbf{m}} \times \mathbf{H_{eff}} \times +\alpha\hat{\mathbf{m}} \times \frac{d\hat{\mathbf{m}}}{dt} - \gamma\frac{\tau_{\parallel}(I,\theta)}{M_s Vol}\hat{\mathbf{y}} - \gamma\frac{\tau_{\perp}(I,\theta)}{M_s Vol}\hat{\mathbf{x}}, \tag{5.11}$$

where γ is the gyromagnetic ratio, α is the Gilbert damping factor, M_s is the saturation magnetization, and Vol is the volume of the nanomagnet.

$$< V_{mix} >= \frac{1}{4}\frac{\partial^2 V}{\partial I^2} I_{RF}^2 + \frac{1}{2}\frac{\partial^2 V}{\partial\theta\partial I}\frac{\hbar\gamma\sin(\theta)}{4eM_s Vol\sigma} \times I_{RF}^2(\xi_{\parallel}S(\omega) - \xi_{\perp}\Omega_{\perp}A(\omega)) \tag{5.12}$$

Here $\xi_{\parallel} = [(2e/\hbar)\sin(\theta)]d\tau_{\parallel}/dI$ and $\xi_{\perp} = [(2e/\hbar/\sin(\theta))]d\tau_{\perp}/dI$ are the dimensionless units of the differential torques. The $S(\omega)$ is the symmetric Lorentzian $S(\omega) = 1/1 + [(\omega - \omega_m)/\sigma]^2$ and $A(\omega)$ is the anti-symmetric Lorentzian $A(\omega)[(\omega - \omega_m)/\sigma]S(\omega)$. σ is the ST-FMR peak linewidth and ω_m is the resonant frequency.

5.5 Results and Discussions of In-Plane and Out-of-Plane Torque in Asymmetric and Symmetric MTJs

Previously, we observed that field-like torque can be significantly enhanced in the annealed high TMR symmetric FeCoB-based MgO MTJs. This result indicates electronic structures play a significant role in the spin-torque effect in the MgO MTJs. We further utilize the ST-FMR technique to measure spin-torque vectors in asymmetric and symmetric MTJs with four different electrode configurations.

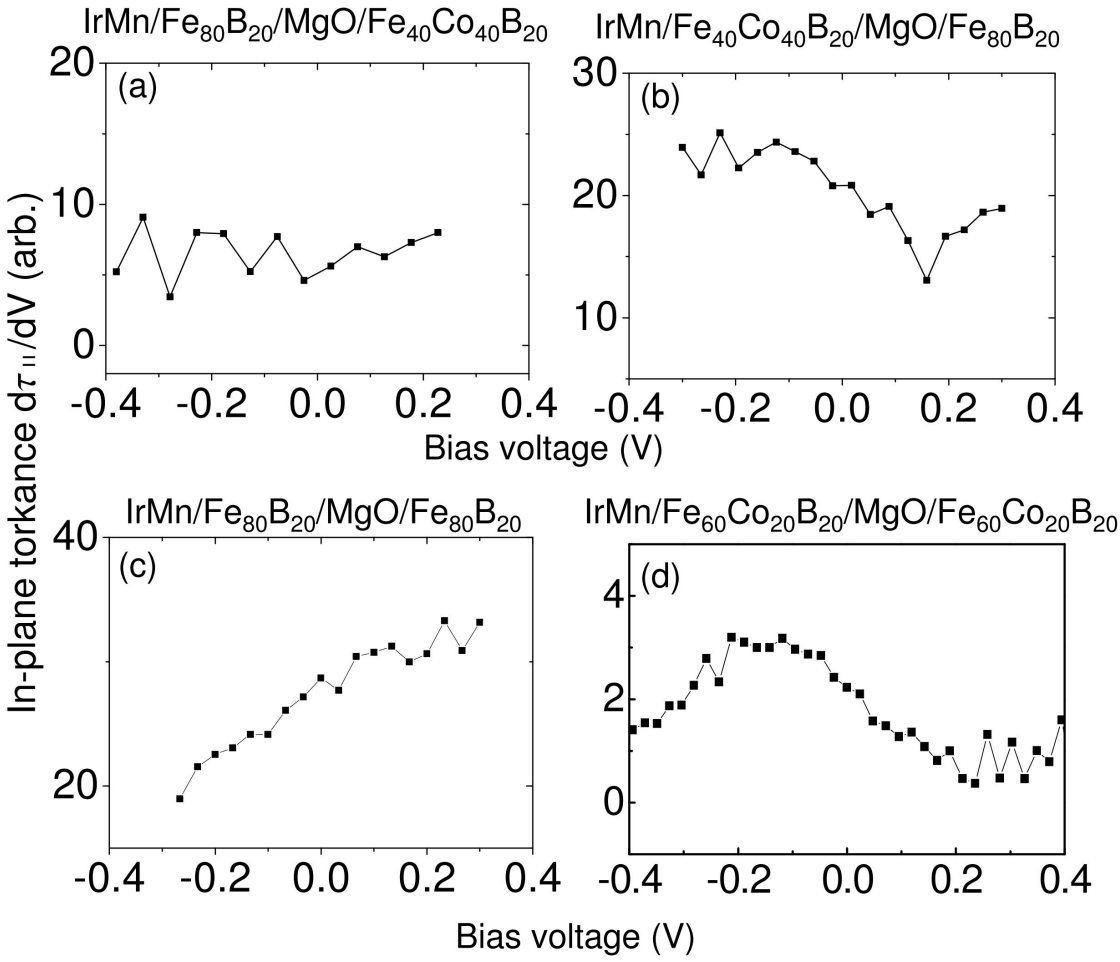

Figure 5.16: The in-plane torkance $d\tau_{\parallel}/dV - V$ as a function of voltage based on spin-torque FMR measurements of four various electrode configurations in high TMR MgO-base MTJs. (a) IrMn /$Fe_{80}B_{20}$ / MgO /$Fe_{40}Co_{40}B_{20}$. (b) IrMn /$Fe_{40}Co_{40}B_{20}$ / MgO /$Fe_{80}B_{20}$. (c) IrMn /$Fe_{80}B_{20}$ / MgO /$Fe_{80}B_{20}$. (d) IrMn /$Fe_{60}Co_{20}B_{20}$ / MgO /$Fe_{60}Co_{20}B_{20}$ (Results in (d) from Yun Li).

Figure 5.16 shows the spin-transfer torkance with respect to bias voltage from the ST-FMR measurement with four different electrode configuration MTJs: the asymmetric IrMn / $Fe_{40}Co_{40}B_{20}$ / MgO / $Fe_{80}B_{20}$ and IrMn / $Fe_{80}B_{20}$ / MgO / $Fe_{40}Co_{40}B_{20}$ and symmetric MTJs IrMn / $Fe_{60}Co_{20}B_{20}$ / MgO /

$Fe_{60}Co_{20}B_{20}$ and IrMn / $Fe_{80}B_{20}$ / MgO / $Fe_{80}B_{20}$. First, we found that the symmetric $Fe_{80}B_{20}$ / MgO / $Fe_{80}B_{20}$ exhibit stronger torkance with positive voltage (V>0) rather than negative voltage (shown in figure 5.16(c)). Typical IrMn / $Fe_{60}Co_{20}B_{20}$ / MgO / $Fe_{60}Co_{20}B_{20}$ structures exhibit weak torkance with positive voltage (shown in figure 5.16(d). Similar torkance behavior of FeCo-based MgO MTJs can also be observed in Ref. [85, 86]. This torkance profile in $Fe_{80}B_{20}$ / MgO / $Fe_{80}B_{20}$ (shown in the figure 5.16) suggests strong and opposite asymmetric in-plane torque when compared to typical IrMn / $Fe_{60}Co_{20}B_{20}$ / MgO / $Fe_{60}Co_{20}B_{20}$ MTJs.

	Fe	Co	Ni
J [a] (eV)	1.5	1.1	0.6
W[b] (eV)	4.67–4.81	5	5.04–5.35

Figure 5.17: Exchange splitting and work functions for Fe, Co and Ni ferromagnetic transition metals. (from Ref. [19, 51]). This table is from Ref. [47]

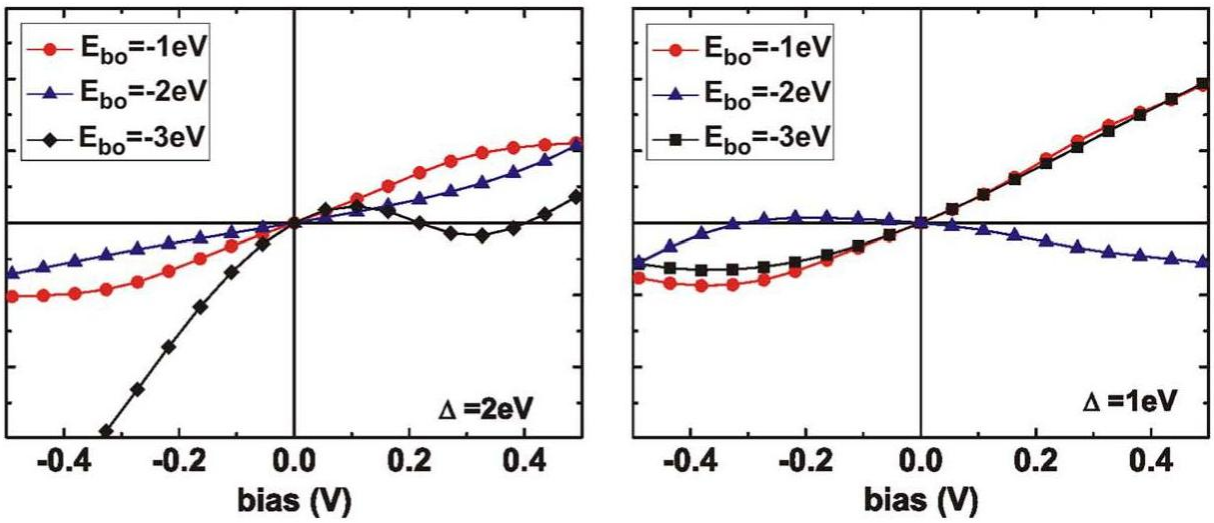

Figure 5.18: The in-plane torque $\tau_{\parallel}$ as a function of the bias voltage for two different exchange splitting energies Δ. Fe corresponding to Δ = 2eV and E_{bo} = −1eV and $Fe_{50}Co_{50}$ corresponding to Δ = 1eV and (From Ref. [36].

Comparing our results to theoretical calculations is not trivial. Several theoretical studies have predicted how electrode materials in the MTJ can influence spin-torque vectors in asymmetric MTJs[29, 80, 81, 47]. It is pointed out that simplified simple band structures of ferromagnetic materials might not be able to correctly predict spin-torque vectors[36], especially for field-like torque which requires integration over all energies over all occupied states in ferromagnetic materials. Here, we compare our result with the theoretical calculation by Khalil *et al.*[36] and using the experiment results of exchange splitting energy and work functions of Fe, Co and Ni from [51, 19]. The exchange splitting energy J is 1.5eV for Fe and 1.1eV for Co. The work functions W(eV) is ~4.7eV for Fe and is 5eV for Co. Figure 5.18 show the theoeretical calculation of in-plane torque as a function of the vias voltage under two different exchange splitting energy Δ. To compare our results with theory, the $Fe_{80}B_{20}$ / MgO /$Fe_{80}B_{20}$ is close to

$\Delta = 2eV$ and $E_{bo} = -1eV$ (figure 5.18(a)) and $Fe_{60}Co_{20}B_{20}$ / MgO / $Fe_{60}Co_{20}B_{20}$ is close to $\Delta = 1eV$ and $E_{bo} = -1eV$ or -2eV(figure 5.18(b)). (Note that the current polarity convention in the Ref. [36]is consistent with our measurement.) Our torkance measurement results, however, are not even qualitatively consistent with the calculation in figure 5.18, but exhibit opposite trend in the strength of torkance in terms of voltage polarity. Possible explanation for this inconsistency can be attributed to using the over-simplified one-band model to describe the band structure of Fe and FeCo.

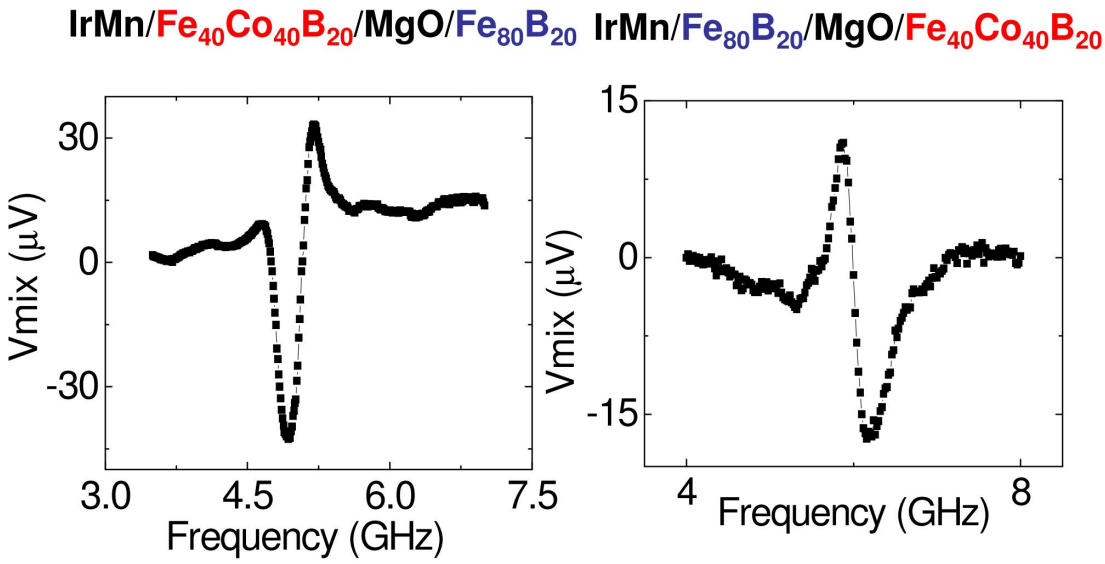

Figure 5.19: Spin-torque FMR measurements of two different asymmetric MTJs. (a) IrMn /$Fe_{40}Co_{40}B_{20}$ /MgO /$Fe_{80}B_{20}$ and (b) IrMn /$Fe_{80}B_{20}$ /MgO /$Fe_{40}Co_{40}B_{20}$. The sign of anti-symmetric Lorentzian reverse as the electrode configuration reverse in the $Fe_{40}Co_{40}B_{20}$ /MgO /$Fe_{80}B_{20}$ to $Fe_{80}B_{20}$ /MgO /$Fe_{40}Co_{40}B_{20}$. This indicates that the sign of the torkance is also opposite.

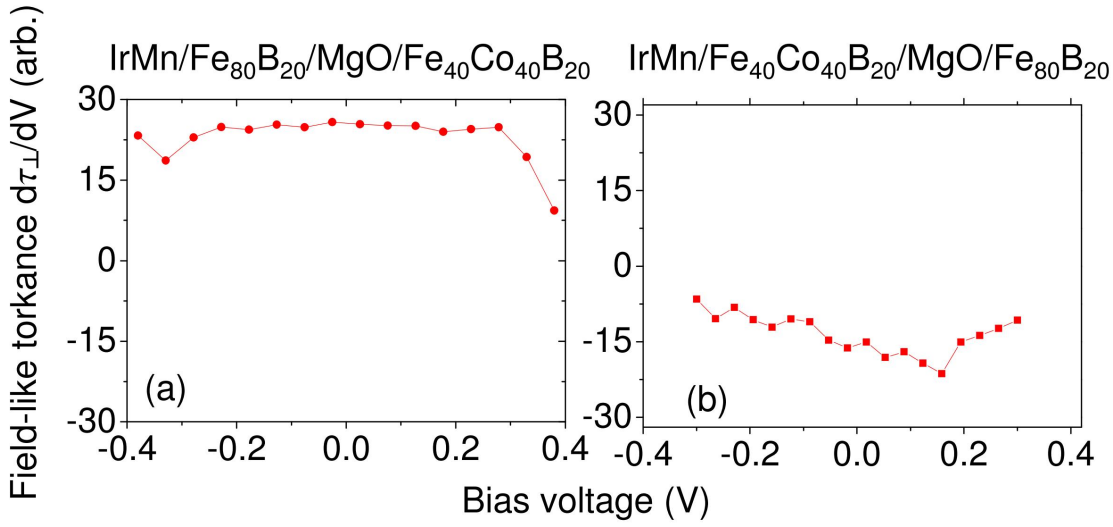

Figure 5.20: Field-like torkance as a function of bias voltage in (a) $Fe_{80}B_{20}$ /MgO /$Fe_{40}Co_{40}B_{20}$ MgO MTJs and (b) $Fe_{40}Co_{40}B_{20}$ /MgO /$Fe_{80}B_{20}$.

Figure 5.19 shows the ST-FMR signal of asymmetric $Fe_{80}B_{20}$ /MgO /$Fe_{40}Co_{40}B_{20}$ MgO MTJs and $Fe_{40}Co_{40}B_{20}$ /MgO /$Fe_{80}B_{20}$. MTJs. The difference in the anti-symmetric Lorentzian indicates the opposite sign of field-like torkance. Figure 5.20 shows the field-like torkance as a function of bias voltage of asymmetric $Fe_{80}B_{20}$ / MgO / $Fe_{40}Co_{40}B_{20}$ MgO MTJs and $Fe_{40}Co_{40}B_{20}$ / MgO / $Fe_{80}B_{20}$. The sign of two asymmetric MTJs are opposite with symmetry argument, since this two structures are basically the same. Another interesting features is the weak voltage dependence of the field-like torkance in the asymmetric MTJs, which is different from conventional symmetric CoFeB-based MgO MTJs [70, 85, 86]. To confirm this result, I also performed the same measurement on the symmetric CoFeB/MgO/CoFeB device. However, only symmetric Lorentzian is observed in symmetric MTJs at zero bias V=0. Tang *et al.*[81] show that in asymmetric MTJs which symmetry is reserved (ferromagnetic elec-

trodes). The field-like torkances exhibit opposite sign and weak voltage bias dependence which is consistent with our ST-FMR results (shown in figure 5.20). Other possible explanation of this anti-symmetric Lorentzian signal could also originate from the device electric circuit, such as the capacitance. Our device geometry, however, has been used in the similar spin-valve system.

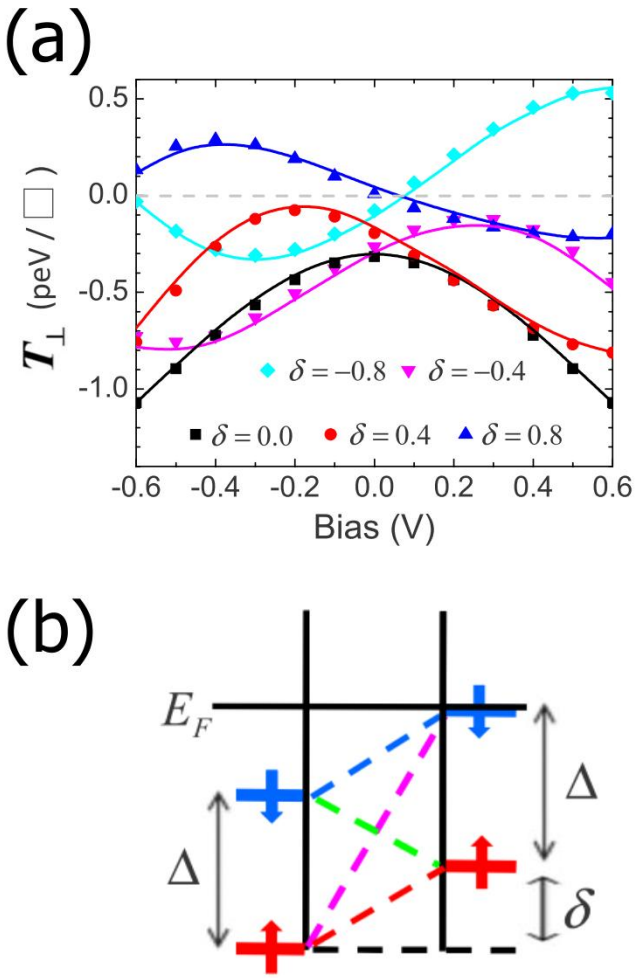

Figure 5.21: (a) is the theoretical calculation of bias dependence of field-like torque $T_\perp$ for $\theta = \pi/2$ (figures are from Ref.[81]). Where Δ is the exchange splitting energy and δ is the energy difference in the Fermi level. The variations of field-like torques vary significantly with respect to different band structure parameters. Interestingly, the signs of field-like torque could possibly exhibit sign-changes and encourage parallel coupling. (b) is an illustration of the simplified band structure.

5.6 Conclusion

The magnetotransport, TMR bias dependence and spin-torque effects in asymmetric $Fe_{60}Co_{20}B_{20}$/MgO/FeNiB, $Fe_{40}Co_{40}B_{20}$/ MgO/ $Fe_{80}B_{20}$ and symmetric $Fe_{40}Co_{40}B_{20}$/MgO/$Fe_{40}Co_{40}B_{20}$, $Fe_{80}B_{20}$/MgO/$Fe_{80}B_{20}$ MTJs have been studied. The tunneling conductance dI/dV-V results show that the interfacial states existing in the interface between the FeCo alloy and MgO with Δ_1 symmetry close to the Fermi level could induce the dips and shoulders in the tunneling conductance. The reversal of TMR voltage bias dependence in the electrode-reversed asymmetric $Fe_{40}Co_{40}B_{20}$/MgO/$Fe_{80}B_{20}$ MTJs suggest the voltage bias difference of spin-polarization between the $Fe_{40}Co_{40}B_{20}$/MgO and $Fe_{80}B_{20}$/MgO interfaces. In addition, the interfacial states only manifested after annealed highly ordered FeCo-based MgO MTJs. In the as-grown MTJs, the sputtering process dominate the magneotransport and TMR voltage bias dependence regardless of the ferromagnetic materials. ST-FMR result show the in-plane torque in symmetric $Fe_{80}B_{20}$/MgO/$Fe_{80}B_{20}$ MTJs exhibit opposite asymmetry compared to conventional CoFeB/MgO/CoFeB MTJs. So far, theoretical prediction still lack of consistent prediction of the in-plane torque behavior even in the simple Fe/MgO/Fe MTJ. Results based on the simple band structure vary significantly even with small changes in the parameters. In asymmetric $Fe_{40}Co_{40}B_{20}$/MgO/$Fe_{80}B_{20}$ and $Fe_{80}B_{20}$/MgO/$Fe_{40}Co_{40}B_{20}$ MTJs, the field-like torkance change sign, which suggest highly asymmetry in the field-like torque with high voltage bias.

CHAPTER 6

HIGH VOLTAGE SPIN-TRANSFER EFFECT MEASUREMENT

6.1 Introduction

Spin torque (ST) enables the electrical manipulation of nanomagnets and is being extensively studied due to its potential applications in the fast, scalable non-volatile magnetic random access memory (ST-MRAM) utilizing magnetic tunnel junctions (MTJs).Very fast, ≈1ns, ST switching of MTJs requires high pulse voltages (0.5 to 1.0+ V). At such pulse level, the ST switching behavior is often unreliable for one bias polarity, although the switching may be fully reliable for longer, lower voltage pulses. This issue of back-hopping[78] in fast ST switching could substantially hinder progress towards commercialization of ST-MRAM. The resolution requires an improved understanding of ST physics at high voltages . While approaches have now been developed to study and quantify the spin torkance of MTJs at low and moderate bias levels, the ST behavior in the ~1V, ultrafast switching regime is not yet well understood.

Here, we report on the study of the ST-excited microwave emissions of CoFe-based MgO MTJs under pulsed, high voltage bias, low magnetic field H_{eff} conditions. We find that the MTJ microwave behavior is highly asymmetric with voltage bias polarity, and the anti-damping spin torque acts to promote parallel alignment moments resulting in broadband microwave emission for MTJs with in-plane coercive fields, $H_c \leq 100$ Oe and for $H_{eff} = H_c$. For the same bias polarity, the ST switching of such MTJs exhibits back-hopping events, strongly suggesting that this behavior is the result of the ST excitation of non-uniform magnetic dynamics in MTJs with relatively low H_c.

The CoFe-based MTJs employed in this study had the following layer structure: IrMn(6.1nm) / CoFe(1.8nm) / Ru / CoFeB(2.0nm) / MgO / CoFe(0.5nm) / CoFeB(3.4nm) and different elliptical nanopillar shapes that varied H_c of the devices from ≤200 Oe, to ≈0Oe Figure 6.1 shows the circuit we employed for the pulse-biased microwave emission measurements. 100 ns voltage pulses (2ns rise and fall times) were sent through a 50Ω line, and any resultant microwave signal was detected via the directional coupler for a 50 ns time period that began 25 ns after the pulse onset. This pulse bias approach was utilized to allow microwave emission measurements at a high bias, ~1V, without degrading the junction during the measurement. The time-domain signal was amplified, fast-Fourier-transformed (FFT), and the result averaged for 40 times at each bias level under various in-plane easy axis fields. The sampling rate limits the linewidth resolution to Δf=40MHz, which is less than the typical linewidth ≥100MHz for CoFeB-based MgO MTJs[17, 27]. In our convention, under positive voltage bias, electrons flow from the free to the fixed layer in which case the in-plane anti-damping spin torque [27] acts to promote anti-parallel (AP) alignment of their ferromagnetic moments.

6.2 Results and Discussions of Microwave Emission Spectra

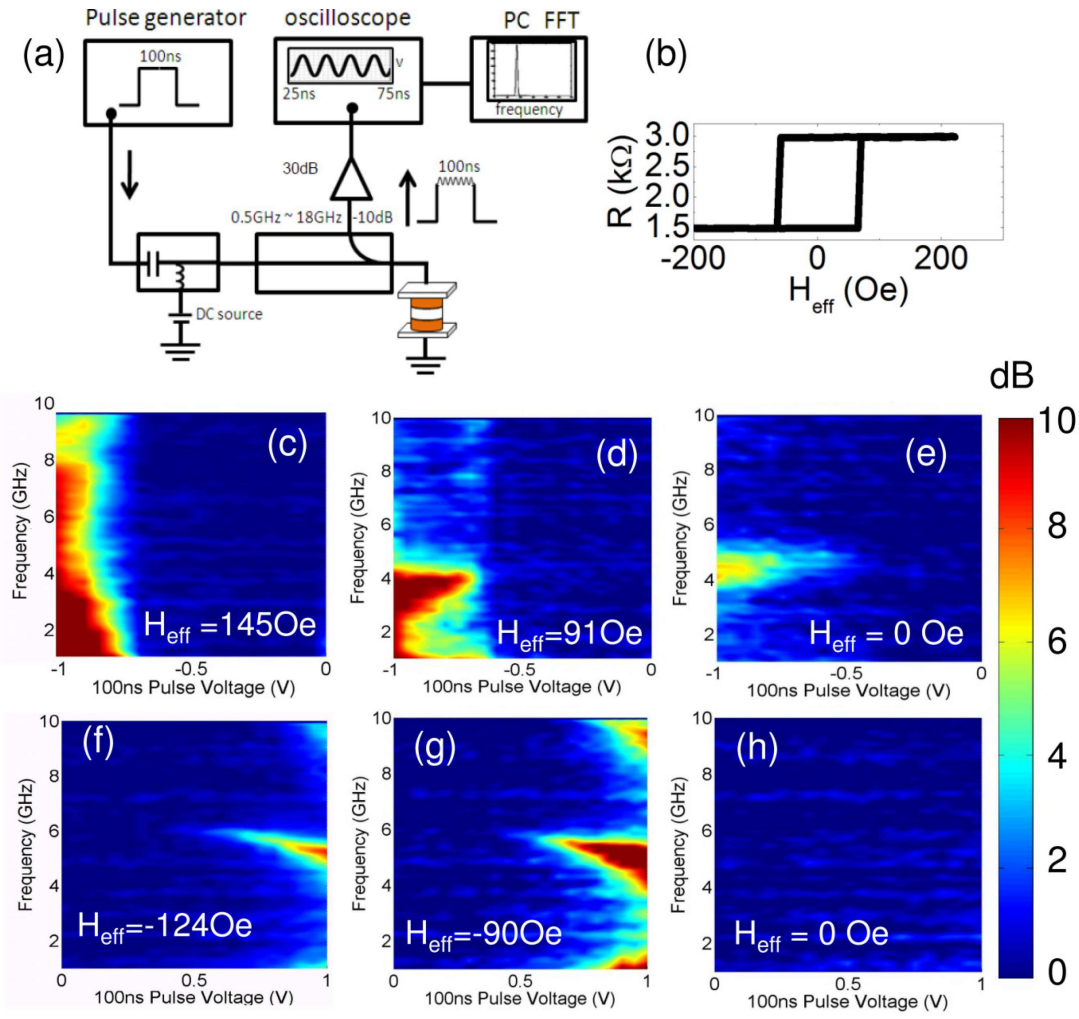

Figure 6.1: High voltage pulse-based microwave measurement setup and contour plots of microwave emission spectra under various fields. (a) is the measurement setup. (b) is the H-R loop of the measurement device. (c)-(h) are the contour plots of pulse-biased microwave emission spectra. The initial configuration for $H > |H_c|$ is P (c,d) and AP (f,g). Bi-stable region are P for (e) and AP for (h).

Figure 6.1(c)-(h) shows the microwave power density (MPD) as the function of the pulse voltage emitted by a 65×130nm MTJ having $H_c \approx 50Oe$ for different

magnetic fields, $H_{eff} = H_{ext} - H_{dip}$, where H_{ext} is the external field applied along the easy axis of the MTJ and H_{dip} is the average dipole field originating from the pinned layers edge charges as determined by the mid-point of the MTJs tunneling magnetoresistance minor loop, $H_d \approx 50Oe$. This junction exhibited good thermal stability and yet was readily switched with 100ns voltage pulses in the parallel-to-antiparallel (P-to-AP) direction, for positive pulses $\leq 1V$ and in the reverse (AP-to-P) for negative pulses $\leq -1V$, for all values of $H_{eff} \leq \pm H_c$. Very similar MPD behavior was observed with other MTJs having the same nominal shape and similar values of H_c.

The MPD plots show that the high voltage microwave emission behavior depends strongly on the magnetic alignment of the electrodes(direction of H_{eff}) and hence on the polarity of the pulse bias. For H_{eff} = +145Oe, P alignment, high negative pulse bias, V>-0.7 V, the result shows a strong broadband microwave emission that extends past 8 GHz but with the greater intensity in the spectral region below 4 GHz. For a similar amplitude but with a reversed field, H_{eff} = 124 Oe and AP alignment, the MTJ exhibits first a thermally excited ferromagnetic resonance mode at ~ 8 GHz, beginning at V~ +0.5 V, which then grows in intensity, narrows in linewidth and gradually redshifts as the bias is increased and the anti-damping spin torque becomes more effective in primarily exciting the FMR-like mode. This asymmetric behavior continues at lower fields, with $H_{eff} = 91Oe$, V >-0.7 V resulting in a broader band of microwave emission extending up to ~ 4.5 GHz with a strong, low frequency tail, in comparison with the more coherent ST-excited mode that is obtained for $H_{eff} = -90Oe$ and V > +0.7, where the low frequency tail is smaller and the primary ST mode is sufficiently coherent to exhibit a distinct second harmonic component at ~ 10 GHz. This asymmetric microwave behavior as the function of bias direction is also

exhibited in the zero field, hysteresis regime. There, pulse-bias to + 1V results in no measurable microwave emissions (Fig. 1 (h)), but a microwave emission centered at 5 GHz begins to be detectable for V -0.5V, with this emission growing in intensity with increasing negative bias, regardless of whether the device is preset in the P or AP configuration. Only for H_{eff}<0, which promotes P alignment, is there no detectable emission for V ≤ -1V. This is surprising since for this bias polarity the in-plane spin torque acts to provide additional damping promoting the P state.

To further understand the microwave spectra, we consider the Kittel formula:

$$f_o = \frac{\gamma}{2\pi}\sqrt{(H_{app}+H_{ani})(H_{app}+H_{ani}+H_{demag}^{eff})} \tag{6.1}$$

Where $H_{app} = H_{ext} \pm H_{dip} \pm H_{FL}$ represent the net applied field after subtracting the dipole field H_{dip} from the fixed layer and field-like torque H_{FL} originating from the exchange coupling from the tunnel barrier. H_{ani} is the in-plane anisotropy field which is around ~100Oe in our samples. $H_{demag}^{eff} = 4\pi M_S - 2K_u/M_S$ is the effective perpendicular demagnetization field where M_S is the saturation magnetization of the free layer and K_u is the uniaxial anisotropy energy energy coefficient which can be affected by the applied voltage bias[28, 21, 94]. For convenience, we define the following field for simplicity:

$$H_1 = H_{app} + H_{ani} \tag{6.2}$$

$$H_2 = H_{app} + H_{ani} + \Delta H_{demag}^{eff} + H_{demag}^{eff} \tag{6.3}$$

Here, we estimate the Kittel frequency f under four different parameters situation. P1 without considering the field-like torque or voltage-induced

anisotropy change. P2 considering the field-like torque. P3 only the voltage-induced anisotropy change. P4 considering both the field-like torque and voltage-induced anisotropy change.

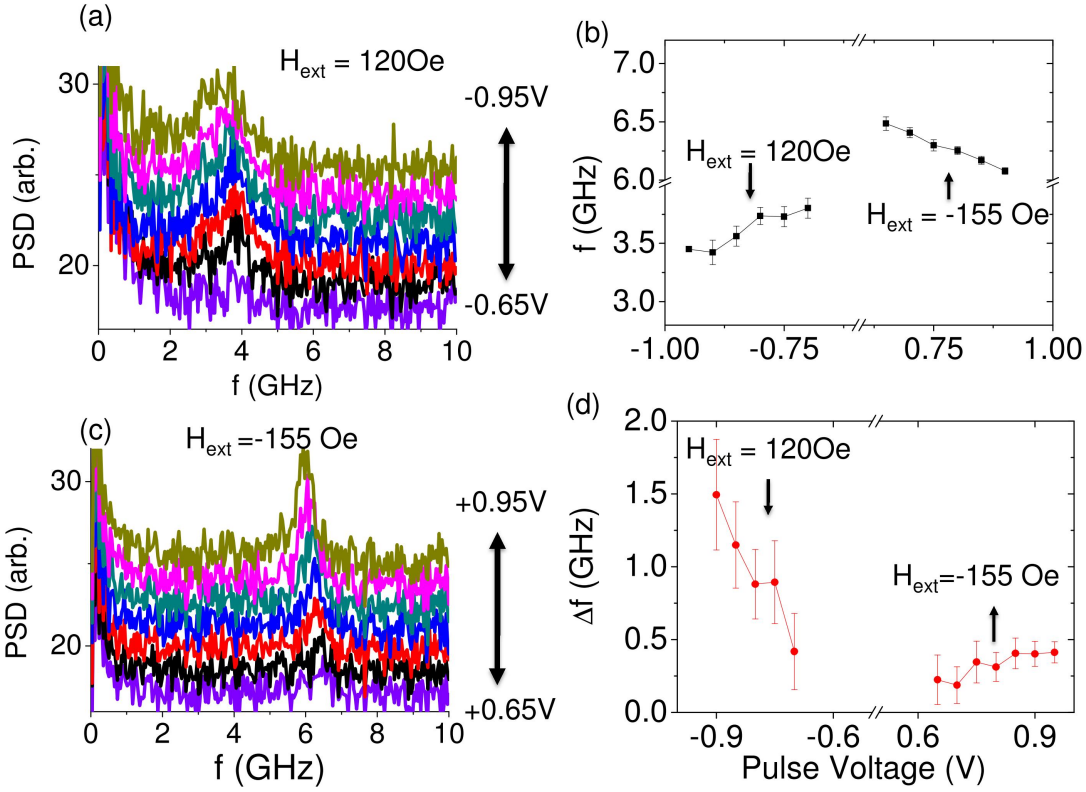

Figure 6.2: (a) and (b)are the pulse-biased microwave emissions in the CoFeB-based MgO MTJ nanopillar under V<0 and V>0 100ns pulse voltages. The frequency shift (a) and line width (b) of the microwave emission peak under various positive and negative voltages. With negative voltage from -0.70V to -0.95V (electrons flowing fixed to free), the line width increases from ~0.5GHz to 1.5GHz, but with positive voltage, the line width only increases from 0.22GHz to 0.41GHz. The shifts of microwave frequency under both polarities are ~0.45GHz.

Set	$\|H_{app}\|$	$H_{FL}(+1V)$	H_{ani}	H^{eff}_{demag}	$\Delta H^{eff}_{demag}(V)$	H_1	H_2	f (GHz)
P1(P)	0.0205	0	0.01	1.3	0	0.0305	1.3305	6.51
P2(P)	0.0135	0.0070	0.01	1.3	0	0.0235	1.3235	5.68
P3(P)	0.0205	0	0.01	1.3	+0.1000	0.0305	1.4305	7.00
P4(P)	0.0135	0.0070	0.01	1.3	+0.1000	0.0235	1.4235	6.11

Table 6.1: Kittel frequency f under four different parameter situations under positive voltage. Only considering H_{FL} = 0.0070 Oe underestimates f, only consider voltage-induced anisotropy change overestimates f. Incorporate both term gives us the f = 6.11GHz closer to the experiment results. $f_{measured}$ = 6.1GHz.

Set	$\|H_{app}\|$	$H_{FL}(-1V)$	H_{ani}	H^{eff}_{demag}	$\Delta H^{eff}_{demag}(V)$	H_1	H_2	f (GHz)
P1(AP)	0.0070	0	0.01	1.3	0	0.017	1.3170	4.81
P2(AP)	0.0030	0.0040	0.01	1.3	0	0.013	1.313	4.19
P3(AP)	0.0070	0	0.01	1.3	-0.1000	0.017	1.2170	4.44
P4(AP)	0.0030	0.0040	0.01	1.3	-0.1000	0.0130	1.213	3.87

Table 6.2: Kittel frequency under four different parameter situations under negative voltage. Considering field-like torque H_{FL} = 0.0040 Oe still overestimates f. Considering both voltage-induced anisotropy change and field-like torque gives us f = 3.87GHz closer to the experimental result $f_{measured}$ = 3.5GHz.

The magnitude of the strength of field-like torque is extrapolated from Ref. [86]. There is a voltage-polarity asymmetry in the field-like torque. We also take that into account in our estimation. Considering the asymmetry, I acquire 70Oe for +1V and 40Oe for -1V. The voltage-induced anisotropy effect used here is 1.0kOe/V. In the literature[94], the dependence of perpendicular anisotropy change is 0.6kOe/V. Here, the value I used in this numerical calcu-

lation is higher to better estimate the effect of voltage-induced anisotropy on the oscillation frequency. Incorporating both the field-like torque and voltage-induced anisotropy changed into consideration, we obtain the Kittel frequency closer to the experimental result shown in figure 6.2. Without considering both effects, the ST-excited microwave frequency will be considerably higher than the experiment results. For V<0, $f_{measured}$ = 3.5GHz, the f calculated without considering both terms is f = 4.81GHz. For V>0, $f_{measured}$ = 6.1GHz, the f calculated is f = 6.51GHz. The pulse-biased high voltage microwave emission spectra reveal the complicated microwave emission spectra under different voltage polarities. Table 6.1 and 6.2 shows that how the field-like torque and voltage-induced anisotropy change influence the microwave frequency f. After considering both effects, we acquire the estimated Kittel frequency close to the experiment measurement without considering the red shift from the in-plane-torque driven oscillation.

6.3 Results and Discussion of Power phase diagram

In figure 6.3 we show the total integrated microwave power emitted by the device of figure 6.1 as the function of H_{eff} and pulse-bias V. For comparison figure 6.4 (a) and (b) shows similar power phase diagram plots obtained from samples with Hc≈ 0 and Hc ≈ 200 Oe, respectively. Dot line in the figure 6.3(b) is a guide to eye to outline the boundary of different power regimes. In figure 6.4(c), B stands for broadband microwave emission, which has been shown in figure 6.1(c). S is spin-torque excited FMR microwave oscillation as figure 6.1(e). N is no microwave emission(figure 6.1 (h)) And C represents coherent microwave emission (figure 6.1(f, g)).

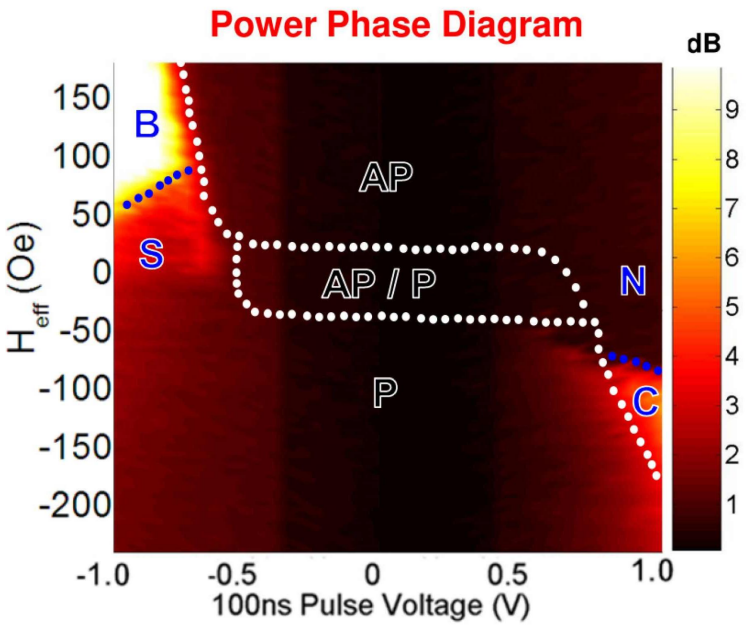

Figure 6.3: High voltage pulse-biased power phase diagram (PPD). The integrated power phase diagram over all the parameters space. Power phase diagram from positive and negative polarities exhibit very different features. The positive PPD exhibits weak microwave power emission. The negative PPD voltage, however, show strong microwave emission within coercivity $H_{ext} \leq H_c = 50$Oe. This result suggests that the spin-torque-driven dynamics are different in the positive and negative polarities.

Figure 6.3 shows the total integrated microwave power emitted by the same device of figure 6.1 as the function of H_{eff} and voltage over all the parameter spaces. Dot line in figure 6.3 is a guide to the eye to show the outline of the boundary of different power regimes. ″B″ stands for broadband microwave emission. ″S″ stands for the spin-torque excited FMR microwave oscillation. ″N″ stands for no microwave emission. ″C″ represents coherent microwave emission.

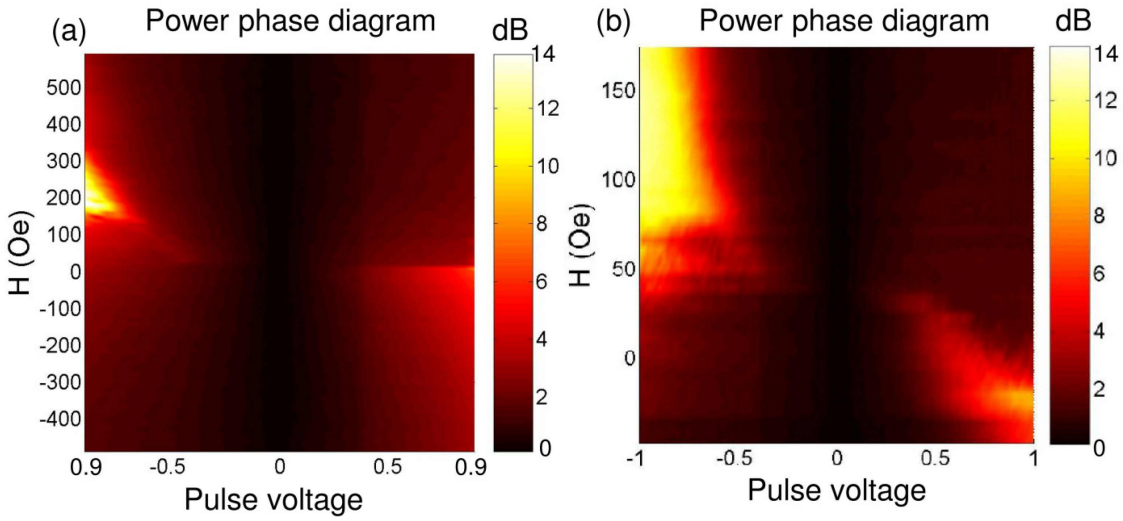

Figure 6.4: Power phase diagrams of MgO MTJ nanopillars from $H_c = 0Oe$ and $H_c = 130Oe$ (a)PSD from the MgO MTJ nanopillar with $H_c = 130Oe$ (b) and $H_c = 0Oe$

Figure 6.4 (a) and (b) are pulse-biased power phase diagrams of MgO nanopillars with $H_c \sim 130$Oe (Fig. 6.4(a)) and $H_c \sim 0$Oe (Fig. 6.4(b)). Regardless of sample geometries, strong microwave emission has be consistently observed while currents and fields are opposing each other, indicating in-plane spin-torque driven microwave oscillation. Theories[**?** 90] have predicted that in-plane torque could change sign under high voltage. One direct consequence of that prediction is the decrease or disappearance of microwave oscillation at all fields of specific voltage bias. In addition, the power phase diagram suggests that in-plane torque have not yet changed sign up to $\sim |1V|$.

The power phase diagram reveals the dynamic status of the MgO nanopillars. Both current polarities exhibit voltage dependence at high voltage bias. The boundaries of both current directions have shifted 40Oe from |0.7V| to |0.9V| toward negative field direction. The microwave peak width with positive bias is

narrow, suggesting coherent oscillation, which also indicated that the nanomagnet is more confined even under high bias. Therefore, it cannot be explained by in-plane torque or joule-heating effect. Similar broadband microwave emission for V<0 has been observed in the Co/Cu/Co spin valve[37, 68]. Micro-magnetic simulation has shown that this broadband microwave emission is attributed to chaotic dynamics in the free layer[40], due to strong in-plane driven dynamics. This behavior can be explained by field-like torque. Other possible mechanisms responsible for the asymmetry of microwave pattern, power phase diagram and switching phase diagram are the reduction of anisotropy field, field-like torque, asymmetry of in-plane torque, joule heating, destabilizing of the fixed layer, and shot noise. However, joule heating, fixed layer instability, and the asymmetry of in-plane torque are not capable of fully explaining all our data, except for the field-like torque.

6.4 Macrospin Simulation

To confirm the effect of the field-like torque of the macrospin simulation, we simulate the complete power phase diagram. Figure6.5 shows the power phase diagram based on macro-magnetic simulation, which is considering that the nanopillar is acting like a single-domain magnet. The simulation parameters are: the free-layer saturation magnetization $M_S = 1050 emu/cm^3$, Gilbert damping constant $\alpha = 0.025$, in-plane anisotropy field $H_{ani} = 50$ Oe. The simulation is done with constant voltage. The thermal fluctuation is incorporated into the simulation by Langevin field. In addition, the MgO nanopillar MTJ samples I used for this studies is the same as Yongtao's 2010 PRL paper[16]. I also use the simulation condition (such as damping factor and saturation magnetization).

Figure 6.5 shows the PSD, individual microwave spectra and dynamic trajectories from the macromagnetic simulation. Figure 6.5(a, b) are the PSD with positive and negative voltage polarities. The microwave emission area in the PSD (V>0) shifts away from the H_{app} = 0 Oe and leaves no microwave emission with H_{app} = 0 Oe, but the microwave emission area in the PSD (V<0) shits towards H_{app} = 0 Oe and exhibit stronger microwave emission in the bi-stable region. This simulated results are consistent with our experiment measurement shown in figure 6.3 and figure 6.4 (b). In addition, the simulated microwave emission exhibits broad line width for V<0 and exhibit smaller line width for V>0. This result is also consistent with our experiment measurement shown figure 6.2 (a, c). The difference between the macromagnetic simulation and our measurement is the broadband microwave emission which shows increasing background noise and even surpass the spin-torque-driven FMR oscillation are not observed in the simulated results. Explanation for the broadband microwave emission feature missing in the macromagnetic simulation can be attributed to the breakdown of the ST-excited single-domain dynamics.

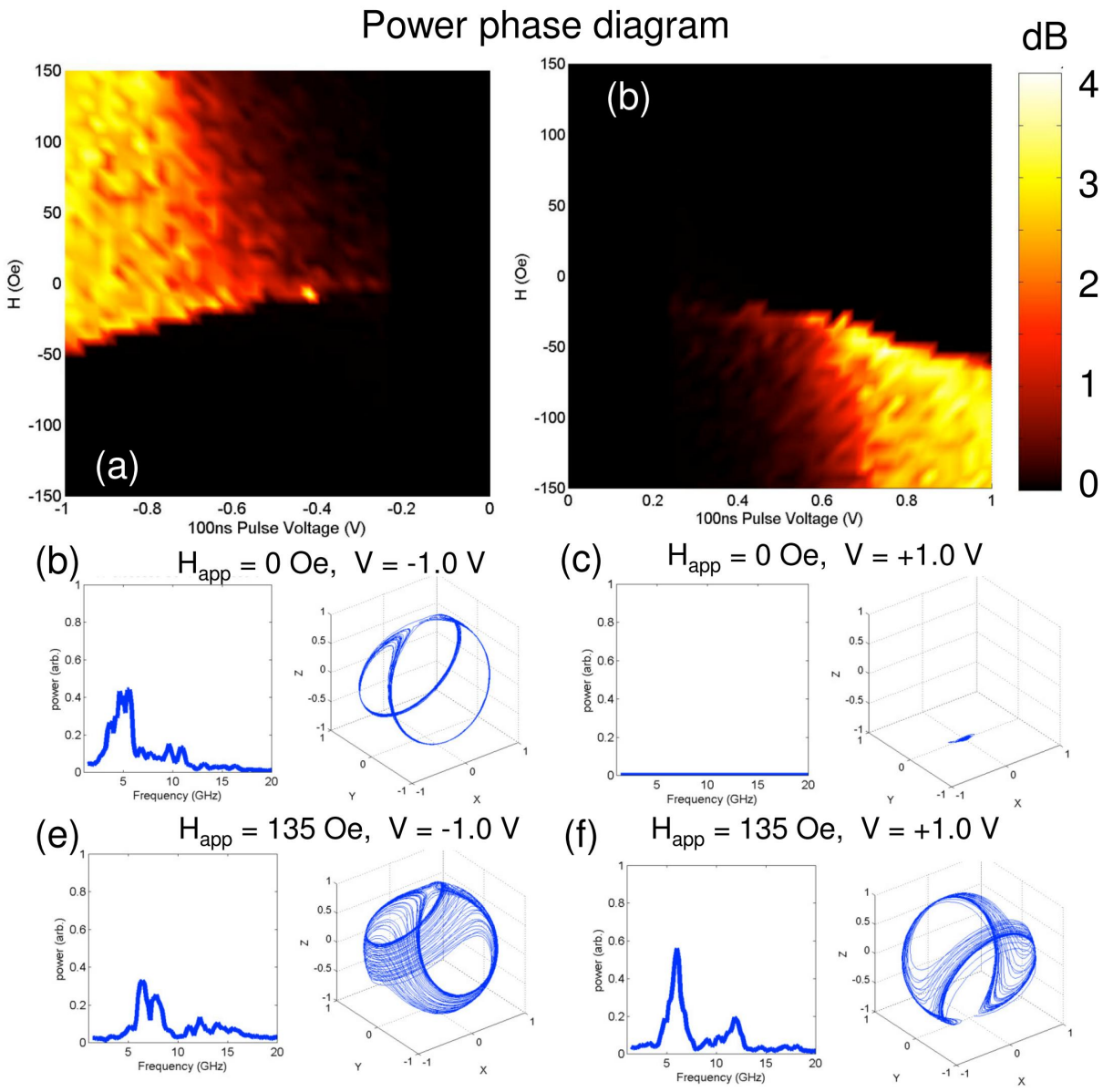

Figure 6.5: Macromagnetic simulation power phase diagram over all parameter space with considering field-like torque in the simulation. (a) and (b) are the PSD under positive and negative voltages. (b, c, e, f) are microwave spectra and trajectories under different H_{app} and pulse voltages. While field-like torque and in-plane torque are opposing each other, the microwave spectra exhibit broader line width and lower frequency (b). Positive voltage exhibit not microwave emission (c) and smaller line width and higher microwave frequency (~6GHz).

Figure 6.6 shows the PSD, microwave emission spectra and dynamic trajectories of the spin-torque-driven dynamics without field-like torque H_{FL}. we observes the microwave emission area does not exhibit asymmetric in the PSD (shown in figure 6.6(a)) or shifting of the microwave emission area. The result confirm our speculation that the field-like torque manifest its effect within the bipolar stable region.

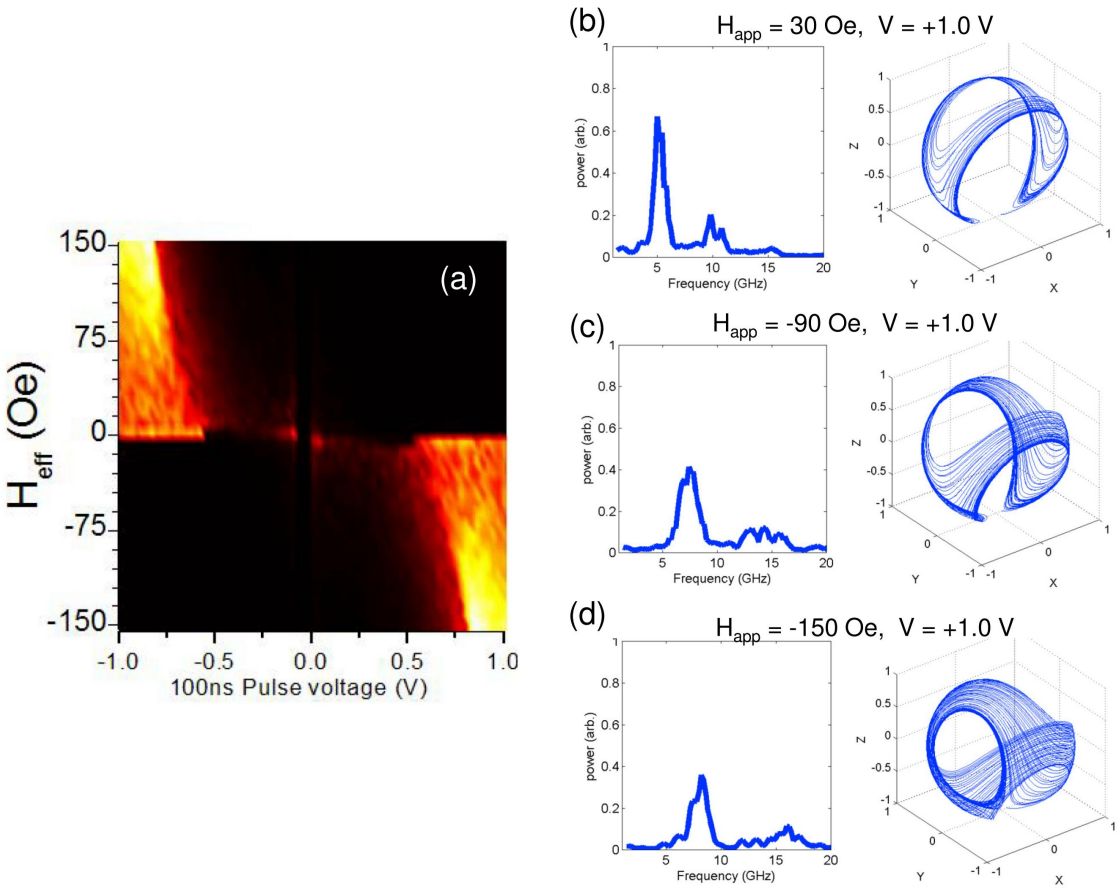

Figure 6.6: Macromagnetic simulation power phase diagram over all parameter space without considering field-like torque in the simulation.

6.5 Comment on Recent Two Spin-Torque-Switching Single-shot Measurement

Two single-shot studies of MgO MTJs shows inconsistent results in pre-oscillation, and post-oscillation, our measurement results could explain this inconsistency. Devolder *et. al*[18] measured P-to-AP switching, which showed post-switching oscillation; however, Cui *et. al*[16] measured AP-to-P switching which exhibited stronger pre-switching oscillation. Our microwave spectra also observed high asymmetric microwave oscillation behavior. With V<0, both TE-FMR, background noise and linewidth are much stronger and larger than V>0, suggesting that the dominating driven-mechanism is different. If our speculation is correct, the switching for P-to-AP is field-like torque assisted switching and V<0 is the in-plane torque dominated switching. Our speculation is consistent with microwave simulation[26], which showed that field-like torque assisted switching will show not pre-switching oscillation, but post-switching oscillation.

6.6 Conclusion

In summary, we have directly probed both the switching and the dynamics of MgO-based MTJs under different current polarities with high voltage pulse (1V). We have directly associated the effects of field-like torque between dynamics and magnetization switching. Under high voltage (~1V), field-like torque could become the dominant mechanism, even larger than coercive fields in symmetric MTJs. It could also significantly affect reliable switching for AP-to-P

switching.

Pulse-biased microwave measurements have revealed highly asymmetric spin-transfer effects under high voltage polarities (~1V) in MgO-based MTJs for the first time. Free layer exhibit broadband emission with V = -1.0V, suggesting strong in-plane and opposite field-like torque V<0 would lower the thermal barrier (due to reduction of H_k) and result in back-hopping. As V >0, field-like torque quench the oscillation and confine the nanomagnet (enhance the in-plane magnetic anisotropy), resulting in coherent oscillation and reliable switching.

Our results have important implication that while pushing for ultrafast switching, higher voltage is required. Field-like torque could affect high voltage spin-transfer effect resulting unreliable switching for AP-to-P switching and enhance the switching for P-to-AP. Simply reducing saturation magnetization will easily resulted in chaotic motion under high voltage; therefore, resulted in unreliable switching. For the future design, it might require large coercivity to suppress field-like torque effect under high voltage or controlling the effects of field-like torque in MTJs.

CHAPTER 7

CONCLUSION

In this thesis, I have presented the details of the material sputtering process and the nanopillar fabrication of a high TMR MgO magnetic tunnel junction (MTJ) at Cornell. I have fabricated various IrMn/$Fe_{40}Co_{40}B_{20}$/MgO/$Fe_{40}Co_{40}B_{20}$, IrMn / $Fe_{40}Co_{40}B_{20}$/MgO/$Fe_{80}B_{20}$, and IrMn/$Fe_{80}B_{20}$/MgO/ $Fe_{40}Co_{40}B_{20}$ into nanopillar structures for spin-torque experiments. In addition, I have further examined the spin-transfer effect in the CoFeB-based and FeB-based high TMR MgO MTJs through several different kinds of spin-torque effect measurement, such switching phase diagrams (SPD) and spin-torque ferromagnetic resonance (ST-FMR).

High TMR CoFeB-based and FeB-based Asymmetric MgO MTJs exhibit oscillatory signature in the tunneling conductance as a function voltage dI/dV-V within the low voltage bias (V≤|0.5V|). We exam the oscillatory signature in the tunneling conductance under four different ferromagnetic material configurations and conclude the that tunneling conductance can be associated with the electronic structure in the electrode materials.

Our pulse-biased microwave emission spectra also further reveals the complicated current-induced effect previously unobserved in the low RA MgO MTJ spin-torque devices. Field-like torque can change high voltage pulse-biased microwave dynamics within the coercive field region ($\leq H_c$) induced broadband microwave emission under negative voltage and completely suppress the nanomagnet dynamics showing no microwave emission with positive voltage. Our pulse-biased microwave emission measurement also reveals that the voltage-induced anisotropy change under high voltage bias even in the low RA CoFeB-based MgO MTJ spin-torque devices and affect the microwave dynamics.

To conclude my thesis, we examined the spin-torque effect in asymmetric MTJs and we observed that the electronic structures of the ferromagnetic electrode affecting the magnetotransport, spin-dependent transport and spin-torque effect in the high TMR FeCo-based MgO MTJs. In addition, the high voltage pulse-biased microwave emission measurement reveal the nanomagnet dynamics under high voltage and suggest the dynamics is influenced by the interaction from in-plane torque, field-like torque and voltage-induced anisotropy change. Our results provide an understanding of the physics for the application of ST-MRAM while pursuing ultrafast switching and asymmetric electrodes materials.

BIBLIOGRAPHY

[1] Y. Ando, T. Miyakoshi, M. Oogane, T. Miyazaki, H. Kubota, K. Ando, and S. Yuasa. Spin-dependent tunneling spectroscopy in single-crystal FeMgOFe tunnel junctions. *Applied Physics Letters*, 87(14):142502, 2005.

[2] L Berger. Emission of spin waves by a magnetic multilayer traversed by a current. *Physical Review B*, 54(13):9353–9358, 1996.

[3] M. Bischoff, T. Yamada, C. Fang, R. de Groot, and H. van Kempen. Local electronic structure of Fe(001) surfaces studied by scanning tunneling spectroscopy. *Physical Review B*, 68(4):1–7, July 2003.

[4] F. Bonell, T. Hauet, S. Andrieu, F. Bertran, P. Le Fèvre, L. Calmels, A. Tejeda, F. Montaigne, B. Warot-Fonrose, B. Belhadji, A. Nicolaou, A. Taleb-Ibrahimi, L. Plucinski, Y. Zhao, B. Sinkovic, and E. Vescovo. Spin-Polarized Electron Tunneling in bcc FeCo/MgO/FeCo(001) Magnetic Tunnel Junctions. *Physical Review Letters*, 108:176602, April 2012.

[5] P. M. Braganca, I. N. Krivorotov, O. Ozatay, A. G. F. Garcia, N. C. Emley, J. C. Sankey, D. C. Ralph, and R. A. Buhrman. Reducing the critical current for short-pulse spin-transfer switching of nanomagnets. *Applied Physics Letters*, 87(11):112507, 2005.

[6] P. M. Braganca, O. Ozatay, A. G. F. Garcia, O. Lee, D. C. Ralph, and R. A. Buhrman. Enhancement in spin-torque efficiency by nonuniform spin current generated within a tapered nanopillar spin valve. *Physical Review B*, 77(14):1–6, April 2008.

[7] Patrick M Braganca. *MATERIAL AND STRUCTURAL ENHANCEMENTS*

TO SPIN TRANSFER PHENOMENA IN NANOPILLAR SPIN-VALVE DEVICES. PhD thesis, 2008.

[8] Patrick M Braganca, Jordan A Katine, Senior Member, Nathan C Emley, Daniele Mauri, Jeffrey R Childress, Philip M Rice, Eugene Delenia, Daniel C Ralph, and Robert A Buhrman. A Three-Terminal Approach to Developing Spin-Torque Written Magnetic Random Access Memory Cells. *IEEE Nanotechnology*, 8(2):190–195, 2009.

[9] A M Bratkovsky. Tunneling of electrons in conventional and half-metallic systems: Towards very large magnetoresistance. 56(5):2344–2347, 1997.

[10] W. F. Brinkman. Tunneling Conductance of Asymmetrical Barriers. *Journal of Applied Physics*, 41(5):1915, 1970.

[11] W. Butler, X.-G. Zhang, T. Schulthess, and J. MacLaren. Spin-dependent tunneling conductance of Fe—MgO—Fe sandwiches. *Physical Review B*, 63(5):1–12, January 2001.

[12] William H Butler. Tunneling magnetoresistance from a symmetry filtering effect. *Science and Technology of Advanced Materials*, 9(1):014106, April 2008.

[13] J. J. Cha, J. C. Read, W. F. Egelhoff, P. Y. Huang, H. W. Tseng, Y. Li, R. a. Buhrman, and D. a. Muller. Atomic-scale spectroscopic imaging of CoFeB/MgBO/CoFeB magnetic tunnel junctions. *Applied Physics Letters*, 95(3):032506, 2009.

[14] Judy J. Cha, J. C. Read, R. A. Buhrman, and David A. Muller. Spatially resolved electron energy-loss spectroscopy of electron-beam grown and sputtered CoFeBMgOCoFeB magnetic tunnel junctions. *Applied Physics Letters*, 91(6):062516, 2007.

[15] A. Chanthbouala, R. Matsumoto, J. Grollier, V. Cros, A. Anane, A. Fert, a. V. Khvalkovskiy, K. a. Zvezdin, K. Nishimura, Y. Nagamine, H. Maehara, K. Tsunekawa, A. Fukushima, and S. Yuasa. Vertical-current-induced domain-wall motion in MgO-based magnetic tunnel junctions with low current densities. *Nature Physics*, 7(8):626–630, April 2011.

[16] Y.-T. Cui, G. Finocchio, C. Wang, J. A. Katine, R. A. Buhrman, and D. C. Ralph. Single-shot time-domain studies of spin-torque-driven switching in magnetic tunnel junctions. *Physical review letters*, 104(9):097201, March 2010.

[17] Alina M. Deac, Akio Fukushima, Hitoshi Kubota, Hiroki Maehara, Yoshishige Suzuki, Shinji Yuasa, Yoshinori Nagamine, Koji Tsunekawa, David D. Djayaprawira, and Naoki Watanabe. Bias-driven high-power microwave emission from MgO-based tunnel magnetoresistance devices. *Nature Physics*, 4(10):803–809, August 2008.

[18] T. Devolder, J. Hayakawa, K. Ito, H. Takahashi, S. Ikeda, P. Crozat, N. Zerounian, Joo-Von Kim, C. Chappert, and H. Ohno. Single-Shot Time-Resolved Measurements of Nanosecond-Scale Spin-Transfer Induced Switching: Stochastic Versus Deterministic Aspects. *Physical Review Letters*, 100(5):2–5, February 2008.

[19] D.E. Eastman, F.J. Himpsel, and J.A. Knapp. Experimental Exchange-Split Energy-Band Dispersions for Fe, Co, and Ni. *Physical Review Letters*, 44(2):95, 1980.

[20] Nathan C Emley. *MAGNETIC MULTILAYER NANOPILLARS FOR THE STUDY OF CURRENT-INDUCED REVERSAL OF A THIN MAGNETIC LAYER*. PhD thesis, 2005.

[21] M. Endo, S. Kanai, S. Ikeda, F. Matsukura, and H. Ohno. Electric-field effects on thickness dependent magnetic anisotropy of sputtered MgO/Co[sub 40]Fe[sub 40]B[sub 20]/Ta structures. *Applied Physics Letters*, 96(21):212503, 2010.

[22] R.H. Fowler and L. Nordheim. No Title. *Proc. Roy. Soc. London*, 119:173, 1928.

[23] G. D. Fuchs. SPIN-TRANSFER EFFECTS IN NANOSCALE MAGNETIC TUNNEL JUNCTIONS AND SPIN VALVES. (May), 2007.

[24] G. D. Fuchs, N. C. Emley, I. N. Krivorotov, P. M. Braganca, E. M. Ryan, S. I. Kiselev, J. C. Sankey, D. C. Ralph, R. a. Buhrman, and J. a. Katine. Spin-transfer effects in nanoscale magnetic tunnel junctions. *Applied Physics Letters*, 85(7):1205, 2004.

[25] G. D. Fuchs, I. N. Krivorotov, P. M. Braganca, N. C. Emley, a. G. F. Garcia, D. C. Ralph, and R. a. Buhrman. Adjustable spin torque in magnetic tunnel junctions with two fixed layers. *Applied Physics Letters*, 86(15):152509, 2005.

[26] Samir Garzon, Yaroslaw Bazaliy, Richard Webb, Mark Covington, Shehzaad Kaka, and Thomas Crawford. Macrospin model to explain the absence of preswitching oscillations in magnetic tunnel junctions: Fieldlike spin-transfer torque. *Physical Review B*, 79(10), March 2009.

[27] B Georges, J Grollier, V Cros, A Fert, A Fukushima, H Kubota, K Yakushijin, S Yuasa, and K Ando. Origin of the spectral linewidth in nonlinear spin-transfer oscillators based on MgO tunnel junctions. *Science And Technology*, pages 1–4, 2009.

[28] Seung-Seok Ha, Nam-Hee Kim, Sukmock Lee, Chun-Yeol You, Yoichi Shiota, Takuto Maruyama, Takayuki Nozaki, and Yoshishige Suzuki. Voltage induced magnetic anisotropy change in ultrathin Fe[sub 80]Co[sub 20]/MgO junctions with Brillouin light scattering. *Applied Physics Letters*, 96(14):142512, 2010.

[29] Christian Heiliger and M. D Stiles. Ab Initio Studies of the Spin-Transfer Torque in Magnetic Tunnel Junctions. *Physical Review Letters*, 100(18):1–4, May 2008.

[30] Yiming Huai, Frank Albert, Paul Nguyen, Mahendra Pakala, and Thierry Valet. Observation of spin-transfer switching in deep submicron-sized and low-resistance magnetic tunnel junctions. *Applied Physics Letters*, 84(16):3118, 2004.

[31] M Julliere. Tunneling between ferromagnetic films. 54(3):225–226, 1975.

[32] Alan Kalitsov, Mairbek Chshiev, Ioannis Theodonis, Nicholas Kioussis, and W. H Butler. Spin-transfer torque in magnetic tunnel junctions. *Physical Review B*, 79(17):1–11, May 2009.

[33] J. A. Katine, F. J. Albert, R. A. Buhrman, E. B. Myers, and D. C. Ralph. Current-driven magnetization reversal and spin-wave excitations in Co /Cu /Co pillars. *Physical review letters*, 84(14):3149–52, April 2000.

[34] J. a. Katine, Michael K. Ho, Yongho Sungtaek Ju, and C. T. Rettner. Patterning damage in narrow trackwidth spin-valve sensors. *Applied Physics Letters*, 83(2):401, 2003.

[35] T. Kawahara, K. Ito, R. Takemura, and H. Ohno. Spin-transfer torque RAM

technology: Review and prospect. *Microelectronics Reliability*, 52(4):613–627, April 2012.

[36] Asma H Khalil, Mark D Stiles, Christian Heiliger, and I Physikalisches Institut. Influence of Band Parameters on Spin-Transfer Torque in Tunnel Junctions : Model Calculations. *IEEE Transactions on MAGNETICS*, 46(6):2009–2011, 2010.

[37] S. I. Kiselev, J. C. Sankey, I. N. Krivorotov, N. C. Emley, R. J. Schoelkopf, R. A. Buhrman, and D. C. Ralph. Microwave oscillations of a nanomagnet driven by a spin-polarized current. *Nature*, 425(6956):380–3, September 2003.

[38] Hitoshi Kubota, Akio Fukushima, Kay A Y Yakushiji, Taro Nagahama, Shinji Yuasa, Koji Ando, Hiroki Maehara, Yoshinori Nagamine, Koji Tsunekawa, David D. Djayaprawira, Naoki Watanabe, and Yoshishige Suzuki. Quantitative measurement of voltage dependence of spin-transfer torque in MgO-based magnetic tunnel junctions. *Nature Physics*, 4(1):37–41, November 2007.

[39] P. LeClair, J. Kohlhepp, C. van de Vin, H. Wieldraaijer, H. Swagten, W. de Jonge, a. Davis, J. MacLaren, J. Moodera, and R. Jansen. Band Structure and Density of States Effects in Co-Based Magnetic Tunnel Junctions. *Physical Review Letters*, 88(10):11–14, February 2002.

[40] Kyung-Jin Lee, Alina Deac, Olivier Redon, Jean-Pierre Nozières, and Bernard Dieny. Excitations of incoherent spin-waves due to spin-transfer torque. *Nature materials*, 3(12):877–81, December 2004.

[41] O. J. Lee, V. S. Pribiag, P. M. Braganca, P. G. Gowtham, D. C. Ralph, and

R. a. Buhrman. Ultrafast switching of a nanomagnet by a combined out-of-plane and in-plane polarized spin current pulse. *Applied Physics Letters*, 95(1):012506, 2009.

[42] Robert E. Lee. Microfabrication by ion-beam etching. *J. Vac. Sci. Technol.*, 16(2):164, 1979.

[43] Z. Li and S. Zhang. Thermally assisted magnetization reversal in the presence of a spin-transfer torque. *Physical Review B*, 69(13):1–6, April 2004.

[44] Z. Li, S. Zhang, Z. Diao, Y. Ding, X. Tang, D. Apalkov, Z. Yang, K. Kawabata, and Y. Huai. Perpendicular Spin Torques in Magnetic Tunnel Junctions. *Physical Review Letters*, 100(24):1–4, June 2008.

[45] L. Liu, C.-F. Pai, Y. Li, H. W. Tseng, D. C. Ralph, and R. A. Buhrman. Spin-Torque Switching with the Giant Spin Hall Effect of Tantalum. *Science*, 336(6081):555–558, May 2012.

[46] Luqiao Liu, Takahiro Moriyama, D. C. Ralph, and R. A. Buhrman. Reduction of the spin-torque critical current by partially canceling the free layer demagnetization field. *Applied Physics Letters*, 94(12):122508, 2009.

[47] A Manchon, S Zhang, and K.-J Lee. Signatures of asymmetric and inelastic tunneling on the spin torque bias dependence. *New York*, pages 1–9, 2010.

[48] J. Mathon and a. Umerski. Theory of tunneling magnetoresistance of an epitaxial Fe/MgO/Fe(001) junction. *Physical Review B*, 63(22):1–4, May 2001.

[49] R Matsumoto, S Nishioka, M Mizuguchi, M Shiraishi, H Maehara, K Tsunekawa, D Djayaprawira, N Watanabe, Y Otani, and T Nagahama.

Dependence on annealing temperatures of tunneling spectra in high-resistance CoFeB/MgO/CoFeB magnetic tunnel junctions. *Solid State Communications*, 143(11-12):574–578, September 2007.

[50] Rie Matsumoto, André Chanthbouala, Julie Grollier, Vincent Cros, Albert Fert, Kazumasa Nishimura, Yoshinori Nagamine, Hiroki Maehara, Koji Tsunekawa, Akio Fukushima, and Shinji Yuasa. Spin-Torque Diode Measurements of MgO-Based Magnetic Tunnel Junctions with Asymmetric Electrodes. *Applied Physics Express*, 4(6):063001, May 2011.

[51] Herbert B. Michaelson. The work function of the elements and its periodicity. *Journal of Applied Physics*, 48:4729, 1977.

[52] Casey Miller, Zhi-Pan Li, Ivan Schuller, R. Dave, J. Slaughter, and Johan kerman. Dynamic Spin-Polarized Resonant Tunneling in Magnetic Tunnel Junctions. *Physical Review Letters*, 99(4):1–4, July 2007.

[53] J. S. Moodera, Lisa R. Kinder, Terrilyn M. Wong, and R. Meservey. 1995 JS Moodera CoFe NiFe junction.pdf. *Physical Review Letters*, 74:3273, 1995.

[54] Jagadeesh Moodera, Janusz Nowak, and Rene van de Veerdonk. Interface Magnetism and Spin Wave Scattering in Ferromagnet-Insulator-Ferromagnet Tunnel Junctions. *Physical Review Letters*, 80(13):2941–2944, March 1998.

[55] Jagadeesh S Moodera and George Mathon. Spin polarized tunneling in ferromagnetic junctions. *Journal of Magnetism and Magnetic Materials*, 200:248–273, 1999.

[56] E. B. Myers. Current-Induced Switching of Domains in Magnetic Multilayer Devices. *Science*, 285(5429):867–870, August 1999.

[57] Shingo Nishioka, Rie Matsumoto, Hiroyuki Tomita, Takayuki Nozaki, Yoshishige Suzuki, Hiroyoshi Itoh, and Shinji Yuasa. Spin dependent tunneling spectroscopy in single crystalline bcc-Co/MgO/bcc-Co(001) junctions. *Applied Physics Letters*, 93(12):122511, 2008.

[58] Se-Chung Oh, Seung-Young Park, Aurélien Manchon, Mairbek Chshiev, Jae-Ho Han, Hyun-Woo Lee, Jang-Eun Lee, Kyung-Tae Nam, Younghun Jo, Yo-Chan Kong, Bernard Dieny, and Kyung-Jin Lee. Bias-voltage dependence of perpendicular spin-transfer torque in asymmetric MgO-based magnetic tunnel junctions. *Nature Physics*, 5(12):898–902, October 2009.

[59] O. Ozatay. SPIN DEPENDENT TRANSPORT AND SPIN TRANSFER IN NANOCONSTRICTIONS AND CURRENT CONFINED NANOMAGNETS. (January), 2007.

[60] O. Ozatay, P. G. Gowtham, K. W. Tan, J. C. Read, K. A. Mkhoyan, M. G. Thomas, G. D. Fuchs, P. M. Braganca, E. M. Ryan, K. V. Thadani, J. Silcox, D. C. Ralph, and R. A. Buhrman. Sidewall oxide effects on spin-torque- and magnetic-field-induced reversal characteristics of thin-film nanomagnets. *Nature materials*, 7(7):567–73, July 2008.

[61] Stuart S P Parkin, Christian Kaiser, Alex Panchula, Philip M Rice, Brian Hughes, Mahesh Samant, and See-Hun Yang. Giant tunnelling magnetoresistance at room temperature with MgO (100) tunnel barriers. *Nature materials*, 3(12):862–7, December 2004.

[62] Xilin Peng, Stacey Wakeham, Augusto Morrone, Steven Axdal, Michael Feldbaum, Justin Hwu, Tom Boonstra, Yonghua Chen, and Juren Ding. Towards the sub-50nm magnetic device definition: Ion beam etching (IBE) vs plasma-based etching. *Vacuum*, 83(6):1007–1013, February 2009.

[63] L. Plucinski, Yuan Zhao, C. M. Schneider, B. Sinkovic, and E. Vescovo. Surface electronic structure of ferromagnetic Fe(001). *Physical Review B*, 80(18):1–6, November 2009.

[64] D.C. Ralph and M.D. Stiles. Spin transfer torques. *Journal of Magnetism and Magnetic Materials*, 320(7):1190–1216, April 2008.

[65] J. C. Read. MAGNESIUM BORON OXIDE TUNNEL BARRIERS. (May), 2009.

[66] J. C. Read, Judy J. Cha, William F. Egelhoff, H. W. Tseng, P. Y. Huang, Y. Li, David A. Muller, and R. A. Buhrman. High magnetoresistance tunnel junctions with MgBO barriers and NiFeB free electrodes. *Applied Physics Letters*, 94(11):112504, 2009.

[67] J. C. Read, P. G. Mather, and R. a. Buhrman. X-ray photoemission study of CoFeBMgO thin film bilayers. *Applied Physics Letters*, 90(13):132503, 2007.

[68] J. Sankey, I. Krivorotov, S. Kiselev, P. Braganca, N. Emley, R. Buhrman, and D. Ralph. Mechanisms limiting the coherence time of spontaneous magnetic oscillations driven by dc spin-polarized currents. *Physical Review B*, 72(22):2–6, December 2005.

[69] J. C. Sankey, P. M. Braganca, A. G. F. Garcia, I. N. Krivorotov, R. A. Buhrman, and D. C. Ralph. Spin-Transfer-Driven Ferromagnetic Resonance of Individual Nanomagnets. *Physical Review Letters*, 96(22):1–4, June 2006.

[70] Jack C. Sankey, Yong-Tao Cui, Jonathan Z. Sun, John C. Slonczewski, Robert a. Buhrman, and Daniel C. Ralph. Measurement of the spin-

transfer-torque vector in magnetic tunnel junctions. *Nature Physics*, 4(1):67–71, November 2007.

[71] J. Schmalhorst, a. Thomas, S. Kämmerer, O. Schebaum, D. Ebke, M. Sacher, G. Reiss, a. Hütten, a. Turchanin, a. Gölzhäuser, and E. Arenholz. Transport properties of magnetic tunnel junctions with Co2MnSi electrodes: The influence of temperature-dependent interface magnetization and electronic band structure. *Physical Review B*, 75(1):1–10, January 2007.

[72] K. Schwarz, P. Mohn, P. Blaha, J. Kubler, Home Search, Collections Journals, About Contact, and My Iopscience. Electronic and magnetic structure of BCC Fe-Co alloys from band theory. *J. Phys. F:Met. Phys.*, 14:2659, 1984.

[73] Fengyuan Shi, Hua Xiang, J. Joshua Yang, M.S Rzchowski, Y.a. Chang, and P.M. Voyles. Inverse TMR in a nominally symmetric CoFe/AlOx/CoFe junction induced by interfacial Fe3O4 investigated by STEM-EELS. *Journal of Magnetism and Magnetic Materials*, pages 1–8, January 2012.

[74] J.C. Slonczewski. Current-driven excitation of magnetic multilayers. *Journal of Magnetism and Magnetic Materials*, 39(1-2):4984–L7, June 1996.

[75] J.C. Slonczewski and J.Z. Sun. Theory of voltage-driven current and torque in magnetic tunnel junctions. *Journal of Magnetism and Magnetic Materials*, 310(2):169–175, March 2007.

[76] J. A. Stroscio, D. T. Pierce, A. Davies, and R. J. Celotta. Tunneling Spectroscopy of bcc (001) Surface States. *Physical Review Letters*, 75(16):2960, 1995.

[77] J. Sun. Spin-current interaction with a monodomain magnetic body: A model study. *Physical Review B*, 62(1):570–578, July 2000.

[78] J. Z. Sun, M. C. Gaidis, G. Hu, E. J. OSullivan, S. L. Brown, J. J. Nowak, P. L. Trouilloud, and D. C. Worledge. High-bias backhopping in nanosecond time-domain spin-torque switches of MgO-based magnetic tunnel junctions. *Journal of Applied Physics*, 105(7):07D109, 2009.

[79] J. Z. Sun, M. C. Gaidis, E. J. OSullivan, E. a. Joseph, G. Hu, D. W. Abraham, J. J. Nowak, P. L. Trouilloud, Yu Lu, S. L. Brown, D. C. Worledge, and W. J. Gallagher. A three-terminal spin-torque-driven magnetic switch. *Applied Physics Letters*, 95(8):083506, 2009.

[80] Y.-H. Tang, Nicholas Kioussis, Alan Kalitsov, W. H Butler, and Roberto Car. Controlling the Nonequilibrium Interlayer Exchange Coupling in Asymmetric Magnetic Tunnel Junctions. *Physical Review Letters*, 103(5):1–4, July 2009.

[81] Y.-H. Tang, Nicholas Kioussis, Alan Kalitsov, W. H. Butler, and Roberto Car. Influence of asymmetry on bias behavior of spin torque. *Physical Review B*, 81(5):1–9, February 2010.

[82] J M De Teresa, A Barthélémy, A Fert, J P Contour, R Lyonnet, F Montaigne, P Seneor, A Vaurès, and R R P Ap. Inverse Tunnel Magnetoresistance in Co/SrTiO/LaSrMnONew Ideas on Spin-Polarized Tunneling. 82(21):80–83, 1999.

[83] Ioannis Theodonis, Nicholas Kioussis, Alan Kalitsov, Mairbek Chshiev, and W. H Butler. Anomalous Bias Dependence of Spin Torque in Magnetic Tunnel Junctions. *Physical Review Letters*, 97(23):2–5, December 2006.

[84] S Tsunegi, Y Sakuraba, M Oogane, N D Telling, L R Shelford, E Arenholz, G van der Laan, R J Hicken, K Takanashi, Y Ando, Home Search, Col-

lections Journals, About Contact, My Iopscience, and I P Address. Tunnel magnetoresistance in epitaxially grown magnetic tunnel junctions using Heusler alloy electrode and MgO barrier. *Journal of Physics D: Applied Physics*, 42(19):195004, October 2009.

[85] C. Wang, Y.-T. Cui, J. Sun, J. Katine, R. Buhrman, and D. Ralph. Bias and angular dependence of spin-transfer torque in magnetic tunnel junctions. *Physical Review B*, 79(22):1–10, June 2009.

[86] Chen Wang, Yong-Tao Cui, Jordan a. Katine, Robert a. Buhrman, and Daniel C. Ralph. Time-resolved measurement of spin-transfer-driven ferromagnetic resonance andspin torque in magnetic tunnel junctions. *Nature Physics*, 7(6):496–501, February 2011.

[87] Wenhong Wang, Enke Liu, Masaya Kodzuka, Hiroaki Sukegawa, Marec Wojcik, Eva Jedryka, G. H. Wu, Koichiro Inomata, Seiji Mitani, and Kazuhiro Hono. Coherent tunneling and giant tunneling magnetoresistance in Co$_{2}$FeAl/MgO/CoFe magnetic tunneling junctions. *Physical Review B*, 81(14):1–4, April 2010.

[88] E.L. Wolf. *Principles of Electron Tunneling Spectroscopy*. Oxford Univeristy Press, London, 1985.

[89] S. A. Wolf, D. D. Awschalom, R. A. Buhrman, J. M. Daughton, S von Molnár, M. L. Roukes, A. Y. Chtchelkanova, and D. M. Treger. Spintronics: a spin-based electronics vision for the future. *Science (New York, N.Y.)*, 294(5546):1488–95, November 2001.

[90] Jiang Xiao, Gerrit Bauer, and Arne Brataas. Spin-transfer torque in mag-

netic tunnel junctions: Scattering theory. *Physical Review B*, 77(22):1–9, June 2008.

[91] Haifang Yang, Aizi Jin, Qiang Luo, Junjie Li, Changzhi Gu, and Zheng Cui. Electron beam lithography of HSQ/PMMA bilayer resists for negative tone lift-off process. *Microelectronic Engineering*, 85(5-6):814–817, May 2008.

[92] Shinji Yuasa, Taro Nagahama, Akio Fukushima, Yoshishige Suzuki, and Koji Ando. Giant room-temperature magnetoresistance in single-crystal Fe/MgO/Fe magnetic tunnel junctions. *Nature materials*, 3(12):868–71, December 2004.

[93] S. Zhang, P. Levy, a. Marley, and S. Parkin. Quenching of Magnetoresistance by Hot Electrons in Magnetic Tunnel Junctions. *Physical Review Letters*, 79(19):3744–3747, November 1997.

[94] Jian Zhu, J. Katine, Graham Rowlands, Yu-Jin Chen, Zheng Duan, Juan Alzate, Pramey Upadhyaya, Juergen Langer, Pedram Amiri, Kang Wang, and Ilya Krivorotov. Voltage-Induced Ferromagnetic Resonance in Magnetic Tunnel Junctions. *Physical Review Letters*, 108(19):1–5, May 2012.